Title

Mapping the Conformational Landscapes of Viral Fusion Proteins

Author

Shoemaker, Sophie Rose

Publication Date

2024

Peer reviewed|Thesis/dissertation

Mapping the Conformational Landscapes of Viral Fusion Proteins

By

Sophie Rose Shoemaker

A dissertation submitted in partial satisfaction of the

requirements for the degree of

Doctor of Philosophy

in

Molecular and Cell Biology

in the

Graduate Division

of the

University of California, Berkeley

Committee in charge:

Professor Susan Marqusee, Chair

Professor Molly Ohainle

Professor David Savage

Professor Alanna Schepartz

Fall 2024

Abstract

Mapping the Conformational Landscape of Viral Fusion Proteins

By

Sophie Rose Shoemaker

Doctor of Philosophy in Molecular and Cell Biology

University of California, Berkeley

Professor Susan Marqusee, Chair

Viral fusion proteins are essential for most enveloped viruses to infect cells, making them key targets for vaccines and therapeutics. Despite a wealth of structural data, their conformational dynamics remain insufficiently understood, presenting challenges to optimizing vaccine and therapeutic design. Viral fusion proteins undergo dramatic conformational changes during fusion, making it both an interesting protein folding question and a therapeutic opportunity. Hydrogen-deuterium exchange mass spectrometry (HDX-MS) is uniquely suited to investigate the conformational landscapes of viral fusion proteins, providing insights into solvent accessibility and secondary structure stability under diverse conditions.

This dissertation employs HDX-MS to study the conformational dynamics of the SARS-CoV-2 spike protein and Rabies virus glycoprotein (RABV-G). Chapter 1 reviews viral fusion proteins and their study. Chapter 2 discusses our work that revealed a novel, open-interface trimer conformation of the SARS-CoV-2 spike protein, exposing previously inaccessible surface areas to solvent and antibodies. Temperature, receptor binding, and sequence variations influence the thermodynamics and kinetics of this transition. Chapter 3 extends these findings by demonstrating that this conformation is sampled on enveloped virus-like particles (eVLPs) and allows us to see how other engineering efforts and natural evolution have shaped the conformational landscape of spike. This chapter also reveals that cleavage at the multibasic furin site allosterically increases the flexibility of the S2’ protease site — providing a molecular basis for enhanced infectivity in viruses with this cleavage site. Chapter 4 explores ongoing studies of RABV-G, comparing its conformational dynamics as a soluble ectodomain and on eVLPs, highlighting the membrane's role in shaping its conformational landscape.

These findings deepen our understanding of viral fusion protein dynamics, offering molecular insights to inform vaccine and therapeutic design.

Table of Contents

Acknowledgements

This dissertation is the result of five and a half years of hard work and perseverance at UC Berkeley as well as the years of education preparing me for graduate school. None of this would have been possible without the support of my loved ones and community who have supported me through the years. Thank you to everyone who has helped me in the pursuit of this degree.

I would like to thank my advisor, Dr. Susan Marqusee, for all of her mentorship throughout graduate school. Susan always has great advice about science and non-science related matters all of which has shaped the past six years of my life. Susan, thank you for always saying yes when it came to new scientific ideas and directions and being excited by every new piece of data. Hearing “that was the best part of my day” when I shared a new result with you always made me feel valued. Susan has a gift to see where her efforts are needed, whether it's in mentoring a specific person in a tough place, organizing the research at the university during the pandemic or advising our nation’s science policy, and then gives it her all. We always say that Susan’s superpower is connecting with people, and this network is only there because she is a generous and action oriented person that accomplishes what she says she is going to do. I am so grateful that I decided to join your lab because throughout all of the hard things that have happened in the past five and a half years I always know that you will figure out how to best move forward.

I am thankful for all of the members of the Marqusee lab throughout my time at Berkeley. One of the reasons I felt confident in joining the lab was due to the wonderful community that the existing members had created. Dr. Ha Truong, Dr. Naomi Latorraca, Dr. Emma Carroll, Dr. Helen Hobbs, Dr. Charlotte Nixon, Dr. Shawn Costello, Dr. Natalie Dall, Dr. Miriam Hood and Dr. Sara Volz were the ones who showed me where everything was in the lab, planned social events and made me feel welcome and included. I had the honor of joining the lab at the same time as my fellow graduate students Darren Kahan and Eva Gerber and it has been such a joy working alongside them and seeing all of our projects grow and flourish. We added more postdocs during my time in the lab, in particular Dr. Carol Mendonça, Dr. Amir Bitran and Dr. Mark Petersen. All of whom brought great new ideas and perspectives into the lab. I must specifically thank Shawn Costello for being the best example of a peer mentor I have ever had. Shawn was my rotation mentor and then the two of us worked on the project in the second chapter of this dissertation together. Shawn is incredibly generous with his time to teach me new things, edit my writing and talk through confusing data. I am so lucky to have learned so much from Shawn before he graduated but also still to this day. Natalie Dall was another graduate student when I joined the lab and was a constant source of joy and encouragement even when things were very tough. Natalie is the master of troubleshooting and always gave me great ideas for how to fix my lab issues,

thank you Natalie for all of your support. Naomi Latorraca joined the lab right before I rotated and was another rotation mentor of mine. Since then she has been a constant source of advice, mentorship and someone to talk through hard concepts with. I am so excited to see all the work your new lab will accomplish with your mentorship and great ideas. Miriam Hood was one year ahead of me in graduate school and thus was the constant target of my “how do I navigate this bureaucracy” questions. Miriam is a brilliant scientist with strong morals who I admire greatly. Finally I would like to thank two undergraduate students I had the honor of mentoring, Tina Li and Megan Luo. Tina started working with me during her senior year so we did not have a long time to work together, but in her short time she learned so much and gained so much confidence in the lab that it felt like a much longer period than it was. Tina I am so proud of all that you have accomplished and I’m so excited to see where your own graduate school journey takes you. Megan started working with me during her junior year so we worked together for about two years. Megan is a brilliant scientist and her work was critical to the success of many of the projects in this dissertation as well as projects of her own. By the end of our time working together Megan was an accomplished biophysicist and was more of a peer than a mentee. Megan, thank you so much for all of your hard work and thoughtful analysis of our data. These projects would not be where they are without you. I am so excited to see how you change the world.

Furthermore, I have had the opportunity to work with wonderful collaborators throughout graduate school. I must first thank Dr. John Pak at the Chan Zuckerberg Biohub for all of his collaboration and mentorship. John had a large impact on all of my projects between making some of the protein for the studies, teaching me how to do cell culture work, providing scientific expertise on viruses and viral proteins, editing this dissertation and being a kind and generous human to work with. When the projects we wanted to pursue required resources and knowledge our lab did not have John quickly and generously invited me to learn new techniques in his lab. This was when I met Dr. Wesley Wu, another very impactful person on my Ph.D. Wes taught me how to express and purify proteins in insect cell culture and little did he know he also signed up for an incredibly challenging troubleshooting experience as the rabies virus glycoprotein was not an easy protein to work with. Wes is always generous with his time and very thoughtful in how he approaches experiments and I was always the beneficiary of his kindness. Another incredibly helpful collaboration was with Dr. Magnus Hoffmann and Dr. Kim-Marie Dam who I first met while they were at CalTech while Magnus was starting his lab. They very generously invited me to spend about a week with them learning how to express and purify the eVLPs, which if you read this thesis you will learn really changed the direction of my research and enabled me to do really amazing experiments. Magnus and Kim continue to be wonderful sources of advice and I am so excited to see how the eVLP technology changes the field of vaccines. Another

enriching collaboration was with Dr. Rosalie Lawrence with whom I developed an HDX-MS method to study eIF2B conformational changes which she was studying in her postdoc. This project was incredibly exciting and Rosalie is a wonderful collaborator and provided an exciting opportunity to combine biophysics with cell biology research. Best of luck with your new lab Rosalie, I look forward to seeing what you discover. Thank you to all of the collaborators and co-authors who have invited me to work on their very cool science. These were some of the most fun experiences I had in graduate school.

I owe my pursuit of education in protein biophysics largely to my undergraduate education at Johns Hopkins University in the Department of Biophysics. The education I received through this program was outstanding and made me a curious, thoughtful, hard-working scientist ready to take on graduate school. This journey largely started in my first-year there when I was unsure what I wanted to do and happened to attend a brief talk about the department hosted by Dr. Karen Fleming who convinced me that protein biophysics is fascinating and impactful and that it was what I wanted to pursue. The academic rigor and advising I received in this department was fantastic and I wish I could go back and retake so many of my courses as I am sure I would get more out of them again. My academic advisor Dr. Bertrand Garcia-Moreno helped me navigate the university and in my senior year, the graduate school application process. I am incredibly grateful for his guidance. Bertrand gave me one of the wisest insights which to paraphrase is “one of the best things about life is you do not get to know what your life would be like if you made the other decision”. I believe he told me this just to get me to finally decide on a graduate school, but this comes back to me time and time again in moments where I am overthinking things and distrusting myself. My research journey started at Hopkins when I responded to essentially a “want ad” sent out by Dr. Jesse Yoder who at the time was a graduate student and would become my research mentor when I worked in the lab of Dr. L. Mario Amzel and Dr. Sandra Gabelli. Jesse taught me so much about how to express and purify proteins, take various biophysical measurements and analyze data. This research was exciting and novel and was the perfect complement to my coursework and inspired me to go to graduate school. Mario and Sandra were wonderful professors to have as first advisors, they were both so welcoming to an inexperienced undergraduate and treated me like a full member of the lab and encouraged me to pursue the field. After Jesse graduated I was about to start my senior year and did not have another research opportunity in mind so I figured I would focus on finishing up and preparing my graduate school applications. I was in a seminar class with Karen who heard I did not have a lab to work in and she thought this was unacceptable and invited me to work with her and Dr. Pat Fleming so that I would have a “lab home” for my final year. By the time I graduated I realized how this offer was so important to my career as I had a place to seek advice, people to read applications and a place to go and chat about proteins. All of the members of the Fleming lab made my senior year incredibly special and it has been wonderful to keep in contact with

many of them. I also have to thank Karen for teaching me how to give a good presentation. Karen has strong opinions about how to give a clear and impactful presentation and she is right about all of them. From how to format slides, to how to answer questions after the presentation, Karen has coached me and everyone who has passed through her lab and classes on how to effectively communicate science and she should one day give a masterclass for all of the world to benefit. Hopkins was a wonderful place to grow as a scientist and a person and I am so thankful that I was able to pursue my undergraduate education there.

My high school education at Camas High School in southwestern Washington State was the reason why pursuing science education in college was possible. I was part of the CHS STEM magnet program and through this program had the opportunity to not only have a great education but also conduct independent scientific research and participate in internships. I have to especially thank Ron Wright and Kim Newman who both coordinated many aspects of this program and were wonderful advisors to me. Ron also coached our Science Olympiad team which I was a part of throughout high school and led us to do great things. We were state champions several times and attended the national tournament twice. This experience helped me learn about science and engineering outside of the classroom and taught me how to study and work hard.

My interest in science in my early education is all due to my family, especially my parents Cherie and Warren who raised me and my brother with the intention that we would pursue careers in STEM, even though neither of them are scientists. My parents' love for the natural world is vast and they raised us on trails, beaches and mountains and inspired us to study the world and how to improve it. As they are not scientists themselves, they often do not understand the goings-on of graduate school or scientific research but they were always supportive and excited for what I was accomplishing. My brother Eliot, who is two years older than me, was the guinea pig child so I had the benefit of learning from different things that he attempted. While we were not always the greatest of friends in our younger years and drove our parents crazy, I believe we pushed each other to work hard in school and achieve great things. Eliot’s career in engineering was the first half of fulfilling our parents' dream and we are all so proud of his hard work and the life that he and my lovely sister-in-law Isibael have built. My maternal grandparents, Lila and Jim Elliott, were influential in raising my brother and I as they lived on adjacent property to us and my many cousins. Many afternoons were spent fixing things around the farm with Grandpa and learning how to use tools, or baking and doing laundry with Grandma, learning how to care for myself and be independent. I learned many practical skills from my grandparents and was always encouraged to work hard to be “the smartest girl in school”. Similarly my paternal grandparents, Beverley and Bob Shoemaker were always taking the grandchildren to the theater, art museum, mountain, beach, and of course playing lots and lots of card

games. Most of my Shoemaker cousins can attest to much of our early math education being during high-stakes cribbage games with Grandfather where we quickly learned how cards add up to 15 and when probability of cutting into a double-run is high enough to throw a risky pair into the crib. Sadly Grandfather Shoemaker did not live to see the completion of this thesis but I know he would be so proud and interested to hear about all of this work. My Grandmother, Beverley, always supported my scientific interests but also helped me to balance this with artistic pursuits as well. My passion for ceramics, block printing and cooking are largely due to her love of art and I am so grateful for these balancing hobbies. All of my grandparents were very excited by and invested in my education and their pride in my success was always a motivating factor to keep going.

In addition to a wonderful family I am incredibly blessed to have fantastic friends. Thomas Matthews is one of my oldest friends and we met in high school and have stayed close friends even though we have not lived in the same city since. Thomas has always been one of my biggest cheerleaders and has always believed that I can achieve anything. My undergraduate years at Johns Hopkins University introduced me to some of the most wonderful people I have ever met, many of whom remain my biggest supporters and source of fun. Through the Johns Hopkins Outdoors Club/Experiential Education at JHU I met some of the most wonderful humans I have ever known: Karina Wohlhieter, Emma Weinert, AsiaLuna Patlis, Kyle Shannahan, Annie Britton, Allie Lemmer, Sammie Lemmer and numerous others. Together we learned technical skills of how to safely navigate caves, paddle canoes and stay warm in the freezing cold backcountry which led to some extreme bonding situations. We also learned soft-skills such as communication, organization, and group management, all of which have served us all greatly throughout our post-graduate lives. We have all gone on to do very different careers in different places yet we remain close and invested in one-another's lives. I was blessed that as I moved to Berkeley, Karina and Asia were also living in the area and our friendships grew much stronger as we started our adult lives. Although they both eventually moved on to pursue their own studies elsewhere in the country I will always be grateful for the support they provided during this period of my life. Another close Hopkins friend whose influence in my graduate school career has been great is Dr. Daisy Duan who was my primary study buddy while we were both studying biophysics as undergraduates. Daisy was also in graduate school at the same time as me at Yale. Seeing her at conferences and exchanging texts about the ups and downs of graduate school was always a refreshing moment and a reminder that hard things are inevitable but overcomeable. Finally during my graduate school years I have also formed some incredibly special friendships. Vinson Fan and I became friends through the trial by fire experience of being the co-chairs of the MCB graduate student organization. We both had a great desire to make elections as democratic as possible and make all voices heard and through this became good friends. Vinson is a very

thoughtful and talented scientist and his support of me as a scientist and a person is greatly appreciated. Héctor Torres Vera is actually a friend I met while we were both undergraduates but we became much closer when we became roommates at Berkeley after he joined the same graduate program the year after me. Thus Héctor and I weathered much of the pandemic together and it has been so wonderful to see him grow as a scientist and human being. Héctor always has great thoughts about the world and science and is always a good person to bounce ideas off of. His empathy and joy are infectious and make me a better person. Finally, I have to specifically thank Laura and Kyle Kovacs who I met in my first year of graduate school. Kyle and Laura became good friends with Tim and I as the four of us enjoyed playing board games. Little did we know when the COVID-19 pandemic would start in a few short months our affinity for board games would be a lifeline of human interaction as we would play online board games and enjoy one another's company on zoom several nights a week. After the pandemic quieted down our friendship became about more than just rolling dice and building card decks and we now share many hobbies, lots of good food and conversation. Our dogs, Floyd and Kat, are best dog friends and Floyd taught Kat many valuable lessons such as the fun of peeing on trees and how to play tug. Laura is an incredibly talented ceramicist and I started ceramics again at her invitation to take a class together. We now do ceramics together in her home studio and spend hours solving the world's problems over conversation while throwing on the wheel and glazing mugs. The six of us love hiking and we have hiked most of the dog-friendly trails in the east bay as well as traveled to beautiful places including Joshua Tree and the Sierras to find the most scenic vistas and interesting plants. The support of the Kovacs has been such a blessing during graduate school and I am so thankful for our friendship.

Another source of friendship and community has been the San Francisco Bay Area Curling Club. Tim and I began curling in 2022 after we took a class and thought it could be a fun shared hobby. We are now hooked and at some points in the past few years we have been there most nights of the week playing in league, volunteering and teaching others how to curl. It is wonderful to be part of a diverse community of people with different life experiences to remember the world is bigger than graduate school. As a volunteer run club, the hard work and dedication of everyone is inspiring. Weeknight leagues have been a wonderful escape from the stress of graduate school to just have fun for a few hours and work to improve on something not related to proteins or presentations.

I would also like to thank my partner Tim's family for all of their love and support over the years. Thank you Virginia, Chuck, Elayna, Grace and all of the extended families on all sides. Tim and I started dating a few months before the pandemic, so by the time I was actually able to meet his family our lives were already very intertwined. Many members of Tim's family including his parents and sister have science

backgrounds and thus have been very understanding and supportive of me through the ups and downs of graduate school. Everyone is always excited to hear what has been going on in the lab and loves sharing fun science things with me. The family visits throughout the years have been a consistent source of fun and love and I truly think I have hit the in-law lottery.

Finally I have to thank my partner (fiancé at time of writing) Tim Foster. Tim and I met shortly after I started graduate school, I was rotating in the Marqusee Lab at the time, so there is not much of this journey that he was not present for. Tim I love you so much and your support has made this journey so much easier and enjoyable. Coming home after a long day and being told that I'm doing a good job even when things feel impossible was often what I needed to keep going. Thank you for being the best co-parent of our crazy dog named Kat. Sitting on the couch with the two of you at the end of the day always re-energizes me and fills me with such joy. Thank you for traveling the world with me and showing me your favorite places whether in Ireland or Cleveland. You are a brilliant and hard working person and inspire me to be the best version of myself. I love this life that we have built together and I appreciate everything that you do to make our lives better. I am so lucky to have a partner like you and I am excited to see what the future brings for us.

Chapter 1

Overview of Viral Fusion Proteins and Approaches for Studying Their Conformational Landscapes

---

1.1 Viral fusion proteins catalyze membrane fusion between the viral and host-cell membranes

Almost all enveloped viruses rely on a fusion protein to infect cells. After binding of the host cell receptor by the fusion protein or a distinct host-cell recognition protein, a hydrophobic fusion peptide or loop from the fusion protein will anchor into the host-cell membrane and then the fusion protein facilitates the combining of the host and viral membranes into one membrane, allowing the viral contents to infect the cell. Since the fusion of two membranes has a high energetic barrier, the virus-host cell membrane fusion relies on the fusion protein to act as a catalyst to overcome this barrier. Fusion proteins of enveloped viruses are typically categorized into three classes: class one includes viruses such as influenza and coronaviruses, class two comprises flaviviruses and alphaviruses, while class three includes rhabdoviruses and herpesviruses. These

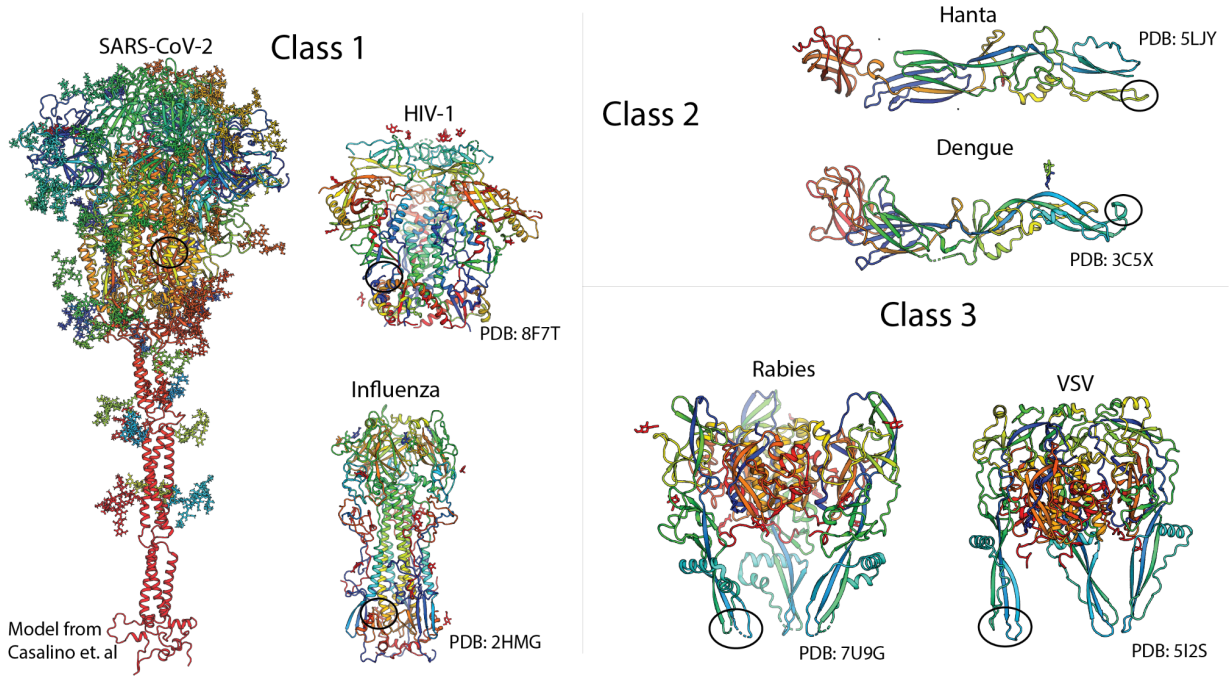

Figure 1: Several examples of each class of viral fusions colored from N -> C terminus in blue to red for each chain. The approximate location of the fusion peptide is indicated with a black oval.

classes are primarily differentiated by: the arrangement of fusion loops within the oligomer, the predominant secondary structures of the monomers, the orientation of the protein relative to the membrane, and the necessity for proteolysis to achieve fusion (*1*–*3*).

Class 1 viral fusion proteins are trimeric with fusion peptides initially buried within the trimer. The long axis of the fusion proteins are oriented perpendicular to the membrane and are predominantly alpha-helical (*4*–*7*). In most class 1 fusion proteins, the polypeptide chain is cleaved into individual subunits (*4*–*6*) and some require proteolysis to release the fusion peptide (*5*). Class 1 viral fusion proteins typically have two domains, one responsible for recognizing the host cell receptor and the other for catalyzing fusion after the triggering event (*4*, *5*, *7*). Class 1 virus fusion proteins have a variety of triggers that result in release of the fusion peptide, including low pH, as seen with hemagglutinin (*4*), receptor binding, such as with HIV-env (*8*), and a combination of receptor binding and cleavage by a protease, such as with coronavirus spike proteins (*5*). For certain class 1 viral fusion proteins, like RSV, the triggering mechanism remains unknown (*6*). The release of fusion peptides in class 1 fusion proteins is irreversible, often described as a "harpoon" anchoring into the cell membrane (*9*).

In contrast, class 2 viral fusion proteins are typically dimeric, predominantly composed of beta sheets that lie parallel to the viral membrane (*10*). The fusion loops in these proteins are concealed under a domain of the other chain in the dimer. The viruses typically enter the cell through endocytosis. Upon acidification in the endosome, the viral fusion proteins activate by dissociating into monomers, rotating to a perpendicular orientation relative to the viral membrane and then trimerizing before facilitating membrane fusion (*10*). In some viruses with class 2 fusion proteins, such as Dengue virus (a flavivirus), the fusion protein also serves as the receptor-binding protein (*11*). In contrast, other viruses with class 2 fusion proteins, like the Semliki Forest virus (an alphavirus), use separate proteins for receptor recognition and viral fusion (*12*).

Class 3 viral fusion proteins exhibit characteristics of both class 1 and class 2 (*1*, *13*). These trimeric fusion proteins feature a mix of alpha helices and beta sheets and are oriented perpendicularly to the viral membrane. The fusion loops are on the exterior of the protein but are oriented toward the viral membrane (*14*–*18*). Class 3 fusion proteins have a variety of triggers, the G protein of rhabdoviruses is triggered by a drop in pH during endosomal entry (*19*, *20*), whereas herpesvirus gB proteins appear to require a decrease in pH, interaction with other viral surface proteins (gD, gH/gL), and receptor recognition (*13*).

Despite the structural diversity of fusion proteins, their mechanisms of fusion are remarkably similar. All fusion proteins exhibit a prefusion conformation, where fusion loops are not in a position ready to anchor into a membrane, an extended intermediate conformation, where the fusion loops are exposed and positioned to interact with the host membrane, and a post-fusion conformation, where the fusion loops and

transmembrane helices have come together to facilitate the merging of viral and host membranes (*1*, *3*, *12*). This series of conformational changes start with the protein in the prefusion state, followed by a triggering event that induces refolding into the extended intermediate conformation. The protein then collapses into a hairpin structure, drawing the membranes close together to initiate fusion. Ultimately, upon completion of the collapse, a pore is formed between the two membranes, allowing the viral contents to mix with the cytoplasm of the target cell (*1*, *3*, *12*) (Figure 2). Generally, each conformational change is effectively irreversible, with the notable exception of some class three viral fusion proteins within the Rhabdoviridae family, which can reversibly interconvert between the prefusion and extended intermediate states (*14*, *18*, *21*, *22*).

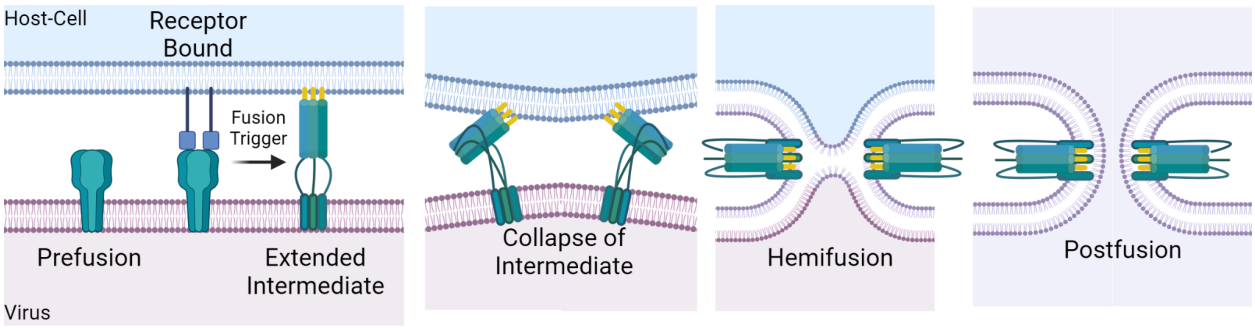

Figure 2: Generic Mechanism of Viral Membrane Fusion. Proteins start in the prefusion conformation where they are able to interact with the host-cell receptor protein (if one is necessary). There is then typically a trigger for fusion which could be a drop in pH, proteolysis or interaction with a companion protein. This then leads to the formation of the extended intermediate where the fusion loops will bury in the host-cell membrane. These intermediates will then begin to collapse and if enough are present in one area this will lead to the membrane being brought close together which eventually will lead to hemifusion, where membrane mixing will begin until a pore is formed, at this point the fusion protein is in the postfusion conformation. Adapted from Harrison *et. al* (*1*), created in Biorender.com

1.2 Viral fusion proteins are often the immunogenic determinant of viruses and thus the target of therapeutics

Viruses exhibit a remarkable diversity in their surface protein composition. Some, such as herpesviruses and influenza, display multiple large proteins on their surfaces (*13*, *17*, *23*). In contrast, others, like rhabdoviruses and coronaviruses, typically present only a few proteins, with the viral fusion protein being the largest and most abundant (*5*, *24*, *25*). Due to their essential role in the fusion process, viral fusion glycoproteins are often targeted by vaccines and therapeutics, as they can be inhibited by antibodies and small molecules to prevent infection (*26*).

Current vaccines are predominantly designed to target viral fusion proteins, including all available COVID-19 vaccines (*27*–*31*), the vaccines for respiratory syncytial virus (*32*) and shingles/herpes zoster (*33*, *34*). Some vaccines that use live, attenuated, or inactivated viruses generate a high titer of antibodies toward the fusion protein of that

virus as compared to other viral surface proteins, as seen with influenza (*35*). In other cases, such as mumps, the primary antigen is not the fusion protein but the receptor-binding protein (*36*). In mumps, while neutralizing antibodies target the fusion protein (F), they are typically produced in lower titers compared to those against the hemagglutinin/neuraminidase (HA/N) proteins.

In addition to vaccines, small molecule therapeutics are available that target various viral components during different lifecycle stages, including inhibitors of SARS-CoV-2 M_{Pro} (*37*), HIV antiretrovirals, and PrEP treatments (*38*). Antibody treatments, however, generally target surface proteins, particularly fusion and receptor-binding glycoproteins (*39*, *40*). Antibodies neutralize viruses through several distinct mechanisms (Figure 3). One common mechanism is blocking receptor binding. For example, the REGN-COV2 antibody cocktail effectively prevents SARS-CoV-2 from binding to ACE2, its cellular receptor, by using two antibodies that both bind to the receptor binding domain (RBD) and block the binding of ACE2 (*41*). Additionally, antibodies may hinder host-cell recognition without binding to the receptor-binding motif but instead by inducing conformational changes (*42*) or sterically obstructing access to the host-cell surface (*43*). Another neutralization mechanism involves inhibiting fusion after the virus has attached to the host cell. An antibody against West Nile virus, for example, does not block attachment but instead prevents the necessary conformational changes for fusion, even inhibiting fusion within the endosome (*44*, *45*).

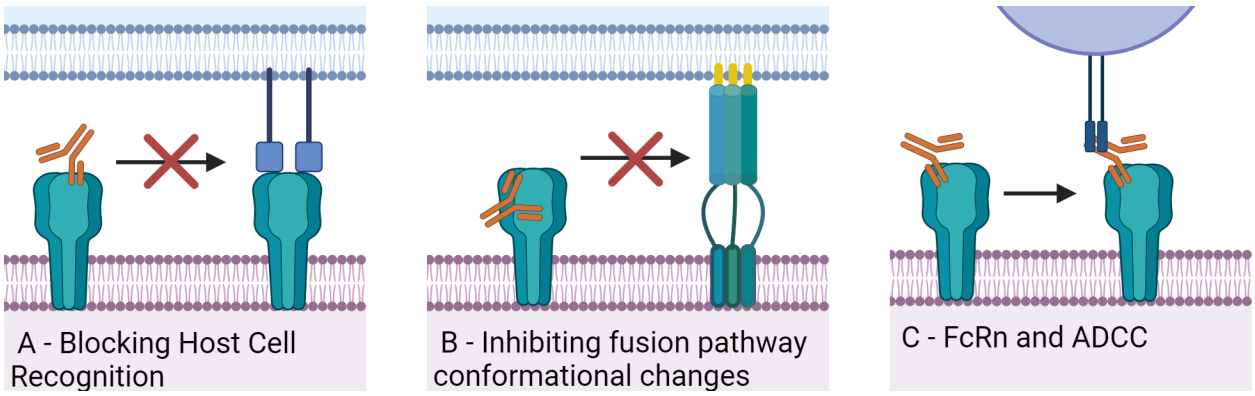

Figure 3 Mechanisms of Antibody Neutralization
(A) By preventing a viral fusion protein from recognizing its host-cell receptor an antibody can prevent infection. This can occur by directly blocking the receptor binding motif or by binding somewhere that prevents or induces a conformational change not conducive to receptor binding. (**B**) Neutralizing antibodies can bind to specific places on viral fusion proteins and prevent necessary conformational changes on the fusion pathway, such as to the extended intermediate or preventing foldback which leads to hemifusion. Binding directly to the fusion protein will also prevent the formation of the extended intermediate and lead to neutralization. (**C)** Some antibodies neutralize due to Fc effector functions and antibody body cellular cytotoxicity which happens with the constant region of the antibody is recognized by immune cells which then directly kill cells.

Similarly, an antibody targeting chikungunya virus was found to inhibit fusion by preventing the release of fusion loops after viral binding (*46*). Lastly, some antibodies mediate neutralization through antibody-dependent cell cytotoxicity (ADCC), which relies on Fc effector functions (*47*). A notable example is S309, the parent antibody of sotrovimab, which neutralizes SARS-CoV-2 by binding to its spike protein and stimulating Fc effector functions. This antibody has demonstrated *in vivo* effectiveness against infection even after its binding affinity and in vitro neutralization diminished due to viral mutations, suggesting an ADCC mechanism of action (*48*).

1.3 Viral fusion protein conformational dynamics are important for vaccine design

Viral fusion proteins are highly dynamic, undergoing a series of conformational changes to facilitate membrane fusion (*1*, *3*, *49*) (Figure 2). The process begins with host-cell recognition, where certain fusion glycoproteins, including those from beta coronaviruses, possess RBDs that can exist in either a binding-competent "up" conformation or a binding-incompetent "down" conformation (*50*). This conformational transition can occur on a range of timescales, from milliseconds to seconds (*51*). Once a host cell is recognized, a triggering event induces a conformational change that exposes fusion loops, allowing them to interact with the host-cell membrane. This state is often referred to as the extended intermediate conformation (*1*). Following insertion of the fusion loops into the host membrane, the fusion proteins undergo another significant conformational shift from the extended intermediate to the post-fusion conformation, leading to the formation of a fusion pore (*1*).

Understanding these conformational changes is crucial for designing targeted vaccines and therapeutics, as different conformations expose distinct surface areas that can be targeted by the immune system, monoclonal antibodies and other therapies (*17*, *26*). In vaccine development, significant efforts have been made to engineer fusion proteins to limit their conformational landscape, thus directing the immune response toward the most efficacious neutralizing conformations (*6*, *17*, *26*, *32*, *52*, *53*). Early research on hemagglutinin found that mutating residues involved in coiled-coil formation in the post-fusion conformation to proline prevents the fusion of cells expressing the mutated protein (*54*). This concept has since been generalized to other fusion proteins that also form coiled coils in their post-fusion states, including those of Respiratory Syncytial Virus (RSV) (*55*), Middle Eastern respiratory syndrome coronavirus (MERS-CoV) (*56*) and SARS-CoV-2 (*32*, *57*, *58*). These efforts have led to the development of immunogens that elicit effective antibody responses. In further designs for the SARS-CoV-2 spike protein it was found that including additional prolines lead to increased expression and solubility (*52*). Another design campaign led to additional mutations to lock the receptor binding domains down into the receptor binding incompetent conformation using disulfide bonds to improve antigen stability; however, vaccines with this construct were found to produce lower titers of neutralizing antibodies

as opposed to constructs where the RBDs were not constrained (*59*). In recent RSV vaccine design, mutations were also made to prevent the protein from adopting the post-fusion conformation. It was found that a combination of disulfide bond introduction, cavity-filling mutations, and mutating out charges led to a highly stable antigen that elicited a strong neutralizing antibody response in animal trials (*32*) and conferred protection against RSV infection in human clinical trials (*60*).

1.4 Viral fusion proteins exist in complex environments

Reductionist approaches to studying viral fusion proteins *in vitro* have led to significant discoveries, but they also come with caveats that must be addressed in order to fully understand the potential conformational landscape of these proteins. One major limitation is that these membrane proteins are often examined using truncated soluble constructs (*6*, *9*, *15*, *18*, *32*, *52*, *53*, *61*). The chemical environment experienced by these synthetic constructs is far different from the physiological environment experienced when on the virus. Viral fusion proteins are membrane proteins, which spatially constricts the protein in close proximity to a highly charged surface and restricts its degrees of freedom. Such characteristics can significantly influence the fusion proteins conformational landscape. (*62*, *63*). The membrane environment also limits access to certain membrane-proximal epitope regions (MPERs), meaning that antibodies that bind effectively to MPER-containing soluble constructs may not neutralize the virus, as their epitopes may not be accessible on the viral surface (*64*, *65*). Additionally, the density of glycoproteins on the viral surface can affect both the conformational landscape and the immune response. For example, HIV-1 has a low copy number of its env glycoprotein (approximately 7-14 copies per virus), which is thought to reduce avidity effects and shield the virus from B-cell immune responses (*65*). In contrast, viruses like VSV, RABV, and influenza have densely packed glycoproteins. In influenza, the immunodominant globular head domain of hemagglutinin is targeted by strain-specific antibodies, while antibodies directed at the conserved stalk domain are often immuno-subdominant, leading to less robust responses. One proposed reason for this is that the MPER is less accessible on the crowded viral surface, resulting in a diminished B-cell response to the stalk region (*35*).

Furthermore, although viral fusion proteins are typically multimers, they are sometimes expressed and studied as monomers for experimental simplicity (*18*). This simplification can obscure the significant effect of multimerization on conformational dynamics. Additionally, viral fusion proteins are often heavily glycosylated, and the glycosylation patterns observed on viruses may differ from those expressed recombinantly in laboratory cell lines (*66*). For instance, the glycosylation pattern of the SARS-CoV-2 spike protein has been shown to modulate the conformational dynamics of the RBD (*67*). Therefore, glycosylation patterns must be carefully considered, especially when expressed in non-native host species (e.g., insect versus mammalian cells).

Ideally, viral fusion proteins should be studied in native-like contexts that account for these variables. However, studies on actual viruses are limited to techniques that can be performed in high-biosafety-level laboratories. Consequently, many informative structural and biophysical techniques necessitate modifications to study fusion proteins in soluble constructs, virus-like particles, or pseudoviruses. When designing experiments, it is essential to consider how to leverage different techniques in a complementary manner to mitigate the limitations inherent in each individual approach.

1.5 Methods to study the conformational landscape of viral fusion proteins

A variety of methods have been employed to investigate the biophysics of viral fusion proteins, each offering unique insights while possessing distinct strengths and limitations. In this section, I will discuss several prominent techniques, though nearly every imaginable biophysical method has been utilized to study these proteins or their individual domains.

X-ray crystallography (*68*–*72*), cryo-electron microscopy (cryo-EM) (*15*–*17*, *32*, *52*, *53*, *73*) and cryo-electron tomography (cryo-ET) (*74*–*78*) have all been used to determine the three-dimensional structures of viral fusion proteins. These structural insights help elucidate the various domains and their collaborative roles in the fusion process. Structure-based guided design has also been effective in identifying mutations that stabilize fusion proteins in specific conformations (*26*, *52*, *53*, *73*). Furthermore, structural methods have been valuable in determining antibody epitopes and leading to a better understanding of why some antibodies are neutralizing and some are not (*72*, *79*). However, these techniques come with inherent biases regarding the conformations they can visualize. X-ray crystallography requires a fairly static and uniform protein conformation in order to crystallize, often resulting in the determination of only a single conformation. Many viral fusion proteins are highly flexible, making crystallization difficult. Cryo-EM can resolve multiple distinct conformations, but each must be sufficiently populated to produce an average model. For instance, cryo-EM successfully captured various structures of the SARS-CoV-2 spike protein with receptor-binding domains in either "up" or "down" position (*76*, *80*, *81*). On the other hand, conformational changes that lead to highly flexible states or are minorly populated will not be easily captured through cryo-EM. Cryo-EM also cannot determine changes in flexibility as the model is static and averaged. Moreover, cryo-EM typically requires proteins to exceed a certain size for structural resolution (*82*). While this limitation is usually not a concern for trimeric viral fusion proteins, flexible domains and smaller constructs may fall below the threshold for visualization. Antibodies can be used to increase particle mass, but their inclusion may bias the protein's conformation relative to the apo state. Another issue with studying viral fusion proteins with cryo-EM is that some proteins have a preferred orientation on cryo-EM grids which biases the sample and can lead to incomplete reconstructions, this has in particular been noted as an

issue for influenza hemagglutinin (*83*). Cryo-ET offers the advantage of studying proteins in a native environment, such as on actual viral membranes, vesicles, or cells (*74–78*, *84*), but typically at lower resolution compared to other structural methods. Regardless, structural information on viral fusion proteins is invaluable for understanding their functions and enhances the interpretative power of complementary techniques by linking results back to structural insights.

Another common method to study the conformations of viral fusion proteins involves testing the binding of conformationally specific antibodies under varying conditions (*16*, *85–87*). This approach is relatively straightforward once the antibody's behavior is understood. However, since these experiments assess binding to a single epitope, they can only indicate whether that epitope has changed in a way that affects binding. Given the large, multi-domain nature of viral fusion proteins, a single epitope is unlikely to capture all possible conformations. Although multiple conformationally specific antibodies can be employed, their co-binding may be limited by the locations of their respective epitopes (*73*). These antibodies have been utilized to investigate various stages of the viral fusion process (*16*), offering a high-throughput alternative to other assays. However, the binding of an antibody—or lack thereof—does not guarantee that fusion has occurred; it merely indicates that a specific epitope has formed or altered.

Single-molecule FRET (smFRET) has been employed to explore the dynamic properties of viral fusion proteins. For example, smFRET successfully measured the opening and closing rates of the receptor-binding domain in the SARS-CoV-2 spike protein, revealing that this conformational change occurs on the millisecond timescale and quantifying the relative populations of "up" and "down" RBDs (*51*). smFRET is a challenging experiment that requires introduction of large fluorescent labels into the protein, which is both technically challenging and could unintentionally change the dynamics of the protein.

Finally, hydrogen-deuterium exchange monitored by mass spectrometry (HDX-MS) has been widely used to study various aspects of viral fusion proteins and is the primary technique employed in this dissertation (*88*). HDX-MS allows direct examination of the dynamics of fusion proteins using pulse-labeling techniques (*9*) and provides insights into local stability under different conditions (*61*), revealing how conformations and stability are influenced by factors such as antibody binding, pH, and receptor interactions. This technique offers the advantage of not requiring external labels or large quantities of protein, enabling the study of viral fusion proteins across a diverse range of solution conditions. Furthermore, HDX-MS reports on the entire solution ensemble and therefore does not rely on sample homogeneity nor is it biased to a specific conformations. The next section of this chapter will delve deeper into the specifics of this technique and its advantages and disadvantages compared to these other methods.

1.6 Hydrogen-deuterium exchange monitored by mass spectrometry and its application to viral fusion proteins

Hydrogen deuterium exchange mass spectrometry (HDX-MS) is a powerful technique for studying viral fusion proteins in native-like environments. Hydrogen-deuterium exchange occurs when a protein or mixture of proteins is diluted into a buffer containing heavy water (D_2O). The amide hydrogens of the protein backbone can exchange with deuterons in the solvent (*89*) (Figure 4). Amides can only exchange when they are not forming hydrogen bonds and are solvent exposed. This exchangeable state is referred to as the "open" state, while the unexchangeable state is referred to as the "closed" state. The rate at which an open amide will exchange is known as the intrinsic rate (k_{chem}), which is influenced by temperature, pH, salt concentration, as well as the local primary sequence, the amino acid identities of that residue and its nearest neighbors (*90*). Depending on the rate of opening (k_{op}) and closing (k_{cl}) at each individual amide site as well as the intrinsic rate, the observed rate of hydrogen exchange ($k_{observed}$) either reports on the opening rate of an amide, EX1

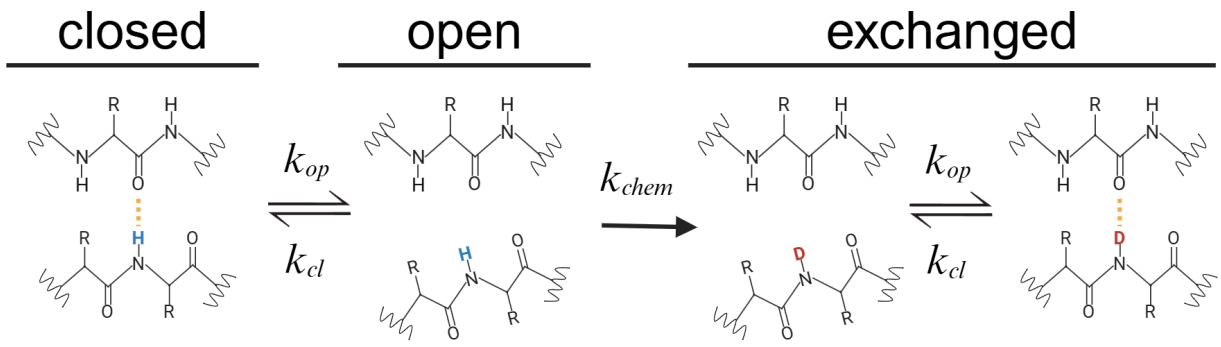

$$k_{observed} = \frac{k_{op} \bullet k_{chem}}{k_{op} + k_{chem} + k_{cl}} \quad if \quad k_{cl} >> k_{op}$$

EX1 $$k_{observed} = k_{op} \quad if \quad k_{cl} >> k_{op} \;\&\; k_{cl} << k_{chem}$$

EX2 $$k_{observed} = \frac{k_{op}}{k_{chem}} \bullet k_{chem} = \mathrm{K_{op}} \bullet k_{chem} \quad if \quad k_{cl} >> k_{op} \;\&\; k_{cl} >> k_{chem}$$

Figure 4 The Linderstrom-Lang model of hydrogen exchange and the equations for the observed rate of hydrogen exchange in different regimes.

conditions: when the intrinsic rate is much faster than the closing rate, or reports on the stability of the hydrogen bond that amide is involved in, EX2 conditions: when the intrinsic rate is slower than the rate of closing (*91*).

Both regimes can help answer interesting questions about protein stability and conformational dynamics. Typically, a time course of exchange is monitored. Several techniques can be employed to determine the degree of deuterium incorporation at each amide, including NMR, small-angle neutron scattering (SANS), infrared spectroscopy and liquid chromatography coupled with mass spectrometry (LC-MS). The focus of this dissertation will be on measuring HDX using LC-MS (Figure 5). In this case, reactions are quenched after specified times of incubation in D_2O by introducing

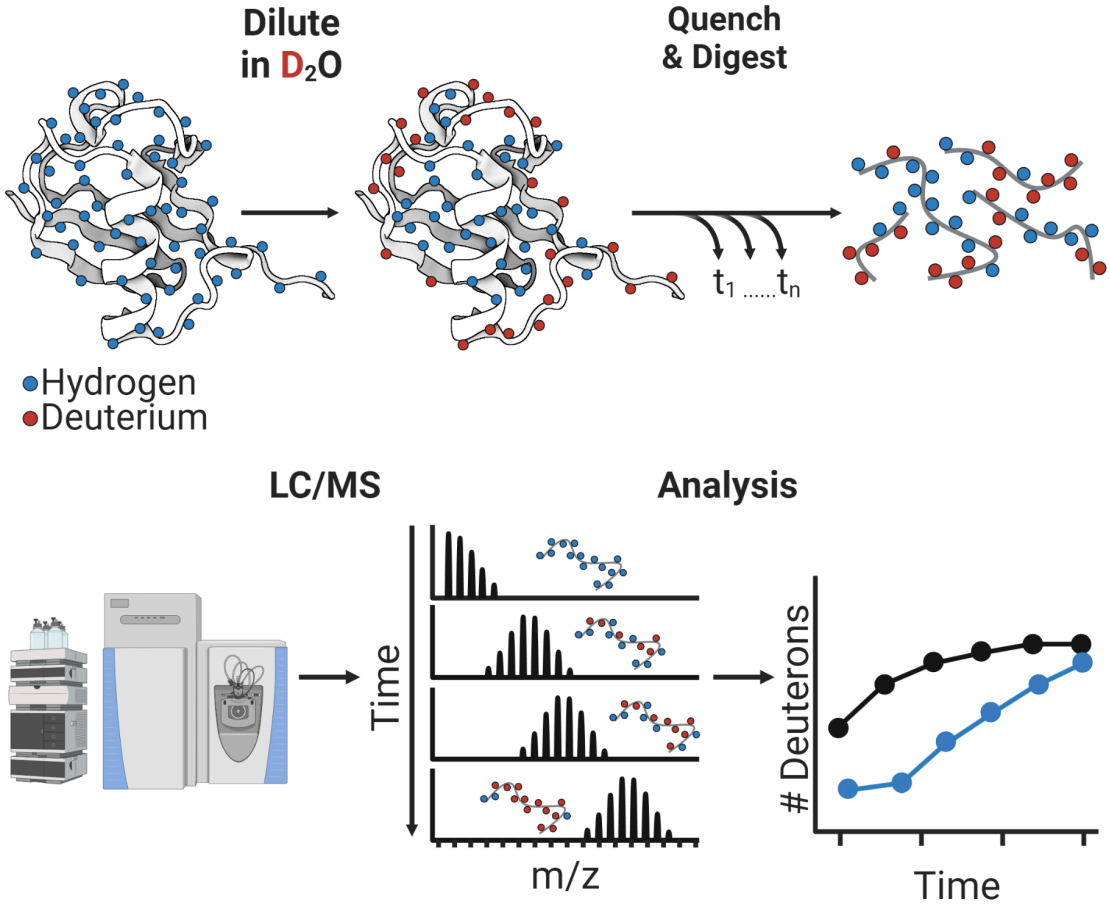

Figure 5 Hydrogen-deuterium exchange monitored by mass spectrometry
In every protein there is a labile hydrogen along the amide backbone which will exchange with deuterons from the solvent once the protein is diluted into a deuterated buffer. The exchange is quenched at timepoints by lowering the temperature and the pH. At this point timepoints can be stored at -80 ºC until LC-MS. The frozen timepoints are thawed and then injected over immobilized non-specific acid protease columns to be cleaved into individual peptides. The peptides are then massed by a mass spectrometer. The mass spectrometry data from a timecourse of exchange has an isotope distribution for each timepoint that goes up in m/z (mass to charge ratio) as more deuterium is incorporated. This data is analyzed in a variety of ways including taking the centroid of the distribution and plotting it over time.

an ice-cold buffer that lowers the pH to approximately 2.5, minimizing the rate of hydrogen exchange. The quenched time point can be stored at -80 ºC after being frozen in liquid nitrogen before measuring deuterium incorporation. The quenched HDX samples are usually digested into peptides using non-specific acid proteases (e.g., porcine pepsin, nepenthesin II, aspergillopepsin). Analyzing HDX data at the peptide level allows the data to be interpreted at a local (peptide) level. The resulting peptides are separated on an analytical column and eluted through a gradient of aqueous and non-aqueous buffers (such as acetonitrile). As each peptide elutes, it is injected into the mass spectrometer (MS) to collect the isotope distribution. The average number of incorporated deuterons is then determined by subtracting the natural isotopic abundance from the deuterated spectra. These data can be analyzed in various ways to draw meaningful conclusions.

Mass spectrometry is particularly well-suited for measuring deuterium uptake in viral fusion proteins because it requires relatively small amounts of sample (micrograms to milligrams, depending on the experiment) and unlike NMR does not necessitate isotopic labeling of the nitrogen and/or carbon in the protein backbone. Additionally, NMR requires a larger quantity of protein, typically expressed recombinantly in *E. coli*, which is often not feasible for full-length viral fusion proteins. Additionally, mass spectrometry is compatible with complex protein and solution conditions, including glycosylation, large protein complexes, and various binding conditions (e.g. detergent solubilization or antibody binding). HDX-MS does not have protein size limitations and can be used with highly flexible, heterogeneous protein populations. Mass spectrometry is sensitive enough to monitor high energy populations that are often missed by structural techniques such as cryo-EM and x-ray crystallography.

Mass spectrometry lacks the single amide resolution provided by NMR, instead reporting deuterium incorporation at the peptide level. With sufficient peptide coverage, it is possible to computationally extract single amide exchange rates (*92*, *93*), but for most applications, peptide-level data suffices, particularly in comparative hydrogen exchange studies (e.g., comparing conditions such as apo vs. bound, wild type vs. variant, or differing pH levels). On the other hand, mass spectrometry visualizes the entire isotopic distribution, allowing for the identification of bimodal data that may arise from EX1 behavior or the presence of multiple conformations. This capability, which will be further discussed in later chapters, underscores mass spectrometry's suitability for studying complex systems.

Prior to and alongside this dissertation, HDX-MS has been employed by others to investigate viral fusion proteins. Notably, work by Lee and colleagues revealed molecular rearrangements in influenza hemagglutinin (HA) during fusion through pulse labeling experiments triggered by a pH drop. Their findings indicated a series of intermediates forming upon acidification and demonstrated that the pathway to fusion differs between HA on a virus and soluble HA cleaved from the viral surface (*9*).

Additionally, Lee and colleagues conducted HDX-MS on HIV envelope protein (env) from various strains, discovering that different epitope regions exhibited varying exchange behaviors across different backgrounds (*61*). This work has important implications for understanding how viruses are recognized and neutralized by the immune system.

1.7 Summary of dissertation work

In this dissertation, I present my research addressing key questions related to the conformational landscape of viral fusion proteins. The first chapter describes work from a co-first author paper with Dr. Shawn Costello, where we investigated the SARS-CoV-2 spike protein's conformational dynamics. During our HDX-MS experiments aimed at mapping epitopes for collaborators, we discovered that the spike protein samples an open-trimer conformation. In this state, which is still trimeric, each monomer remains well-folded but no longer forms contacts at the trimer interface, exposing previously buried surfaces to the solvent. This intriguing finding emerged when we observed two isotopic distributions for certain peptide spectra (bimodal behavior), which deviated from the expected unimodal distributions. After ruling out various potential artifacts, we concluded that these distributions represented two distinct conformations: the canonical closed trimer (prefusion) and the newly identified open trimer. We further explored how factors like temperature, receptor binding, antibody binding, and sequence influence this conformational change.

Following this work, I engaged in collaborations with research groups around the world that discovered antibodies or nanobodies purportedly recognizing this open trimer conformation. These collaborations yielded valuable insights, revealing both successful and unexpected interactions, furthering our understanding of the conformational landscape of this viral protein and resulted in several publications with me as a co-author.

In the second chapter, I addressed the unresolved question of how the membrane environment affects the conformational landscape of the spike protein. Our initial experiments used the S-2P construct, an engineered variant designed for easier experimental handling, featuring a soluble trimerization domain and specific mutations to stabilize the prefusion conformation. To better understand the effects of these engineered features, I compared S-2P with enveloped virus-like particles (eVLPs) displaying constructs both with and without the stabilizing prolines, the furin cleavage site, and the D614G mutation—an early SARS-CoV-2 spike protein mutation that became fixed worldwide. My findings revealed that native multibasic furin has two effects, it leads to an allosteric loosening of the S2’ cleavage site, which may enhance TMPRSS2 activity and could be why viruses are more infectious with the multibasic furin site. The other effect is that cleavage at the S1/S2 site increases the equilibrium population of the open-interface trimer relative to the prefusion conformation.

Interestingly, the D614G mutation appeared to counteract these effects by stabilizing the prefusion conformation. This suggests that the virus may have acquired the D614G mutation to mitigate the destabilizing influence of the furin cleavage site, which could otherwise lead to non-functional spikes.

The final chapter of my dissertation focuses on the Rabies Virus glycoprotein, a class III viral fusion protein that uniquely samples both the prefusion and extended intermediate conformations at physiological pH. I developed an HDX-MS method specifically to study this conformational change, aiming to elucidate how mutations and antibody interactions affect the equilibrium between these states, both in soluble constructs and in the eVLP system. While this project is on-going, we have learned that the membrane stabilizes the prefusion conformation and that many mutations we thought would affect the conformational landscape of the protein do not. The one class of mutations that do seem to have an effect are helix breaking mutations that somewhat stabilize the prefusion conformation, although not as dramatically as other labs have reported.

Through the studies presented in this thesis, I contributed to a deeper understanding of viral fusion proteins, their dynamics, and the implications for vaccine and therapeutic design. Each chapter builds upon the last, exploring various aspects of conformational changes in viral proteins and their biological significance.

1.8 References

1. S. C. Harrison, Viral membrane fusion. *Nat. Struct. Mol. Biol.* **15**, 690–698 (2008).
2. M. Kielian, F. A. Rey, Virus membrane-fusion proteins: more than one way to make a hairpin. *Nat. Rev. Microbiol.* **4**, 67–76 (2006).
3. J. M. White, S. E. Delos, M. Brecher, K. Schornberg, Structures and Mechanisms of Viral Membrane Fusion Proteins. *Crit. Rev. Biochem. Mol. Biol.* **43**, 189–219 (2008).
4. S. J. Gamblin, S. G. Vachieri, X. Xiong, J. Zhang, S. R. Martin, J. J. Skehel, Hemagglutinin Structure and Activities. *Cold Spring Harb. Perspect. Med.* **11**, a038638 (2021).
5. F. Li, Structure, Function, and Evolution of Coronavirus Spike Proteins. *Annu. Rev. Virol.* **3**, 237–261 (2016).
6. J. S. McLellan, W. C. Ray, M. E. Peeples, Structure and Function of RSV Surface Glycoproteins. *Curr. Top. Microbiol. Immunol.* **372**, 83–104 (2013).
7. J. J. Skehel, D. C. Wiley, Receptor binding and membrane fusion in virus entry: the influenza hemagglutinin. *Annu. Rev. Biochem.* **69**, 531–569 (2000).
8. B. S. Stein, S. D. Gowda, J. D. Lifson, R. C. Penhallow, K. G. Bensch, E. G. Engleman, pH-independent HIV entry into CD4-positive T cells via virus envelope fusion to the plasma membrane. *Cell* **49**, 659–668 (1987).
9. M. A. Benhaim, V. Mangala Prasad, N. K. Garcia, M. Guttman, K. K. Lee, Structural monitoring of a transient intermediate in the hemagglutinin fusion machinery on influenza virions. *Sci. Adv.* **6**, eaaz8822 (2020).
10. Y. Modis, “Class II Fusion Proteins” in *Madame Curie Bioscience Database [Internet]* (Landes Bioscience, 2013; https://www.ncbi.nlm.nih.gov/books/NBK154547/).
11. K. I. P. J. Hidari, T. Suzuki, Dengue virus receptor. *Trop. Med. Health* **39**, 37–43 (2011).
12. M. Kielian, C. Chanel-Vos, M. Liao, Alphavirus Entry and Membrane Fusion. *Viruses* **2**, 796–825 (2010).
13. E. E. Heldwein, C. Krummenacher, Entry of herpesviruses into mammalian cells. *Cell. Mol. Life Sci.* **65**, 1653–1668 (2008).
14. A. Abou-Hamdan, L. Belot, A. Albertini, Y. Gaudin, Monomeric Intermediates Formed by Vesiculovirus Glycoprotein during Its Low-pH-induced Structural Transition. *J. Mol. Biol.* **430**, 1685–1695 (2018).
15. H. M. Callaway, D. Zyla, F. Larrous, G. D. de Melo, K. M. Hastie, R. D. Avalos, A. Agarwal, D. Corti, H. Bourhy, E. O. Saphire, Structure of the rabies virus glycoprotein trimer bound to a prefusion-specific neutralizing antibody. *Sci. Adv.* **8**, eabp9151 (2022).
16. W. M. Ng, S. Fedosyuk, S. English, G. Augusto, A. Berg, L. Thorley, R. R. Segireddy, T. A. Bowden, A. D. Douglas, “Structure of trimeric pre-fusion rabies virus glycoprotein in complex with two protective antibodies” (preprint, Microbiology, 2022); https://doi.org/10.1101/2022.02.28.482293.
17. B. Vollmer, V. Pražák, D. Vasishtan, E. E. Jefferys, A. Hernandez-Duran, M. Vallbracht, B. G. Klupp, T. C. Mettenleiter, M. Backovic, F. A. Rey, M. Topf, K. Grünewald, The prefusion structure of herpes simplex virus glycoprotein B. *Sci. Adv.* **6**, eabc1726 (2020).

18. F. Yang, S. Lin, F. Ye, J. Yang, J. Qi, Z. Chen, X. Lin, J. Wang, D. Yue, Y. Cheng, Z. Chen, H. Chen, Y. You, Z. Zhang, Y. Yang, M. Yang, H. Sun, Y. Li, Y. Cao, S. Yang, Y. Wei, G. F. Gao, G. Lu, Structural Analysis of Rabies Virus Glycoprotein Reveals pH-Dependent Conformational Changes and Interactions with a Neutralizing Antibody. *Cell Host Microbe* **27**, 441-453.e7 (2020).
19. Y. Gaudin, R. W. Ruigrok, M. Knossow, A. Flamand, Low-pH conformational changes of rabies virus glycoprotein and their role in membrane fusion. *J. Virol.* **67**, 1365–1372 (1993).
20. Y. Gaudin, H. Raux, A. Flamand, R. W. Ruigrok, Identification of amino acids controlling the low-pH-induced conformational change of rabies virus glycoprotein. *J. Virol.* **70**, 7371–7378 (1996).
21. A. A. Albertini, C. Mérigoux, S. Libersou, K. Madiona, S. Bressanelli, S. Roche, J. Lepault, R. Melki, P. Vachette, Y. Gaudin, Characterization of Monomeric Intermediates during VSV Glycoprotein Structural Transition. *PLOS Pathog.* **8**, e1002556 (2012).
22. Y. Gaudin, C. Tuffereau, D. Segretain, M. Knossow, A. Flamand, Reversible conformational changes and fusion activity of rabies virus glycoprotein. *J. Virol.* **65**, 4853–4859 (1991).
23. I. Kosik, J. W. Yewdell, Influenza Hemagglutinin and Neuraminidase: Yin–Yang Proteins Coevolving to Thwart Immunity. *Viruses* **11**, 346 (2019).
24. B. M. Davis, G. F. Rall, M. J. Schnell, Everything You Always Wanted to Know About Rabies Virus (But Were Afraid to Ask). *Annu. Rev. Virol.* **2**, 451–471 (2015).
25. P. V'kovski, A. Kratzel, S. Steiner, H. Stalder, V. Thiel, Coronavirus biology and replication: implications for SARS-CoV-2. *Nat. Rev. Microbiol.* **19**, 155–170 (2021).
26. H. Ebel, T. Benecke, B. Vollmer, Stabilisation of Viral Membrane Fusion Proteins in Prefusion Conformation by Structure-Based Design for Structure Determination and Vaccine Development. *Viruses* **14**, 1816 (2022).
27. L. R. Baden, H. M. E. Sahly, B. Essink, K. Kotloff, S. Frey, R. Novak, D. Diemert, S. A. Spector, N. Rouphael, C. B. Creech, J. McGettigan, S. Khetan, N. Segall, J. Solis, A. Brosz, C. Fierro, H. Schwartz, K. Neuzil, L. Corey, P. Gilbert, H. Janes, D. Follmann, M. Marovich, J. Mascola, L. Polakowski, J. Ledgerwood, B. S. Graham, H. Bennett, R. Pajon, C. Knightly, B. Leav, W. Deng, H. Zhou, S. Han, M. Ivarsson, J. Miller, T. Zaks, Efficacy and Safety of the mRNA-1273 SARS-CoV-2 Vaccine. *N. Engl. J. Med.* **384**, 403–416 (2021).
28. P. T. Heath, E. P. Galiza, D. N. Baxter, M. Boffito, D. Browne, F. Burns, D. R. Chadwick, R. Clark, C. Cosgrove, J. Galloway, A. L. Goodman, A. Heer, A. Higham, S. Iyengar, A. Jamal, C. Jeanes, P. A. Kalra, C. Kyriakidou, D. F. McAuley, A. Meyrick, A. M. Minassian, J. Minton, P. Moore, I. Munsoor, H. Nicholls, O. Osanlou, J. Packham, C. H. Pretswell, A. S. F. Ramos, D. Saralaya, R. P. Sheridan, R. Smith, R. L. Soiza, P. A. Swift, E. C. Thomson, J. Turner, M. E. Viljoen, G. Albert, I. Cho, F. Dubovsky, G. Glenn, J. Rivers, A. Robertson, K. Smith, S. Toback, Safety and Efficacy of NVX-CoV2373 Covid-19 Vaccine. *N. Engl. J. Med.* **385**, 1172–1183 (2021).
29. F. P. Polack, S. J. Thomas, N. Kitchin, J. Absalon, A. Gurtman, S. Lockhart, J. L. Perez, G. P. Marc, E. D. Moreira, C. Zerbini, R. Bailey, K. A. Swanson, S.

Roychoudhury, K. Koury, P. Li, W. V. Kalina, D. Cooper, R. W. Frenck, L. L. Hammitt, Ö. Türeci, H. Nell, A. Schaefer, S. Ünal, D. B. Tresnan, S. Mather, P. R. Dormitzer, U. Şahin, K. U. Jansen, W. C. Gruber, Safety and Efficacy of the BNT162b2 mRNA Covid-19 Vaccine. *N. Engl. J. Med.* **383**, 2603–2615 (2020).
30. Md. M. Rahman, Md. H. U. Masum, S. Wajed, A. Talukder, A comprehensive review on COVID-19 vaccines: development, effectiveness, adverse effects, distribution and challenges. *VirusDisease* **33**, 1–22 (2022).
31. J. Sadoff, G. Gray, A. Vandebosch, V. Cárdenas, G. Shukarev, B. Grinsztejn, P. A. Goepfert, C. Truyers, H. Fennema, B. Spiessens, K. Offergeld, G. Scheper, K. L. Taylor, M. L. Robb, J. Treanor, D. H. Barouch, J. Stoddard, M. F. Ryser, M. A. Marovich, K. M. Neuzil, L. Corey, N. Cauwenberghs, T. Tanner, K. Hardt, J. Ruiz-Guiñazú, M. L. Gars, H. Schuitemaker, J. V. Hoof, F. Struyf, M. Douoguih, Safety and Efficacy of Single-Dose Ad26.COV2.S Vaccine against Covid-19. *N. Engl. J. Med.* **384**, 2187–2201 (2021).
32. Y. Che, A. V. Gribenko, X. Song, L. D. Handke, K. S. Efferen, K. Tompkins, S. Kodali, L. Nunez, A. K. Prasad, L. M. Phelan, M. Ammirati, X. Yu, J. A. Lees, W. Chen, L. Martinez, V. Roopchand, S. Han, X. Qiu, J. P. DeVincenzo, K. U. Jansen, P. R. Dormitzer, K. A. Swanson, Rational design of a highly immunogenic prefusion-stabilized F glycoprotein antigen for a respiratory syncytial virus vaccine. *Sci. Transl. Med.* **15**, eade6422 (2023).
33. S. F. James, E. B. Chahine, A. J. Sucher, C. Hanna, Shingrix: The New Adjuvanted Recombinant Herpes Zoster Vaccine. *Ann. Pharmacother.* **52**, 673–680 (2018).
34. F. Maltz, B. Fidler, Shingrix: A New Herpes Zoster Vaccine. *Pharm. Ther.* **44**, 406–433 (2019).
35. F. Krammer, The human antibody response to influenza A virus infection and vaccination. *Nat. Rev. Immunol.* **19**, 383–397 (2019).
36. J. R. Frost, S. Shaikh, A. Severini, Exploring the Mumps Virus Glycoproteins: A Review. *Viruses* **14**, 1335 (2022).
37. J. Hammond, H. Leister-Tebbe, A. Gardner, P. Abreu, W. Bao, W. Wisemandle, M. Baniecki, V. M. Hendrick, B. Damle, A. Simón-Campos, R. Pypstra, J. M. Rusnak, Oral Nirmatrelvir for High-Risk, Nonhospitalized Adults with Covid-19. *N. Engl. J. Med.* **386**, 1397–1408 (2022).
38. R. J. Landovitz, H. Scott, S. G. Deeks, Prevention, treatment and cure of HIV infection. *Nat. Rev. Microbiol.* **21**, 657–670 (2023).
39. R. Copin, A. Baum, E. Wloga, K. E. Pascal, S. Giordano, B. O. Fulton, A. Zhou, N. Negron, K. Lanza, N. Chan, A. Coppola, J. Chiu, M. Ni, Y. Wei, G. S. Atwal, A. R. Hernandez, K. Saotome, Y. Zhou, M. C. Franklin, A. T. Hooper, S. McCarthy, S. Hamon, J. D. Hamilton, H. M. Staples, K. Alfson, R. Carrion, S. Ali, T. Norton, S. Somersan-Karakaya, S. Sivapalasingam, G. A. Herman, D. M. Weinreich, L. Lipsich, N. Stahl, A. J. Murphy, G. D. Yancopoulos, C. A. Kyratsous, The monoclonal antibody combination REGEN-COV protects against SARS-CoV-2 mutational escape in preclinical and human studies. *Cell* **184**, 3949-3961.e11 (2021).
40. G. Pantaleo, B. Correia, C. Fenwick, V. S. Joo, L. Perez, Antibodies to combat viral infections: development strategies and progress. *Nat. Rev. Drug Discov.* **21**,

676–696 (2022).
41. J. Hansen, A. Baum, K. E. Pascal, V. Russo, S. Giordano, E. Wloga, B. O. Fulton, Y. Yan, K. Koon, K. Patel, K. M. Chung, A. Hermann, E. Ullman, J. Cruz, A. Rafique, T. Huang, J. Fairhurst, C. Libertiny, M. Malbec, W. Lee, R. Welsh, G. Farr, S. Pennington, D. Deshpande, J. Cheng, A. Watty, P. Bouffard, R. Babb, N. Levenkova, C. Chen, B. Zhang, A. Romero Hernandez, K. Saotome, Y. Zhou, M. Franklin, S. Sivapalasingam, D. C. Lye, S. Weston, J. Logue, R. Haupt, M. Frieman, G. Chen, W. Olson, A. J. Murphy, N. Stahl, G. D. Yancopoulos, C. A. Kyratsous, Studies in humanized mice and convalescent humans yield a SARS-CoV-2 antibody cocktail. *Science* **369**, 1010–1014 (2020).
42. J. H. Lee, D. P. Leaman, A. S. Kim, A. Torrents de la Peña, K. Sliepen, A. Yasmeen, R. Derking, A. Ramos, S. W. de Taeye, G. Ozorowski, F. Klein, D. R. Burton, M. C. Nussenzweig, P. Poignard, J. P. Moore, P. J. Klasse, R. W. Sanders, M. B. Zwick, I. A. Wilson, A. B. Ward, Antibodies to a conformational epitope on gp41 neutralize HIV-1 by destabilizing the Env spike. *Nat. Commun.* **6**, 8167 (2015).
43. T. J. Wohlbold, V. Chromikova, G. S. Tan, P. Meade, F. Amanat, P. Comella, A. Hirsh, F. Krammer, Hemagglutinin Stalk- and Neuraminidase-Specific Monoclonal Antibodies Protect against Lethal H10N8 Influenza Virus Infection in Mice. *J. Virol.* **90**, 851–861 (2015).
44. G. E. Nybakken, T. Oliphant, S. Johnson, S. Burke, M. S. Diamond, D. H. Fremont, Structural basis of West Nile virus neutralization by a therapeutic antibody. *Nature* **437**, 764–769 (2005).
45. B. S. Thompson, B. Moesker, J. M. Smit, J. Wilschut, M. S. Diamond, D. H. Fremont, A Therapeutic Antibody against West Nile Virus Neutralizes Infection by Blocking Fusion within Endosomes. *PLOS Pathog.* **5**, e1000453 (2009).
46. F. Long, R. H. Fong, S. K. Austin, Z. Chen, T. Klose, A. Fokine, Y. Liu, J. Porta, G. Sapparapu, W. Akahata, B. J. Doranz, J. E. Crowe, M. S. Diamond, M. G. Rossmann, Cryo-EM structures elucidate neutralizing mechanisms of anti-chikungunya human monoclonal antibodies with therapeutic activity. *Proc. Natl. Acad. Sci.* **112**, 13898–13903 (2015).
47. V. R. Gómez Román, J. C. Murray, L. M. Weiner, “Chapter 1 - Antibody-Dependent Cellular Cytotoxicity (ADCC)” in *Antibody Fc*, M. E. Ackerman, F. Nimmerjahn, Eds. (Academic Press, Boston, 2014; https://www.sciencedirect.com/science/article/pii/B9780123948021000017), pp. 1–27.
48. J. B. Case, S. Mackin, J. M. Errico, Z. Chong, E. A. Madden, B. Whitener, B. Guarino, M. A. Schmid, K. Rosenthal, K. Ren, H. V. Dang, G. Snell, A. Jung, L. Droit, S. A. Handley, P. J. Halfmann, Y. Kawaoka, J. E. Crowe, D. H. Fremont, H. W. Virgin, Y.-M. Loo, M. T. Esser, L. A. Purcell, D. Corti, M. S. Diamond, Resilience of S309 and AZD7442 monoclonal antibody treatments against infection by SARS-CoV-2 Omicron lineage strains. *Nat. Commun.* **13**, 3824 (2022).
49. J. M. White, A. E. Ward, L. Odongo, L. K. Tamm, Viral Membrane Fusion: A Dance Between Proteins and Lipids. *Annu. Rev. Virol.* **10**, 139–161 (2023).
50. D. J. Benton, A. G. Wrobel, P. Xu, C. Roustan, S. R. Martin, P. B. Rosenthal, J. J.

Skehel, S. J. Gamblin, Receptor binding and priming of the spike protein of SARS-CoV-2 for membrane fusion. *Nature* **588**, 327–330 (2020).
51. M. Lu, P. D. Uchil, W. Li, D. Zheng, D. S. Terry, J. Gorman, W. Shi, B. Zhang, T. Zhou, S. Ding, R. Gasser, J. Prévost, G. Beaudoin-Bussières, S. P. Anand, A. Laumaea, J. R. Grover, L. Liu, D. D. Ho, J. R. Mascola, A. Finzi, P. D. Kwong, S. C. Blanchard, W. Mothes, Real-Time Conformational Dynamics of SARS-CoV-2 Spikes on Virus Particles. *Cell Host Microbe* **28**, 880-891.e8 (2020).
52. C.-L. Hsieh, J. A. Goldsmith, J. M. Schaub, A. M. DiVenere, H.-C. Kuo, K. Javanmardi, K. C. Le, D. Wrapp, A. G. Lee, Y. Liu, C.-W. Chou, P. O. Byrne, C. K. Hjorth, N. V. Johnson, J. Ludes-Meyers, A. W. Nguyen, J. Park, N. Wang, D. Amengor, J. J. Lavinder, G. C. Ippolito, J. A. Maynard, I. J. Finkelstein, J. S. McLellan, Structure-based design of prefusion-stabilized SARS-CoV-2 spikes. *Science* **369**, 1501–1505 (2020).
53. D. Wrapp, N. Wang, K. S. Corbett, J. A. Goldsmith, C.-L. Hsieh, O. Abiona, B. S. Graham, J. S. McLellan, Cryo-EM structure of the 2019-nCoV spike in the prefusion conformation. *Science* **367**, 1260–1263 (2020).
54. H. Qiao, S. L. Pelletier, L. Hoffman, J. Hacker, R. T. Armstrong, J. M. White, Specific Single or Double Proline Substitutions in the “Spring-loaded” Coiled-Coil Region of the Influenza Hemagglutinin Impair or Abolish Membrane Fusion Activity. *J. Cell Biol.* **141**, 1335–1347 (1998).
55. A. Krarup, D. Truan, P. Furmanova-Hollenstein, L. Bogaert, P. Bouchier, I. J. M. Bisschop, M. N. Widjojoatmodjo, R. Zahn, H. Schuitemaker, J. S. McLellan, J. P. M. Langedijk, A highly stable prefusion RSV F vaccine derived from structural analysis of the fusion mechanism. *Nat. Commun.* **6**, 8143 (2015).
56. J. Pallesen, N. Wang, K. S. Corbett, D. Wrapp, R. N. Kirchdoerfer, H. L. Turner, C. A. Cottrell, M. M. Becker, L. Wang, W. Shi, W.-P. Kong, E. L. Andres, A. N. Kettenbach, M. R. Denison, J. D. Chappell, B. S. Graham, A. B. Ward, J. S. McLellan, Immunogenicity and structures of a rationally designed prefusion MERS-CoV spike antigen. *Proc. Natl. Acad. Sci.* **114**, E7348–E7357 (2017).
57. J. E. Bowen, Y.-J. Park, C. Stewart, J. T. Brown, W. K. Sharkey, A. C. Walls, A. Joshi, K. R. Sprouse, M. McCallum, M. A. Tortorici, N. M. Franko, J. K. Logue, I. G. Mazzitelli, A. W. Nguyen, R. P. Silva, Y. Huang, J. S. Low, J. Jerak, S. W. Tiles, K. Ahmed, A. Shariq, J. M. Dan, Z. Zhang, D. Weiskopf, A. Sette, G. Snell, C. M. Posavad, N. T. Iqbal, J. Geffner, A. Bandera, A. Gori, F. Sallusto, J. A. Maynard, S. Crotty, W. C. Van Voorhis, C. Simmerling, R. Grifantini, H. Y. Chu, D. Corti, D. Veesler, SARS-CoV-2 spike conformation determines plasma neutralizing activity elicited by a wide panel of human vaccines. *Sci. Immunol.* **7**, eadf1421 (2022).
58. F. X. Heinz, K. Stiasny, Distinguishing features of current COVID-19 vaccines: knowns and unknowns of antigen presentation and modes of action. *Npj Vaccines* **6**, 1–13 (2021).
59. L. Rutten, M. Swart, A. Koornneef, P. Bouchier, S. Blokland, A. Sadi, J. Juraszek, A. Vijayan, S. Schmit-Tillemans, J. Verspuij, Y. Choi, C. E. Daal, A. Perkasa, S. Torres Morales, S. K. Myeni, M. Kikkert, J. Tolboom, D. van Manen, H. Kuipers, H. Schuitemaker, R. Zahn, J. P. M. Langedijk, Impact of SARS-CoV-2 spike stability and RBD exposure on antigenicity and immunogenicity. *Sci. Rep.* **14**, 5735 (2024).

60. A. Papi, M. G. Ison, J. M. Langley, D.-G. Lee, I. Leroux-Roels, F. Martinon-Torres, T. F. Schwarz, R. N. van Zyl-Smit, L. Campora, N. Dezutter, N. de Schrevel, L. Fissette, M.-P. David, M. V. der Wielen, L. Kostanyan, V. Hulstrøm, Respiratory Syncytial Virus Prefusion F Protein Vaccine in Older Adults. *N. Engl. J. Med.* **388**, 595–608 (2023).
61. E. A. Hodge, G. S. Naika, S. M. Kephart, A. Nguyen, R. Zhu, M. A. Benhaim, W. Guo, J. P. Moore, S.-L. Hu, R. W. Sanders, K. K. Lee, Structural dynamics reveal isolate-specific differences at neutralization epitopes on HIV Env. *iScience* **25**, 104449 (2022).
62. D. S. Chorev, C. V. Robinson, The importance of the membrane for biophysical measurements. *Nat. Chem. Biol.* **16**, 1285–1292 (2020).
63. J. Thoma, B. M. Burmann, Fake It 'Till You Make It—The Pursuit of Suitable Membrane Mimetics for Membrane Protein Biophysics. *Int. J. Mol. Sci.* **22**, 50 (2021).
64. J. K. Hu, J. C. Crampton, A. Cupo, T. Ketas, M. J. van Gils, K. Sliepen, S. W. de Taeye, D. Sok, G. Ozorowski, I. Deresa, R. Stanfield, A. B. Ward, D. R. Burton, P. J. Klasse, R. W. Sanders, J. P. Moore, S. Crotty, Murine Antibody Responses to Cleaved Soluble HIV-1 Envelope Trimers Are Highly Restricted in Specificity. *J. Virol.* **89**, 10383–10398 (2015).
65. A. Stano, D. P. Leaman, A. S. Kim, L. Zhang, L. Autin, J. Ingale, S. K. Gift, J. Truong, R. T. Wyatt, A. J. Olson, M. B. Zwick, Dense Array of Spikes on HIV-1 Virion Particles. *J. Virol.* **91**, e00415-17 (2017).
66. Y. Watanabe, J. D. Allen, D. Wrapp, J. S. McLellan, M. Crispin, Site-specific glycan analysis of the SARS-CoV-2 spike. *Science* **369**, 330–333 (2020).
67. L. Casalino, Z. Gaieb, J. A. Goldsmith, C. K. Hjorth, A. C. Dommer, A. M. Harbison, C. A. Fogarty, E. P. Barros, B. C. Taylor, J. S. McLellan, E. Fadda, R. E. Amaro, Beyond Shielding: The Roles of Glycans in the SARS-CoV-2 Spike Protein. *ACS Cent. Sci.* **6**, 1722–1734 (2020).
68. F. Beilstein, A. Abou Hamdan, H. Raux, L. Belot, M. Ouldali, A. A. Albertini, Y. Gaudin, Identification of a pH-Sensitive Switch in VSV-G and a Crystal Structure of the G Pre-fusion State Highlight the VSV-G Structural Transition Pathway. *Cell Rep.* **32**, 108042 (2020).
69. S. Roche, S. Bressanelli, F. A. Rey, Y. Gaudin, Crystal structure of the low-pH form of the vesicular stomatitis virus glycoprotein G. *Science* **313**, 187–191 (2006).
70. S. Roche, F. A. Rey, Y. Gaudin, S. Bressanelli, Structure of the Prefusion Form of the Vesicular Stomatitis Virus Glycoprotein G. *Science* **315**, 843–848 (2007).
71. D. C. Wiley, J. J. Skehel, Crystallization and X-ray diffraction studies on the haemagglutinin glycoprotein from the membrane of influenza virus. *J. Mol. Biol.* **112**, 343–347 (1977).
72. M. Yuan, N. C. Wu, X. Zhu, C.-C. D. Lee, R. T. Y. So, H. Lv, C. K. P. Mok, I. A. Wilson, A highly conserved cryptic epitope in the receptor binding domains of SARS-CoV-2 and SARS-CoV. *Science* **368**, 630–633 (2020).
73. M. S. A. Gilman, P. Furmanova-Hollenstein, G. Pascual, A. B. van 't Wout, J. P. M. Langedijk, J. S. McLellan, Transient opening of trimeric prefusion RSV F proteins. *Nat. Commun.* **10**, 1–13 (2019).

74. L. J. Calder, T. Calcraft, S. Hussain, R. Harvey, P. B. Rosenthal, Electron cryotomography of SARS-CoV-2 virions reveals cylinder-shaped particles with a double layer RNP assembly. *Commun. Biol.* **5**, 1–6 (2022).
75. Q. J. Huang, K. Song, C. Xu, D. N. A. Bolon, J. P. Wang, R. W. Finberg, C. A. Schiffer, M. Somasundaran, Quantitative structural analysis of influenza virus by cryo-electron tomography and convolutional neural networks. *Structure* **30**, 777-786.e3 (2022).
76. Z. Ke, J. Oton, K. Qu, M. Cortese, V. Zila, L. McKeane, T. Nakane, J. Zivanov, C. J. Neufeldt, B. Cerikan, J. M. Lu, J. Peukes, X. Xiong, H.-G. Kräusslich, S. H. W. Scheres, R. Bartenschlager, J. A. G. Briggs, Structures and distributions of SARS-CoV-2 spike proteins on intact virions. *Nature* **588**, 498–502 (2020).
77. S. Klein, M. Cortese, S. L. Winter, M. Wachsmuth-Melm, C. J. Neufeldt, B. Cerikan, M. L. Stanifer, S. Boulant, R. Bartenschlager, P. Chlanda, SARS-CoV-2 structure and replication characterized by in situ cryo-electron tomography. *Nat. Commun.* **11**, 5885 (2020).
78. K. Zhou, Z. Si, P. Ge, J. Tsao, M. Luo, Z. H. Zhou, Atomic model of vesicular stomatitis virus and mechanism of assembly. *Nat. Commun.* **13**, 5980 (2022).
79. C. Dacon, C. Tucker, L. Peng, C.-C. D. Lee, T.-H. Lin, M. Yuan, Y. Cong, L. Wang, L. Purser, J. K. Williams, C.-W. Pyo, I. Kosik, Z. Hu, M. Zhao, D. Mohan, A. J. R. Cooper, M. Peterson, J. Skinner, S. Dixit, E. Kollins, L. Huzella, D. Perry, R. Byrum, S. Lembirik, D. Drawbaugh, B. Eaton, Y. Zhang, E. S. Yang, M. Chen, K. Leung, R. S. Weinberg, A. Pegu, D. E. Geraghty, E. Davidson, I. Douagi, S. Moir, J. W. Yewdell, C. Schmaljohn, P. D. Crompton, M. R. Holbrook, D. Nemazee, J. R. Mascola, I. A. Wilson, J. Tan, Broadly neutralizing antibodies target the coronavirus fusion peptide. *Science* **377**, 728–735 (2022).
80. R. Henderson, R. J. Edwards, K. Mansouri, K. Janowska, V. Stalls, S. M. C. Gobeil, M. Kopp, D. Li, R. Parks, A. L. Hsu, M. J. Borgnia, B. F. Haynes, P. Acharya, Controlling the SARS-CoV-2 spike glycoprotein conformation. *Nat. Struct. Mol. Biol.* **27**, 925–933 (2020).
81. T. Zhou, Y. Tsybovsky, J. Gorman, M. Rapp, G. Cerutti, G.-Y. Chuang, P. S. Katsamba, J. M. Sampson, A. Schön, J. Bimela, J. C. Boyington, A. Nazzari, A. S. Olia, W. Shi, M. Sastry, T. Stephens, J. Stuckey, I.-T. Teng, P. Wang, S. Wang, B. Zhang, R. A. Friesner, D. D. Ho, J. R. Mascola, L. Shapiro, P. D. Kwong, Cryo-EM Structures of SARS-CoV-2 Spike without and with ACE2 Reveal a pH-Dependent Switch to Mediate Endosomal Positioning of Receptor-Binding Domains. *Cell Host Microbe* **28**, 867-879.e5 (2020).
82. M. Wu, G. C. Lander, How low can we go? Structure determination of small biological complexes using single-particle cryo-EM. *Curr. Opin. Struct. Biol.* **64**, 9–16 (2020).
83. Y. Z. Tan, P. R. Baldwin, J. H. Davis, J. R. Williamson, C. S. Potter, B. Carragher, D. Lyumkis, Addressing preferred specimen orientation in single-particle cryo-EM through tilting. *Nat. Methods* **14**, 793–796 (2017).
84. M. A. G. Hoffmann, Z. Yang, K. E. Huey-Tubman, A. A. Cohen, P. N. P. Gnanapragasam, L. M. Nakatomi, K. N. Storm, W. J. Moon, P. J. C. Lin, P. J. Bjorkman, ESCRT recruitment to mRNA-encoded SARS-CoV-2 spike induces virus-like particles and enhanced antibody responses. bioRxiv [Preprint] (2022).

https://doi.org/10.1101/2022.12.26.521940.
85. R. J. Edwards, K. Mansouri, V. Stalls, K. Manne, B. Watts, R. Parks, K. Janowska, S. M. C. Gobeil, M. Kopp, D. Li, X. Lu, Z. Mu, M. Deyton, T. H. Oguin, J. Sprenz, W. Williams, K. O. Saunders, D. Montefiori, G. D. Sempowski, R. Henderson, S. Munir Alam, B. F. Haynes, P. Acharya, Cold sensitivity of the SARS-CoV-2 spike ectodomain. *Nat. Struct. Mol. Biol.*, 1–4 (2021).
86. Y. Gaudin, Folding of rabies virus glycoprotein: epitope acquisition and interaction with endoplasmic reticulum chaperones. *J. Virol.* **71**, 3742–3750 (1997).
87. S. M.-C. Gobeil, K. Janowska, S. McDowell, K. Mansouri, R. Parks, K. Manne, V. Stalls, M. F. Kopp, R. Henderson, R. J. Edwards, B. F. Haynes, P. Acharya, D614G Mutation Alters SARS-CoV-2 Spike Conformation and Enhances Protease Cleavage at the S1/S2 Junction. *Cell Rep.* **34**, 108630 (2021).
88. P. V. Raghuvamsi, N. K. Tulsian, F. Samsudin, X. Qian, K. Purushotorman, G. Yue, M. M. Kozma, W. Y. Hwa, J. Lescar, P. J. Bond, P. A. MacAry, G. S. Anand, SARS-CoV-2 S protein:ACE2 interaction reveals novel allosteric targets. *eLife* **10**, e63646 (2021).
89. A. Hvidt, K. Linderstrøm-Lang, Exchange of hydrogen atoms in insulin with deuterium atoms in aqueous solutions. *Biochim. Biophys. Acta* **14**, 574–575 (1954).
90. Y. Bai, J. S. Milne, L. Mayne, S. W. Englander, Primary structure effects on peptide group hydrogen exchange. *Proteins Struct. Funct. Bioinforma.* **17**, 75–86 (1993).
91. A. Hvidt, G. Johansen, K. Linderstrøm-lang, “DEUTERIUM AND 18O EXCHANGE” in *The Composition, Structure and Reactivity of Proteins*, P. Alexander, R. J. Block, Eds. (Pergamon, 1960; https://www.sciencedirect.com/science/article/pii/B9780080094250500108), pp. 101–130.
92. Z.-Y. Kan, B. T. Walters, L. Mayne, S. W. Englander, Protein hydrogen exchange at residue resolution by proteolytic fragmentation mass spectrometry analysis. *Proc. Natl. Acad. Sci.* **110**, 16438–16443 (2013).
93. C. Lu, M. L. Wells, A. Reckers, A. Glasgow, Site-resolved energetic information from HX/MS experiments. bioRxiv [Preprint] (2024). https://doi.org/10.1101/2024.08.04.606547.

Chapter 2:

The SARS-CoV-2 Spike Protein Samples an Open-Trimer Conformation that Exposes Novel Epitopes

---

The work presented in this chapter is adapted from: S. M. Costello*, S. R. Shoemaker*, H. T. Hobbs, A. W. Nguyen, C.-L. Hsieh, J. A. Maynard, J. S. McLellan, J. E. Pak, S. Marqusee, The SARS-CoV-2 spike reversibly samples an open-trimer conformation exposing novel epitopes. *Nat. Struct. Mol. Biol.* **29**, 229–238 (2022).

2.1 Introduction

The spike protein from SARS-CoV-2 (also referred to as the S-protein) is the primary target for current vaccines against COVID-19 and the focus of many therapeutic efforts (1–4). This large heavily glycosylated trimeric protein is responsible for cell entry via recognition of the host receptor angiotensin-converting enzyme 2 (ACE2) and membrane fusion (5–7). It is also the principal antigenic determinant of neutralizing antibodies (8). Shortly after release of the viral genome sequence, a version of the spike ectodomain (termed S-2P) was designed to stabilize the prefusion conformation, and the structure was determined by cryo-electron microscopy (cryo-EM) (9, 10).

This S-2P ectodomain comprises the first ~1200 residues of the spike protein (Fig. 1A) with two proline substitutions in the S2 domain designed to stabilize the prefusion conformation, mutations that abolish the furin-cleavage site, and the addition of a C-terminal trimerization motif (9). This mimic, its structure, and others that followed, have been widely used for vaccine development and interpretation of many structure/function and epidemiological studies. To date there are more than 250 structures of SARS-CoV-2 spike ectodomains in the Protein Data Bank (11).

These structural studies together with other functional studies demonstrate that, like all class 1 viral fusion proteins, the spike protein is dynamic, sampling several different conformations during its functional lifecycle (12, 13). The three individual receptor-binding domains (RBDs) sample an ‘up’ state and a ‘down’ state; the up state exposes the ACE2-binding motif and therefore is required for infectivity (7, 10, 14, 15). After receptor binding and cleavage between the S1 and S2 domains, the protein undergoes a major refolding event to allow fusion and adopts the stable post-fusion conformation (6, 7, 16–18).

Despite the wealth of structural information, there are very few experimental studies on the dynamics within the prefusion state. The noted RBD up/down conformational transition has been monitored on the membrane via single molecule FRET and occurs on the order of seconds (19). Large computational resources have been devoted to molecular simulations of the spike protein revealing a dynamic pre-fusion state with a

range of accessible conformations including the potential of a further opening of the RBD and N-terminal domain (NTD) away from the trimer interface (20, 21). Experimentally, the conformational landscape of spike has not been well interrogated and the effects of perturbations, such as ligand binding (both receptor and antibodies) or amino acid substitutions found in emerging variants of concern are unknown.

For these reasons, we turned to hydrogen deuterium exchange monitored by mass spectrometry (HDX-MS) to probe the conformational landscape of the soluble spike prefusion ectodomain as well as the effects of ligand binding and sequence variation. We uncovered a stable alternative conformation that interconverts slowly with the canonical prefusion structure. This conformation is an open trimer, with easily accessible RBDs. It exposes the S2 trimer interface, providing new epitopes in a highly conserved region of the protein.

2.2 Results

2.2.1: Continuous exchange HDX-MS on Spike 2P (S-2P)

HDX-MS offers an ideal complement to the ever-growing number of structural studies on the SARS-CoV-2 spike protein, providing information on its conformational ensemble and dynamics. HDX-MS monitors the time course of exchange of amide hydrogens on

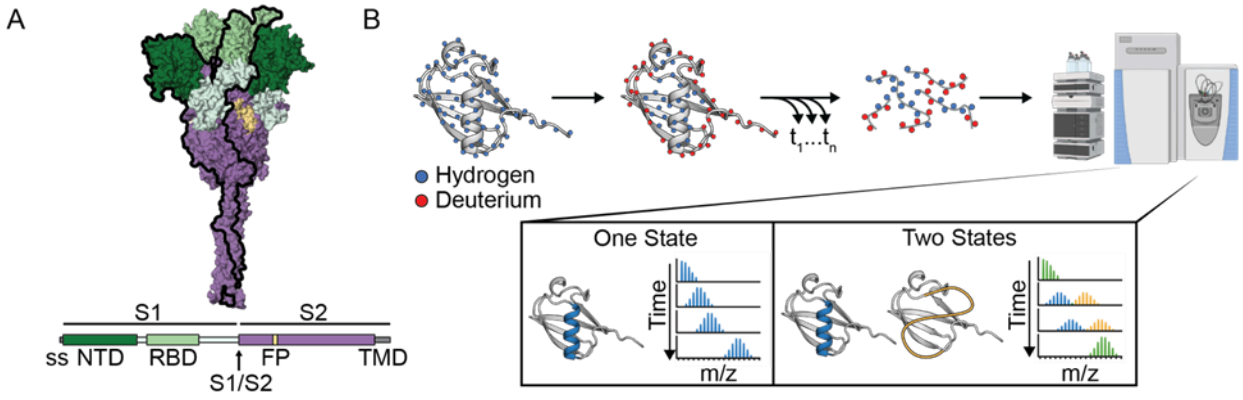

Figure 1. SARS-CoV-2 spike ectodomain and Hydrogen-Deuterium Exchange monitored by mass spectrometry (HDX-MS) experimental overview. (A) Schematic of the prefusion-stabilized SARS-CoV-2 spike protein and a model of the trimeric prefusion conformation (24). **(B)** Schematic of HDX-MS experiment and the resulting mass distributions for a peptide that exists in either one (left) or two (right) separable conformations. In order for the two conformations to result in a bimodal mass distribution, they must not interconvert during the timescale of the HDX experiment (hours). Rapid interconversion would result in a single mass distribution with the ensemble averaged mass profile.

the peptide backbone with the hydrogens in the solvent (see Fig. 1B for description). An individual amide's ability to undergo exchange is directly related to its structure and stability (22, 23).

We first followed the continuous exchange time course of hydrogen exchange at

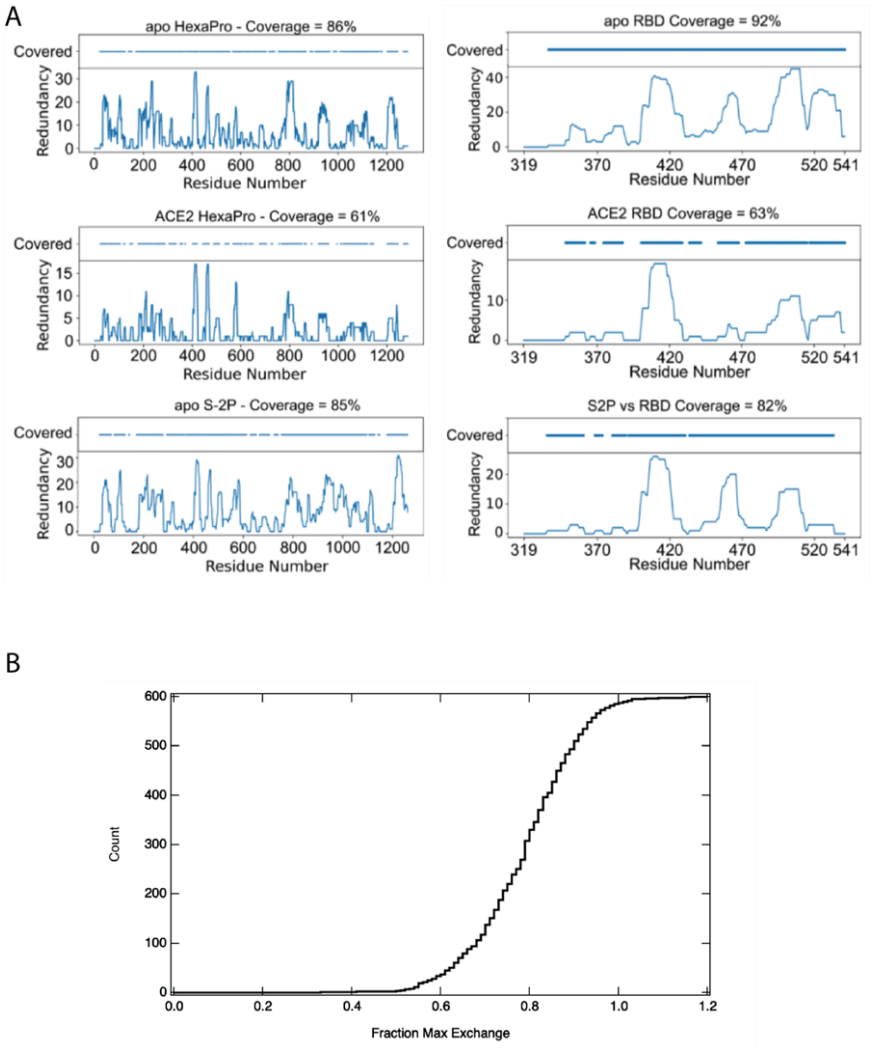

Figure 2. Coverage, redundancy, and back exchange results from HDX-MS experiments
(A) Peptide coverage and redundancy at each residue for all HDX-MS experiments. **(B)** Back-Exchange Control: Cumulative histogram of the fractional deuterium maintained during workup of a fully deuterated sample. Fraction max exchange is corrected for the 90% D2O experimental conditions.

25 °C on the entire S-2P ectodomain, over a period of 15 seconds to 4 hours (see Materials and Methods). Using a combination of porcine pepsin and aspergillopepsin digestion, we obtained 85% peptide coverage allowing us to interrogate the dynamics of the entire protein (800 peptides, which include 9 of the 22 glycosylation sites, average

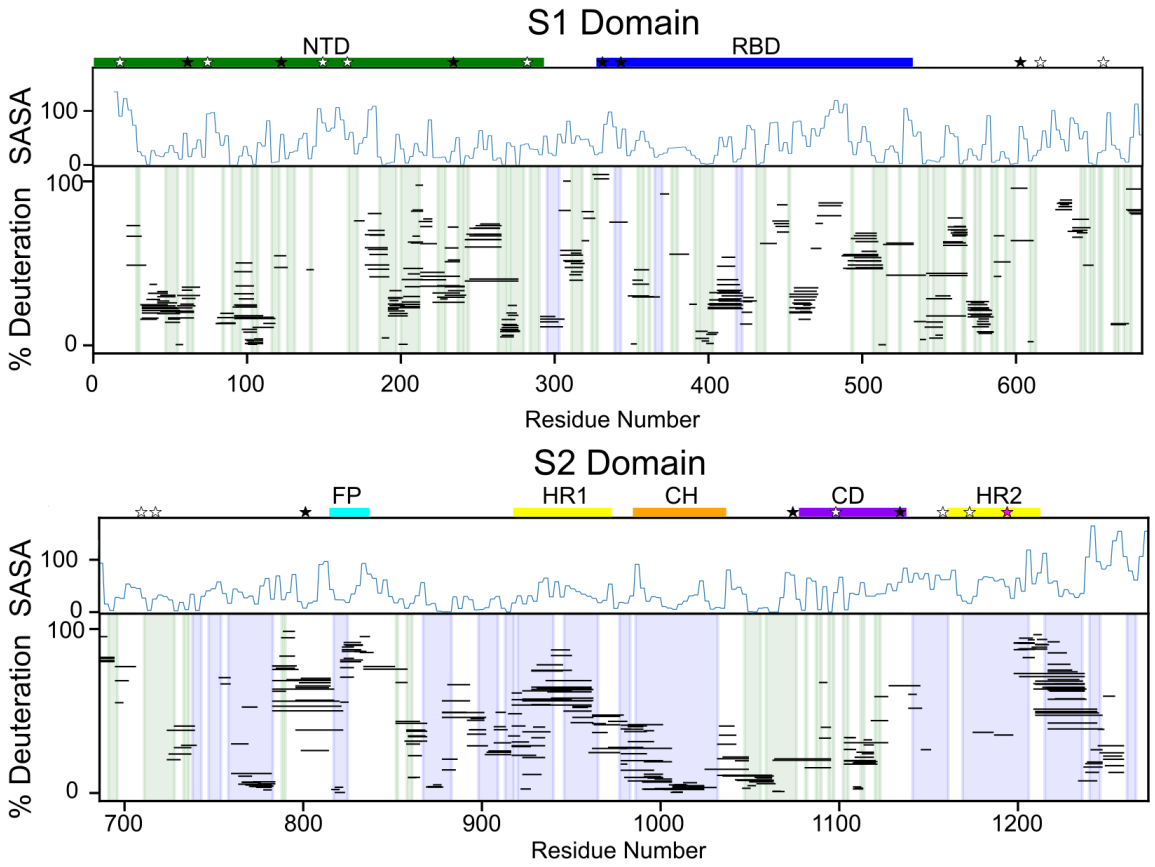

Figure 3. Peptide-level HDX is consistent with the known prefusion conformation. Percent deuteration after one minute of deuterium labeling for every peptide in the S-2P continuous exchange dataset for the S1 (top) and S2 (bottom) domains. Each line represents an individual peptide spanning the residues indicated on the x-axis, with percent deuteration after one minute of exchange indicated on the y-axis (for bimodal peptides, only the less-exchanged centroid shown). Secondary structures in the prefusion conformation are shaded in blue (alpha helices) and green (beta strands). A measure of solvent accessibility is shown above in $Å^2$ (calculated as a three-residue sliding average using the default get_area function in pymol) using a model of the full-length prefusion trimer with all three RBDs in a down position (24). These data are consistent with the SARS-CoV-2 spike trimer secondary structures, notably regions buried in the trimer interface, such as the central helix, show increased protection relative to more exposed regions lacking secondary structure. Important sequence features are indicated above the plot including the N-terminal domain (NTD - green), receptor binding domain (RBD - blue), fusion peptide (FP - cyan), heptad repeat 1 (HR1 - yellow), central helix (CH - orange), core domain (CD - purple) and heptad repeat 2 (HR2 - yellow). Locations of glycans are noted with stars with three categories - glycans detected in at least one peptide of our data set (black, 9/22), glycans known to be on the spike protein where we lack coverage (white, 12/22), and glycans known to be on the spike protein but for which non-glycosylated peptides are observed (pink, 1/22).

redundancy of 8.6) (Fig 3A). Notably, we have coverage in areas not resolved in the cryo-EM structure, including loops in the N-terminal domain (NTD) and RBD that have been found to be recognized by antibodies, loops in the S2 region that include the protease cleavage sites, and C-terminal residues after residue 1145 which includes the second heptad repeat (HR2). Based on control experiments using deuterated protein, our HDX protocol results in an average back exchange of 22% (Fig. 2B). The vast majority of peptides show a classic single isotopic envelope whose centroid increases

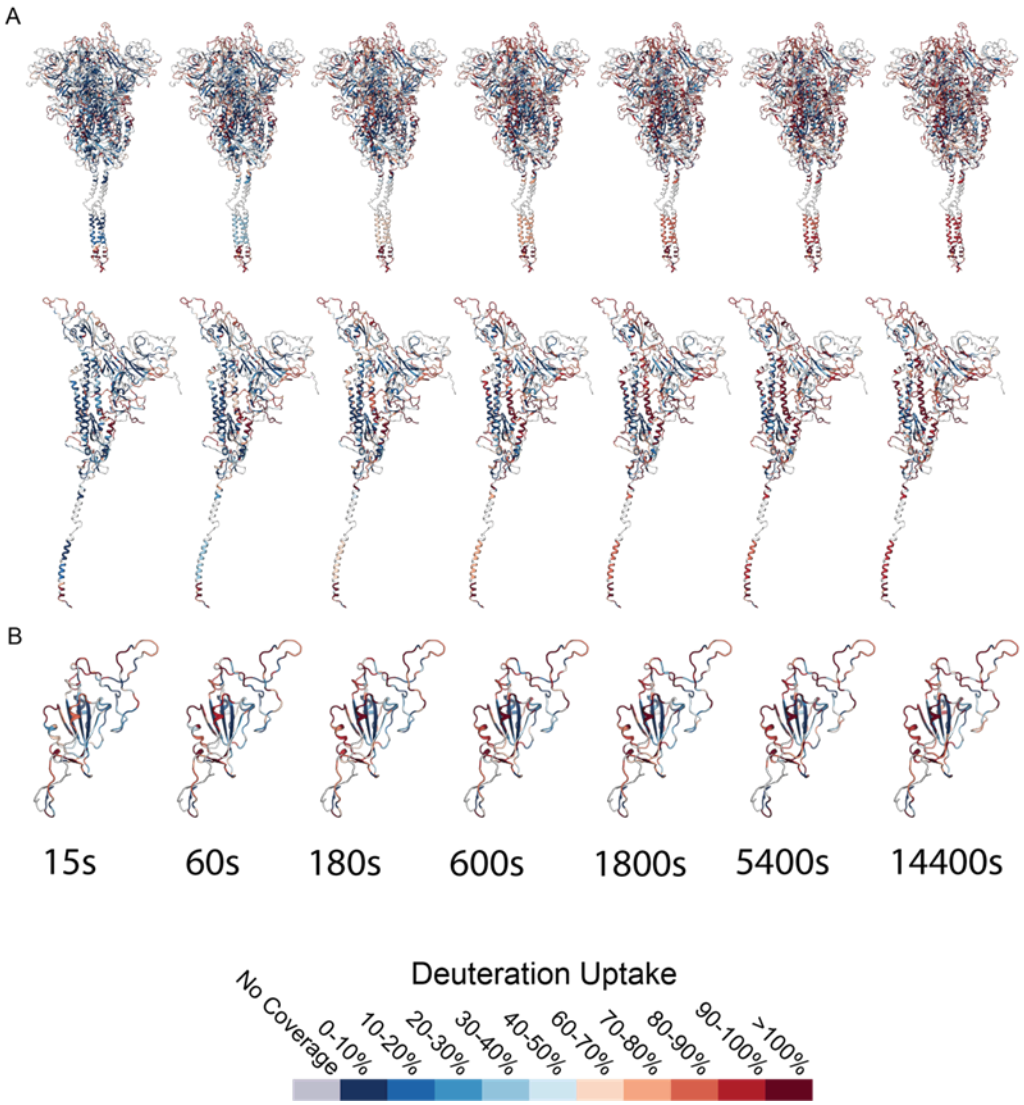

Figure 4. Spike HDX-MS results as a function of time
(A) Deuterium uptake for each S-2P experimental time point mapped to the structure of the prefusion trimer and a single protomer (model from (24)) Per residue deuteration calculated from all peptide data by HDExaminer 3. (B) Deuterium uptake for each Apo-RBD experimental time point mapped to the structure of the RBD (single RBD from a full-length spike trimer model from (24))

in mass as deuterons are added over time (Fig. 1B). A small minority of the peptides,

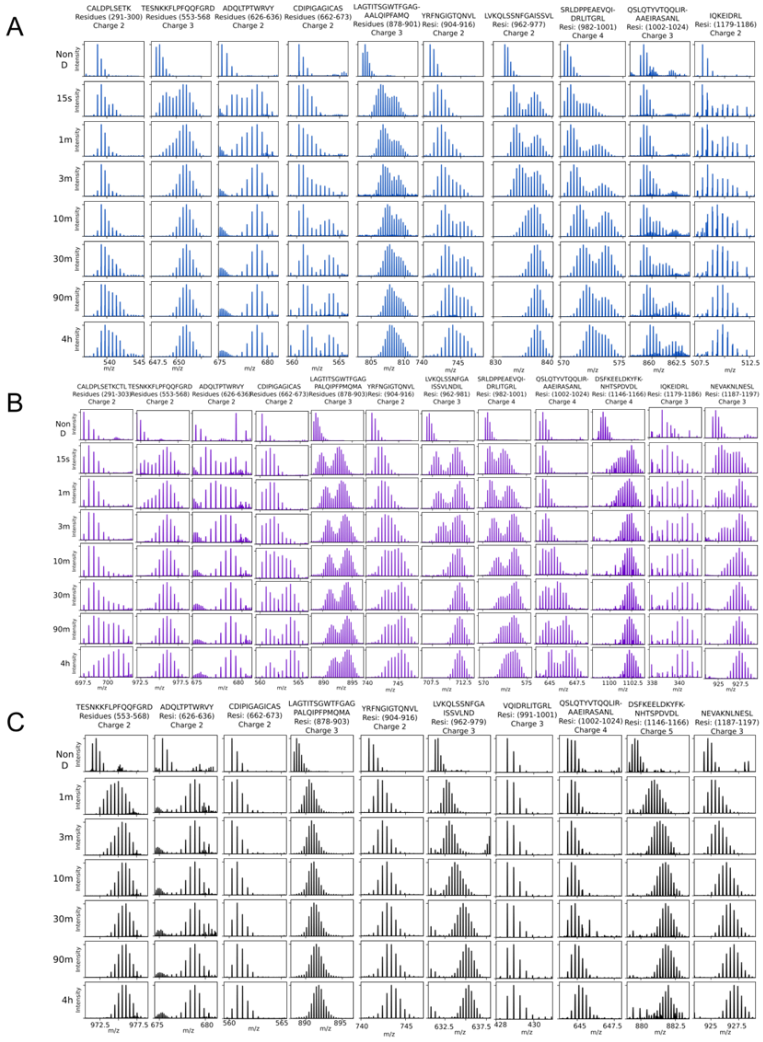

Figure 5. Bimodal peptide spectra observed in continuous labeling HDX-MS experiments
All peptides with observed bimodal behavior for **(A)** S-2P and **(B)** HexaPro **(C)** HexaPro Disulfide Locked

however, show bimodal behavior—with two isotopic envelopes both increasing in mass over time: one less-exchanged distribution and a second more-exchanged distribution (these peptides are described in detail below). The HDX profile of all the peptides, with the exception of the more-exchanged distributions in the bimodal peptides, is consistent with the known prefusion conformation (Fig 3, Fig. 4): secondary structure and buried elements within the trimer exchange slower than exposed loops. We also observe protection for residues 1140¬–1197, which includes HR2, a region not defined in single-particle cryo-EM structures, supporting the predicted helical structure of this

region (24) and the relative rigidity of the stalk observed by cryo-electron tomography (cryo-ET) (25).

2.2.2 Identification of an alternative conformation

Bimodal mass envelopes can indicate the presence of two different conformations that interconvert slowly on the timescale of our hydrogen exchange experiment: one where the amides are more accessible to exchange compared to the other. However, it can also be a result of the kinetics of the hydrogen exchange process itself, so-called EX1 exchange (when the rates of hydrogen bond closing are much slower than the intrinsic chemistry of the exchange process). In this rare scenario, the heavier mass distribution will increase in intensity at the expense of the lighter one over the observed time period. This is not what we observe for the spike protein: the bimodal mass distributions retain their relative intensities, increasing in average mass over time (Fig. 5). The observed ratio is the same for every bimodal peptide under any given condition. The fact that every peptide shows the same ratio indicates that these bimodal peptides reflect two conformations; they report on the regions of the protein that show differences in hydrogen exchange in each conformation.

The bimodal peptides we observe are predominantly in the most conserved region of the protein—the S2 region (26) (Fig. 6A). When mapped onto the canonical prefusion conformation, many come from the helices at the trimer interface (residues 962–1024, 1146–1166, 1187–1196), indicating a second conformation with less stable hydrogen bonding for these helices, consistent with a loss of interprotomer contacts and increased solvent accessibility. We also observe bimodal peptides in other areas of the inter-protomer interface, such as residues 870–916 in S2 and residues 553–574 and 662–673 in S1, again suggesting a change in trimer contacts. Finally, we see bimodal peptides in two regions that do not form interprotomer contacts (residues 291–305, 626–636); instead, these residues form the interface between the NTD and second S1 subdomain (SD2), suggesting that this subdomain interface is also structurally different in this second conformation. All the other peptides (the majority) fit to a classic unimodal distribution in the mass spectrum. The fact that the majority of the peptides are unimodal and that they behave the same in both conformations, indicate that they exist in similar structures in each conformation and suggest that the individual domains have the same structure in each conformation. Previous HDX studies involving the spike protein did not note this behavior, which can be attributed to differences in the experimental conditions and protocols. (27, 28).

2.2.3 Interconversion between the two conformations

These data suggest a model where the spike protein populates two conformations within the prefusion state—the classical prefusion structure seen in cryo-EM (herein referred to as state A)—and one where each domain has a similar

protomer topology and a more flexible or exposed open-trimer interface (herein referred to as state B). The above data do not, however, provide evidence that these states interconvert; any potential interconversion must be slower than the four-hour hydrogen-exchange experiment. Since the transition of the RBD between the up and down conformation occurs on the order of seconds, this conformational heterogeneity is not the source of the bimodal distributions and the observed hydrogen exchange reports on the weighted average of the two RBD conformations. There are several irreversible situations that could account for conformational heterogeneity such as differences in glycosylation, proteolytic degradation, irreversible misfolding, or aggregation. To rule these out, we tested whether the two conformations interconvert reversibly. We used bimodal peptides to quantify the population of each conformation under differing conditions (such as temperature, time, ligand, etc.). Under each condition, we carried out a one-minute pulse of hydrogen exchange (25 °C) and integrated the area under the two mass envelopes for a single bimodal peptide to ascertain the fraction of each conformation under that condition or moment in time (see Materials and Methods).

We monitored two bimodal peptides, one from region 878-903 and one from region 978-1001. Using these two peptides, we quantified the population of each conformation under different conditions (29), such as temperature, time, and ligand. We chose these bimodal peptides because of their high signal to noise ratio and because they report on two distinct regions, thus providing information from both the top and bottom of the S2 interface. We selected a pulse length of one-minute as it provides clearly separable bimodal distributions for these two peptides. For every condition tested, irrespective of the A:B ratio, both peptides report the same fractional population for the two conformations, indicating that all these data can be best described as a variable mixture of just two conformations: the canonical prefusion conformation and an unexpected alternative conformation. Long-term incubation (four days, 25 °C, pH 7.4) demonstrated a slow shift in population from a majority in the canonical prefusion state (state A) to a majority in the alternative conformation (state B) (Fig. 6B, Fig. 7A). Thus, the prefusion state can transform into the alternative state and the bimodal behavior cannot be due to sample heterogeneity such as differential glycosylation. This observed A B conversion, however, does not rule out an irreversible process such as degradation or misfolding.

Postulating that the bimodal peaks represent a reversible structural transition, we used temperature to perturb the system and investigate the ability to interconvert. Indeed, the conformations do interconvert reversibly, with a preference for B at 4 °C and A at 37 °C (Fig. 6B). The observed kinetics of interconversion are extremely slow: A B $t_{1/2}$ of ~17 hours at 4 °C and, when that same sample is moved to ~37 °C, B A $t_{1/2}$ of ~ 9 hours (Fig. 6C, Table 1). Notably the final, and presumably equilibrium, distribution at either temperature shows an observable population of both states (>5%), indicating an

energy difference of less than 2 kcal/mol between the two conformations under both conditions.

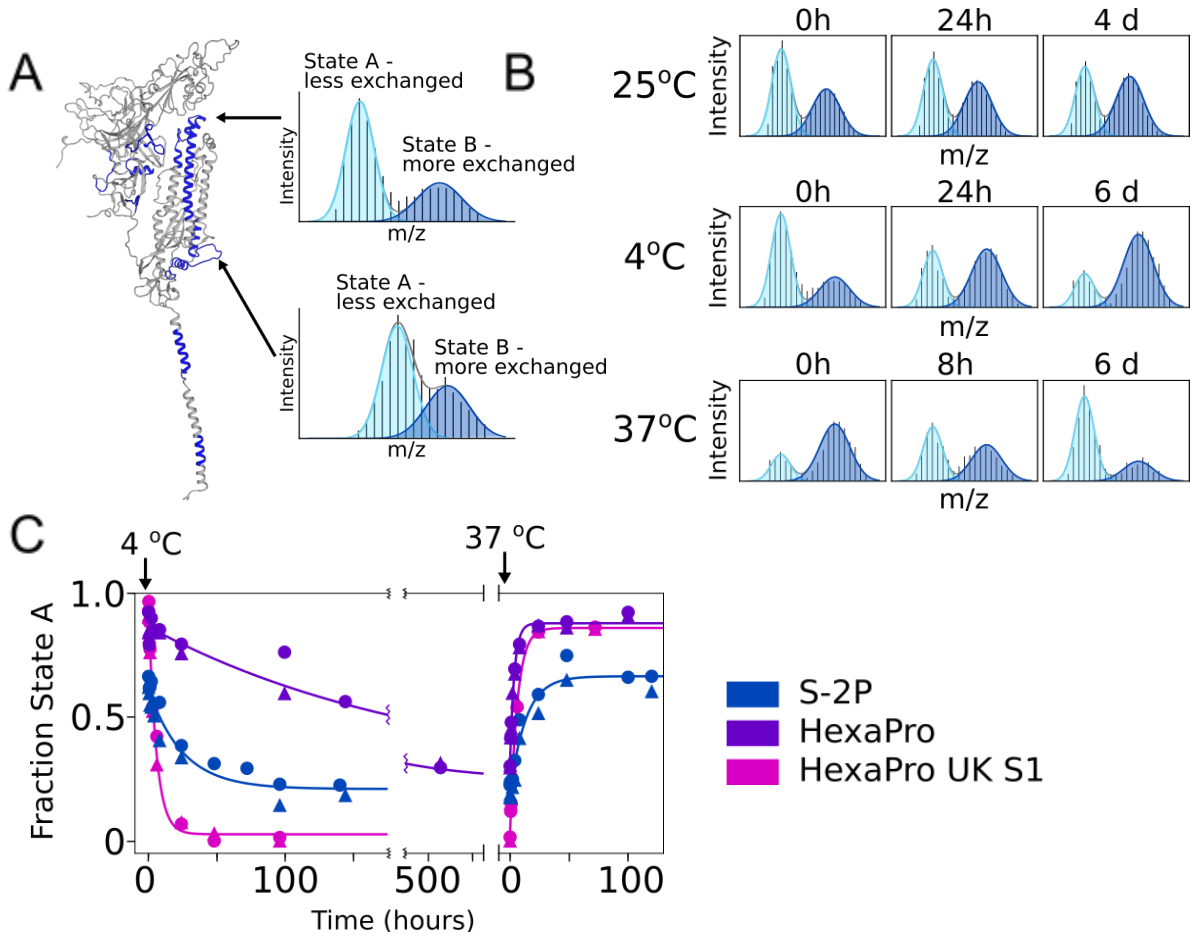

Figure 6. The Spike ectodomain reversibly samples two conformations. (A) Left: SARS-CoV-2 spike monomer with all regions that have peptides showing bimodal mass distributions colored in blue. Right: Example mass spectra from two peptides after one minute of deuteration (top: residues 982–1001, bottom: residues 878–903) with overlaid fitted gaussian distributions that describe each protein conformation in blue (light blue: less exchanged A state, dark blue: the more exchanged B state). **(B)** Conformational preference for the S-2P spike construct at 25 °C, 4 °C and 37 °C monitored by pulsed-labeling. At 25 °C S-2P converts from primarily state A to ~50:50 A:B after 4 days. At 4 °C, S-2P prefers state B while at 37 °C, S-2P prefers state A. **(C)** The kinetics of interconversion between the A and B states for different spike variants. Starting from an initial prefusion conformation (state A, 37 °C), samples were rapidly transferred to 4 °C and assayed for conversion to state B over time using pulsed-labeling HDX-MS. To estimate fraction state A, peptides from two different regions (residues 982-1001 (circles) and residues 878-903 (triangles)) were fit to two gaussians. Data from both regions were used to determine the rate of interconversion.

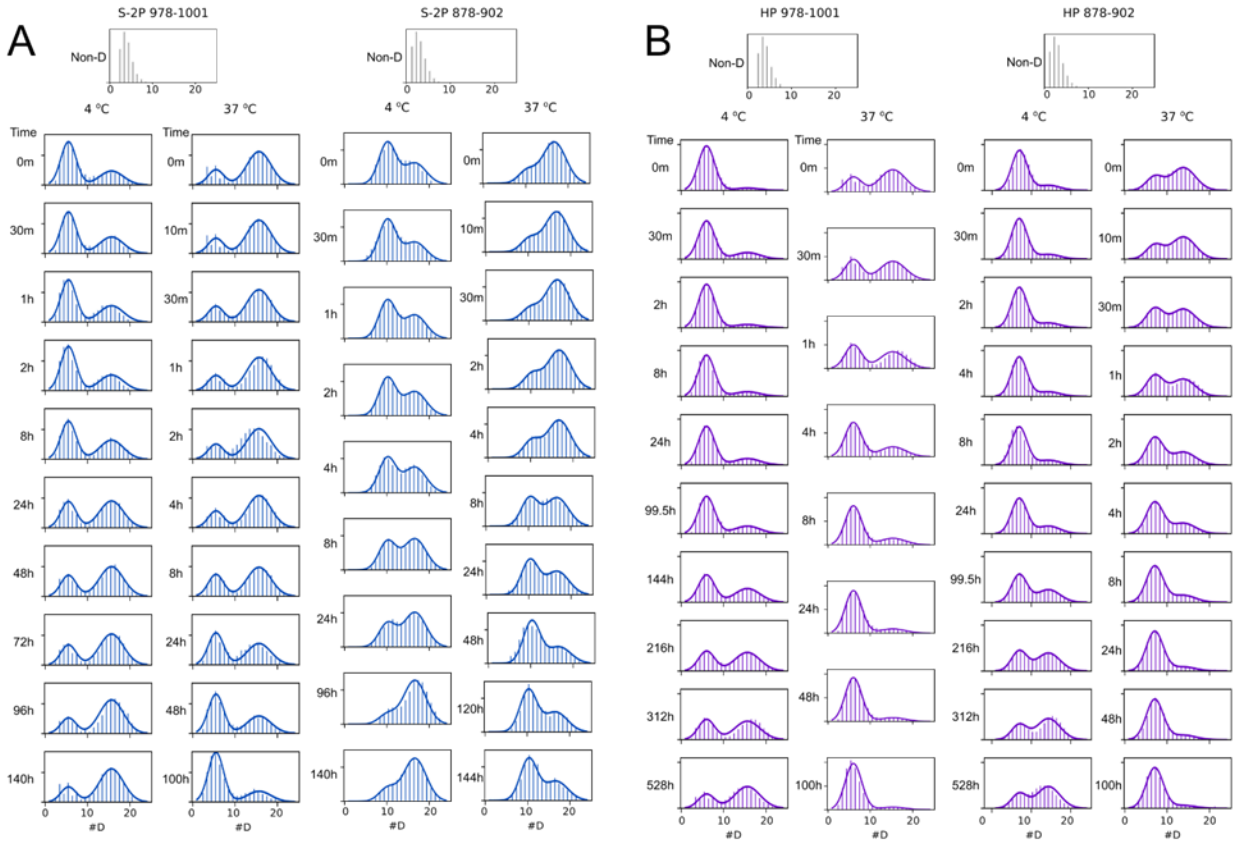

Figure 7. Example bimodal peptide spectra observed in pulse-labeling HDX-MS experiments One example time course for a peptide from each region used to quantify states A and B. The bimodals in the timecourse were globally fit to determine the distributions for state A and state B, the fits were then used to quantify the relative populations of state A and state B, the resulting gaussian fits are overlaid. Undeuterated spectra are at the top in gray.

The prefusion conformation of spike has already been noted to be temperature dependent. Cryo-EM experiments of spike incubated at 4 °C for 5 to 7 days showed less than 10% of the definable prefusion spike particles seen on grids of freshly prepared spike. Incubating spike at 37 °C for three hours after storage at 4 °C recovered particle density to the level seen using freshly prepared protein (30). Failure to detect particles also correlated with a loss in recognition by an antibody known to recognize quaternary structure. These studies are consistent with our findings—long-term incubation of spike at 37 °C biases to the prefusion conformation while long-term incubation at 4 °C prefers an expanded conformation, which is apparently not well visualized on cryo-EM grids. Our results suggest that, while there is a loss of quaternary structure, the HDX protection and therefore secondary structures for each domain are similar for both states, indicating that each protomer is still structured and not denatured – a feature uniquely addressable by HDX.

2.2.4 Effect of sequence changes—HexaPro

The small energetic difference between these states indicates that small changes in sequence may affect the relative populations and/or rates of interconversion between them. Indeed, the S-2P variant was designed to stabilize the pre-fusion conformation avoiding spontaneous conversion to the post-fusion form. This S-2P construct is the basis for most currently employed vaccines. Shortly after the determination of the S-2P structure by cryo-EM, a new version was constructed, termed HexaPro or S-6P, which contains four additional proline mutations designed to increase the apparent stability of the pre-fusion state and improve cellular expression (31).

Using the same pulsed-labeling HDX-MS process, HexaPro shows the same bimodal behavior, with the same regions reporting on the two conformations (see Fig. 6A, Fig. 7B). At 4 °C, HexaPro, like S-2P, converts to state B, but with slower kinetics (t1/2 of ~6 days). At 37 °C HexaPro shifts back to state A with a t1/2 of ~2 hours (Fig. 6C). In sum, as expected based on the design criteria, HexaPro does result in a bias towards the prefusion conformation. Importantly, these changes demonstrate how a small number of mutations can perturb and modulate the conformational landscape of spike, suggesting that the evolving sequence variants may show differences in this conformational exchange (see below).

2.2.5 Effects of sequence changes—an interprotomer disulfide bond

To further probe the structural features of the B conformation, we turned to a variant of HexaPro engineered to contain a disulfide bond. This variant trimer contains three disulfide bonds (S383C/D985C) that reach across protomers and lock the RBDs in the down state (32–34). When probed by continuous-exchange HDX-MS we find that this disulfide-locked variant remains completely in the A state and does not show any observable population of the B state, even after O/N incubation at 25 °C (Fig. 5C). These data are consistent with a model where formation of the B state requires opening of the inter-protomer (trimer) interface and exposure of the RBDs, which would be prohibited by the interprotomer crosslinks.

2.2.6 Effects of sequence changes—B.1.1.7 (Alpha) variant.

Increasingly infectious SARS-CoV-2 variants of concern are being discovered throughout the global population on a regular basis. Most of these include mutations in the spike protein, primarily in the S1 domain; some reside in the ACE2-interaction surface, while others do not. Therefore, we asked if these mutations can influence the biases and kinetics of interconversion of the A and B conformation. We monitored the A/B conversion for a variant of HexaPro that includes five S1 mutations in the B.1.1.7 (alpha) variant and none in the S2, (Δ69–70 (NTD), Δ144 (NTD), N501Y(RBD), A570D (SD1), P681H (SD2)), termed alpha S1 HexaPro. Indeed, alpha S1 HexaPro shows notable differences in both the relative preference for state B and the kinetics of

interconversion. At 4 °C, alpha S1 HexaPro converts to state B nearly 20 times faster than HexaPro (Fig. 6C, Table 1). Furthermore, alpha S1 HexaPro shows no detectable prefusion conformer at 4 °C, while HexaPro shows at least 30% even after several weeks at 4 °C (Fig. 7B). At 37 °C, the kinetics and equilibrium distribution appear nearly

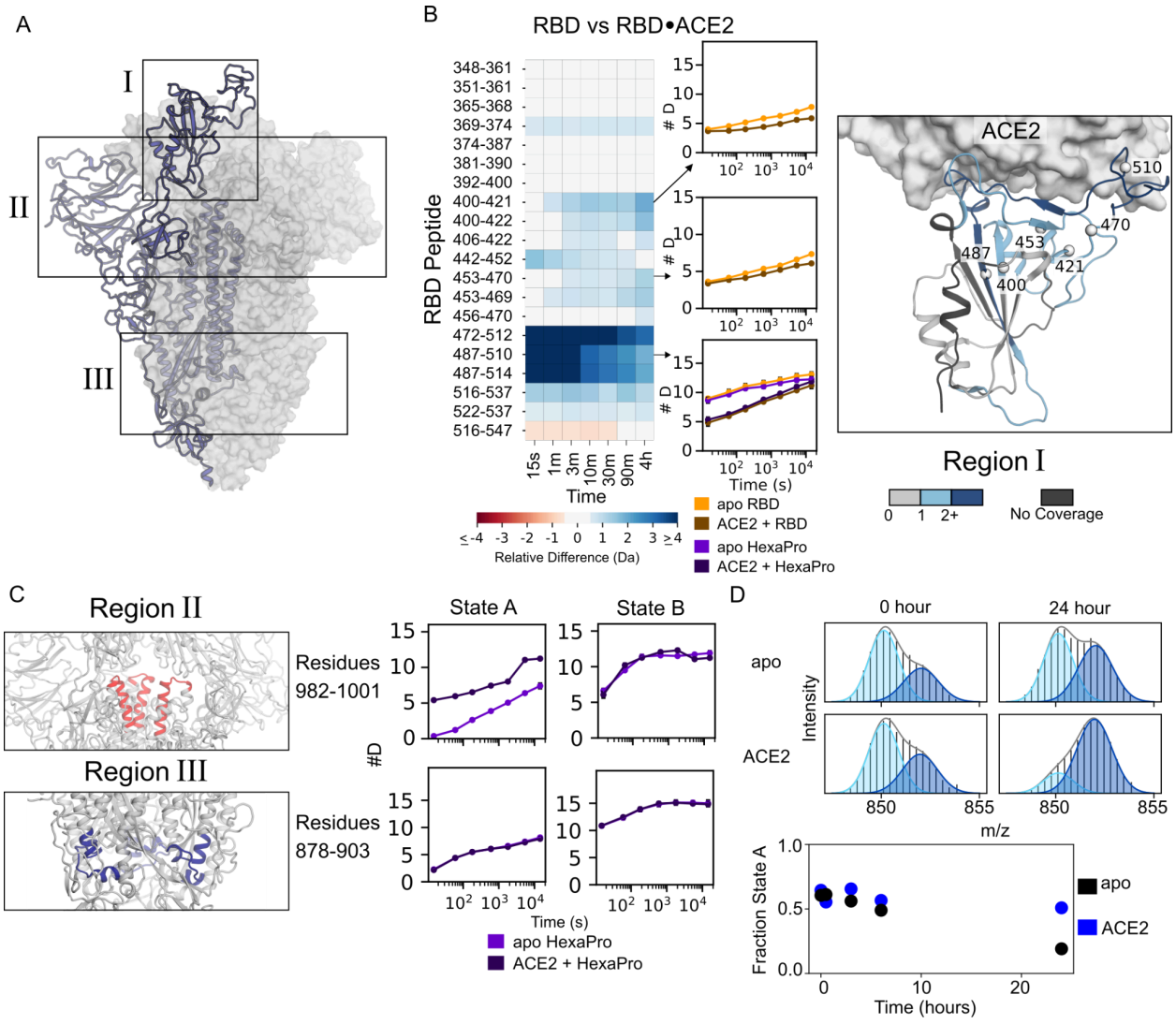

Figure 8: ACE2-binding effects are similar on isolated RBD and RBD in the context of the full-length ectodomain. **(A)** Diagram of the spike structure with regions of interest highlighted. **(B)** Left: Heatmap showing the difference in RBD peptide deuteration (from continuous-exchange HDX-MS) in the presence and absence of ACE2 on the isolated RBD. Middle: The deuterium uptake plots are illustrated for three peptides of interest with error bars representing the standard deviation of three replicates (some are smaller than marker size). The uptake plot for the RBM (residues 487- 510) is shown for both the isolated RBD and HexaPro. Right: Schematic representation of the heatmap data on the structure of the RBD•ACE2 complex (PDB 6M0J). The structure of the RBD is colored based on the maximum change shown in the heatmap for that residue in any peptide. **(C)** Changes to peptides from

HexaPro upon binding of ACE2 outside of the RBD during continuous-exchange HDX-MS. When ACE2 binds the canonical prefusion structure, state A, peptide 982-1001 (Region II) loses inter-subunit contacts with the RBD and thus exchanges faster, but when ACE2 binds the open trimer (state B) it does not, presumably because it is already maximally exposed. For peptide 878-903 (Region III), there is no change in the exchange rate to either state A or state B indicating this region is not affected by ACE2 binding. In the schematic for region II, one NTD has been removed to visualize the peptide of interest. **(D).** Time course of interconversion in the presence of ACE2. Top: Pulsed-labeling HDX-MS example spectra of S-2P peptide 878-902 with and without ACE2 before and after 24 hours of incubation at 25 °C. Bottom: time vs fraction state A for peptide 878-902 in S-2P with and without ACE2 over 24 hours monitored by pulsed-labeling. After 24 hours ACE2 bound S-2P prefers state B.

identical between the two. All of the mutations are at solvent-exposed residues, except residue 570, which contacts the S2 subunit and resides in a region with observed bimodal behavior. Thus, despite their location in the S1 subunit and not at the core trimer interface, these specific B.1.1.7 mutations allosterically affect the interconversion of these two states.

2.2.7 Effects of ACE2 binding

The primary function of the RBD is to recognize the host cell receptor ACE2. In the down conformation, the RBD is occluded from binding to ACE2, and in the up conformation its accessible. The entire trimer can exist with zero, one, two, or all three RBDs in the up conformation (7, 15). In the isolated RBD, the Receptor Binding Motif (RBM) should always be accessible for ACE2 binding. We used continuous-exchange HDX to monitor the binding of the receptor, both in isolation and in the full-length spike (S-2P), using a soluble dimeric form of ACE2 (ACE2-Fc, herein referred to as ACE2). For isolated RBD (residues 319–541, see Materials and Methods), we obtained 141 peptides, including one glycosylated peptide spanning the N-glycosylation site at residue 343 (no peptides are observed for site 331), resulting in 82% sequence coverage with an average redundancy of 8 (Fig 3A).

The effects of ACE2 binding are illustrated in Figure 4. In the presence of ACE2, the latter half of the RBM (residues 472–513), shows a notable decrease in hydrogen exchange upon binding ACE2 (Fig. 8B), consistent with the known ACE2/RBD binding interface (35, 36). We also observe small, but significant, changes for other regions that are near the binding interface. Importantly, we see very similar changes in HDX rates in RBD for both the isolated domain and in the context of the spike ectodomain, suggesting that all three RBDs in full-length spike interact with ACE2 in our experiment and that both the A and the B state can productively bind ACE2, which for the prefusion (A) state requires that RBD transition to the up state.

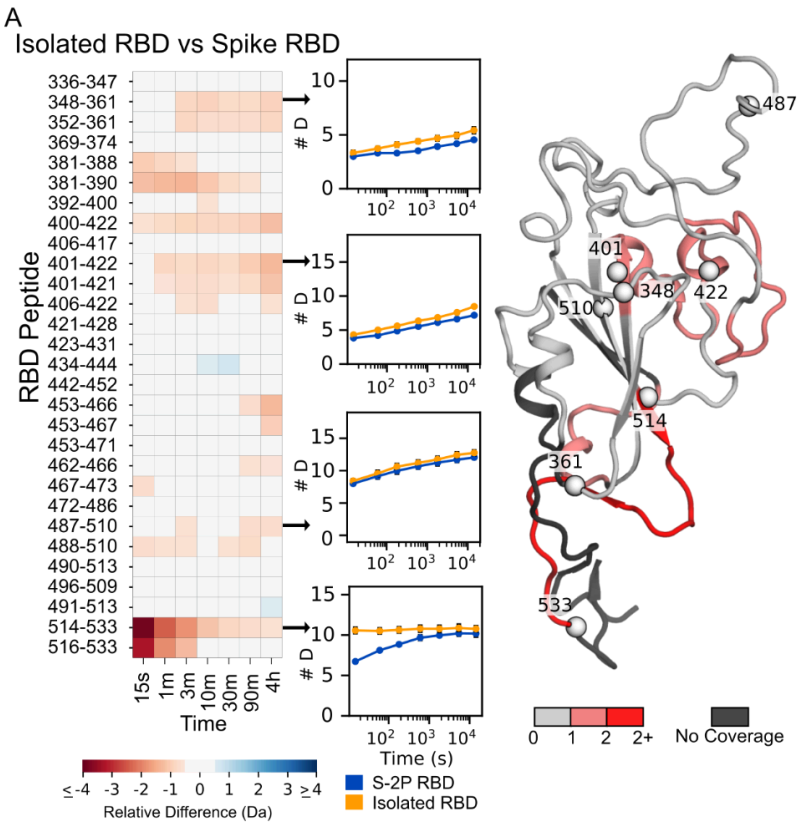

Figure 5: Comparison of HDX on RBD in isolation versus in S-2P
Left: Heat map showing the difference in peptide deuteration for isolated RBD compared to the RBD in S-2P. Middle: Selected uptake plots of isolated RBD and S-2P RBD. Right: Structure of the RBD (model of a single RBD taken from a full-length spike trimer model from (24)) colored based on the maximum change shown in the heat map for that residue in any peptide. For reference, spheres are shown denoting the beginning and end of the peptides displayed in the uptake plots.

In the context of the spike trimer, we also observe notable changes outside of the RBD, particularly in state A, where a few peptides exchange more rapidly in the presence of ACE2 (in state B these peptides do not have any notable difference in the presence of ACE2) (Fig. 8C). These peptides are located on the top of S2 (residues 978–1001), a region known to become more exposed when RBD transitions from a down to an up conformation. Since ACE2 binding in the prefusion state requires the RBDs to be in the up conformation, this increased exchange reflects the known biases in the RBD conformation—a prefusion state whose RBDs are primarily in the down conformation and must transition to an up conformation to bind ACE2. We also see changes in the interconversion between state A and state B in the presence of ACE2, such that state B is more preferred (Figure 4D).

2.2.8 The dynamics of the RBD are similar in isolation and the intact spike trimer

The isolated RBD has been used for many biochemical studies and is the main component of many clinical diagnostics. It is therefore important to ask whether there are large differences in the RBD when it is in isolation versus in the context of the spike trimer; our experiments allow us to directly compare the two. Very few peptides in the RBD show substantial changes in HDX behavior (Fig. 9) and support the use of approaches such as deep sequence mutagenesis on the isolated RBD to gain information on the potential effects of variants, such as escape mutations (37).

We do, however, see some key differences in the RBD—mostly at the termini of the isolated domain and in the expected interactions with the rest of spike and across the protomer interface. The C-terminal region of the RBD (residues 516–537) is notably less protected in the isolated domain. This region is not part of the RBD globular domain and in full-length spike forms part of subdomain 1, so it is not surprising that there would be an increase in flexibility when isolated from the rest of this subdomain. Future studies with the isolated RBD may benefit from removal of both C-terminal and N-terminal (no peptide coverage observed for this region) regions, as they are likely disordered and may interfere with crystallization or lead to increases in aggregation.

2.2.9 3A3—an antibody that binds specifically to the B state

Recently, an antibody, 3A3, was developed that binds to MERS-CoV, SARS-CoV-1, and SARS-CoV-2, with an apparent epitope in a region where we observe bimodal behavior (residues ~980–1000) (28). This region, however, is inaccessible in the prefusion structure—it is buried in the prefusion structure when all RBDs are down, and highly occluded when the RBDs are up. Our HDX data indicate that this region is exposed in state B. To confirm the epitope, we repeated the continuous-exchange HDX studies in the presence of 3A3; indeed, we see strong increased protection in the 978–1001 region. Moreover, this protection is directly associated with state B as evidenced by the now unimodal distribution for peptides in region 978-1001 (Fig 10A). This unimodal distribution can be explained by a decrease in hydrogen exchange in state B due to direct binding of 3A3 to this region such that the exchange is similar in both the A and B state. These data support a model where the 3A3 antibody binds uniquely to the B state.

To confirm this hypothesis, we looked at the effect of 3A3 binding on the temperature-induced conversion between A and B using our pulsed-labeling HDX-MS method. 3A3 increases the rate of conversion from A to B at 4 °C, decreasing the $t_{1/2}$ from ~17 hours to ~5 hours (Fig. 10B, Table 1). This increase in the observed rate implies that 3A3 also affects the transition state for the conversion. Furthermore, returning the sample to 37 °C in the presence of 3A3 (state B saturated with 3A3) prohibits any transition back to the prefusion state, indicating that the binding of 3A3

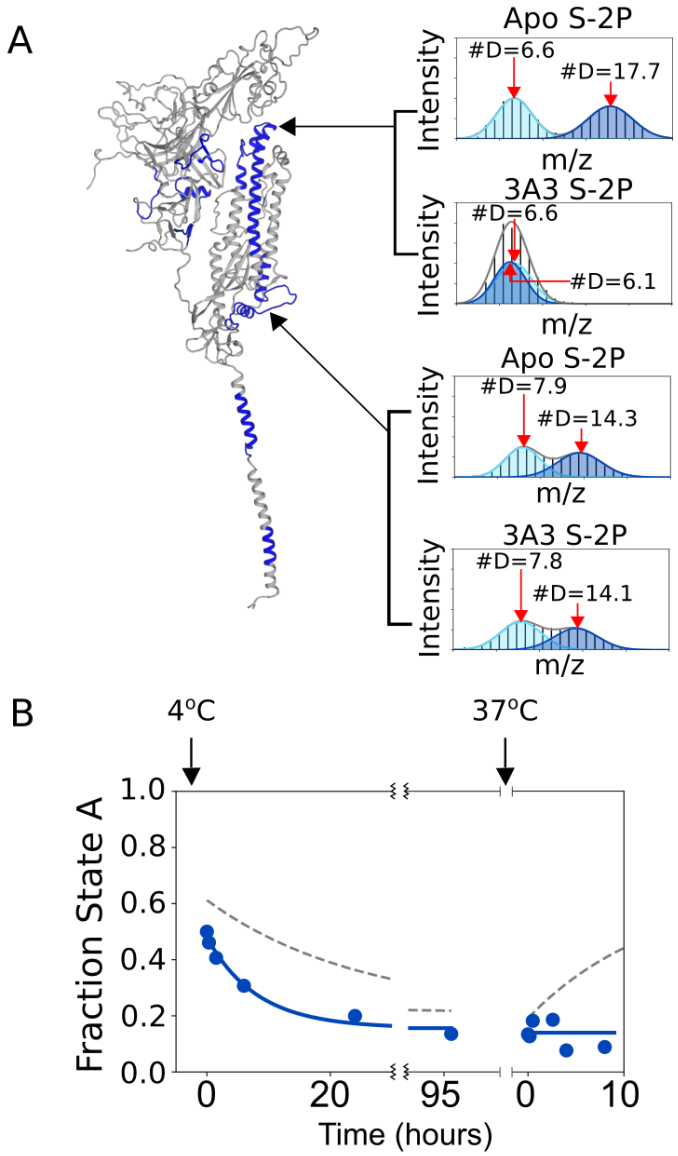

Figure 10: The antibody 3A3 binds selectively to state B in the 978-1001 region. (A) Example mass spectra for S-2P with and without 3A3 for two different peptides that have bimodal mass distributions. The bottom peptide (878-902) shows no change in the presence of 3A3, which indicates that the amount of state A and state B has not significantly changed 13 minutes after adding 3A3. The top peptide (978-1001), however, shows significant protection in the presence of 3A3, shifting the distribution belonging to state B to a deuteration amount indistinguishable from state A. These data are the three-minute time point from a continuous-exchange HDX-MS time course. **(B)** The kinetics of interconversion of S-2P in the presence of 3A3 monitored by pulsed-labeling HDX-MS. The addition of 3A3 accelerated the rate of conversion to state B at 4 °C. The binding of 3A3 prevents the return to state A at 37 °C. Dotted lines indicate the conversion in the absence of 3A3.

prevents formation of the prefusion state most likely due to steric hindrance of the antibody being bound to the trimer interface. Since 3A3 binds wild-type and D614G spike when expressed on the surface of cells and neutralizes pseudovirus expressing these spikes (28), the data collectively suggest state B exposes broadly neutralization-sensitive epitopes that may be of interest for future therapeutics and vaccines.

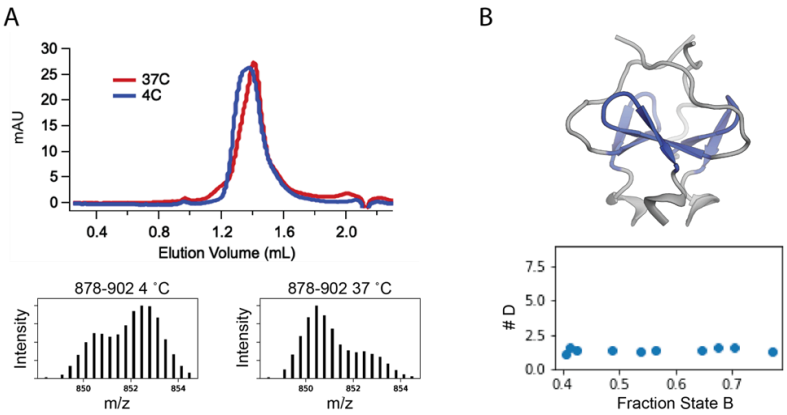

Figure 11. State A and state B are both Trimeric.
(A) Top: SEC (Superose 6 increase 3.2/300) traces from S-2P after incubation at 37 °C and 4 °C. Bottom: MS spectra of a bimodal peptide (878 -902) from each sample taken immediately before SEC experiment. (B) Top: Structure of the T4 Fibritin trimerization domain (PDB 1RFO) with peptide shown in blue. Bottom: peptide deuterium uptake at one minute as a function of fraction state B

2.3 Discussion

2.3.1 Structural model for proposed novel conformation

The above data allow us to create a structural model for state B (Fig. 12). The overall fold, or topology, of each domain is likely similar to the prefusion structure as, with the exception of the bimodal peptides, their hydrogen exchange patterns are similar. The bimodal peptides, which report on the two different conformations, cluster in the trimer interface, suggesting that this interface is less protected in state B. State B is not a monomer. Size-exclusion chromatography combined with multi-angle light scattering (SEC-MALS) and the hydrogen exchange data at the trimerization motif, confirm that both conformations are trimeric (Fig. 11). In these soluble ectodomain constructs, the trimer is held together by the appended C-terminal trimerization domain, while in the full-length native spike trimer, the transmembrane helical segment likely serves this function. Therefore, state B is best modeled as an opened-up trimer with three protomers whose domains are structurally uncoupled. Our data do not let us address the relative orientation of the protomers within individual trimers; however, an ensemble of opened-up trimers with heterogeneous positioning of the protomers would

best explain the lack of cryo-EM data. An opened-up class 1 viral fusion protein has been reported for respiratory syncytial virus (RSV) and visualized by a low resolution structure (38). This structural data from RSV and reports of an opening up of other viral fusion proteins (39–41) support our model of an ensemble of open-trimers with various degrees of openness.

We propose that this conformational change occurs because the trimer interface of the spike protein consists of weak, hydrophobic interactions which are further weakened at low temperatures. This can be thought of as a form of cold denaturation where the open trimer has a higher heat capacity than the canonical prefusion structure, consistent with solvation of the hydrophobic trimer interface (Fig. 12). As for what is responsible for the slow rate of interconversion, this is still unknown. We believe that in order for state B to be formed all three RBDs would need to be in the up position, which could be the rate-limiting step for the formation of state B, and thus the slow rate may be a result of the intertwined nature of the trimer. While it is known that RBDs moving up and down occurs on the order of seconds, having all three RBDs being open simultaneously long enough for the trimer interface to disassociate, may be rare enough to result in a high kinetic barrier. Similarly, the role of the designed prolines (in S-2P and HexaPro) is unclear. The rates of interconversion are not consistent with a model where the isomerization of prolines is playing a role. Rather, our data are consistent with the model where the introduction of prolines successfully stabilizes the prefusion conformation.

A loss of interprotomer contacts in state B implies that the RBDs no longer contact adjacent protomers, and thus do occupy distinct ‘down’ and ‘up’ conformations; rather, they are likely always in a binding-competent state, perhaps even more accessible than the canonical ‘up’ state. This increased availability of the RBD may drive a preference for the B state in the presence of ACE2. Furthermore, in the prefusion conformation, having all three RBDs bound to ACE2 could lead to steric hindrances, but in state B, all three RBDs should be able to bind ACE2 with high affinity. Interestingly, introduction of variants of concern, such as in the alpha S1 HexaPro variant greatly increases the rate of conversion to state B. Whether this plays a role in the noted increased infectivity remains to be determined.

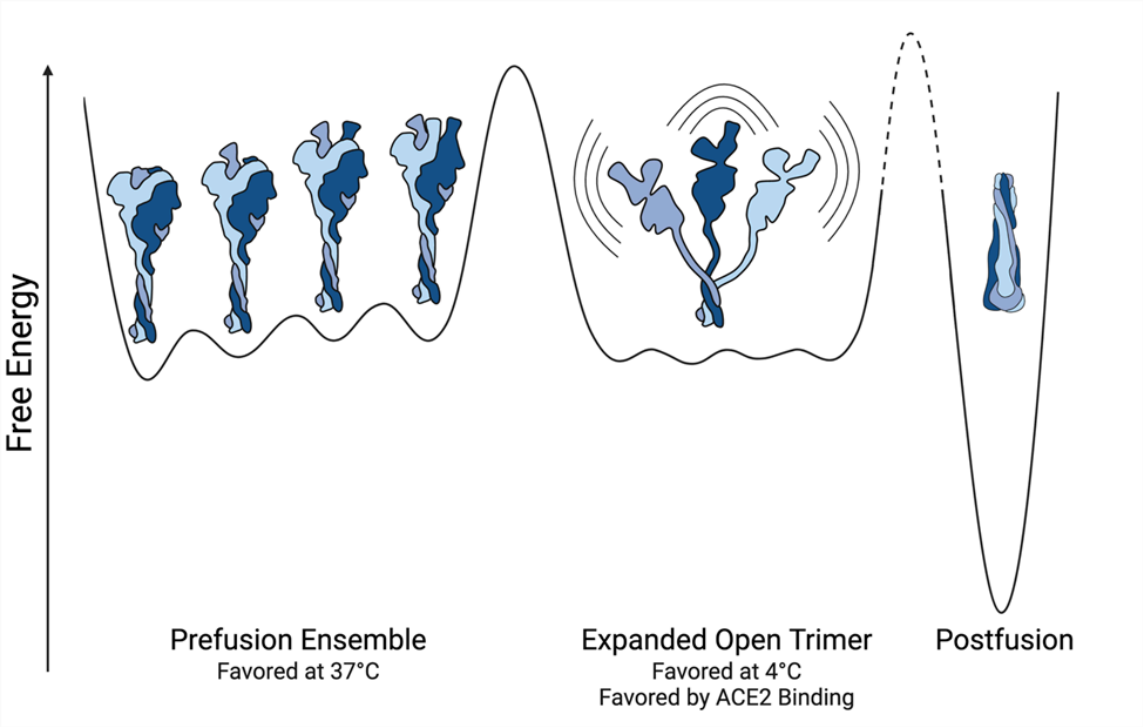

Figure 12. Schematic of the energy landscape for the SARS-CoV-2 Spike ectodomain.
Reaction coordinate illustrating the different conformations accessible by Spike. Three different conformational states are depicted: the canonical prefusion ensemble, the expanded open trimer, and the postfusion conformation. The prefusion conformation contains all four RBD states (0,1,2, or 3 up). The relative energies and barrier heights as well as the placement of the open trimer along the reaction coordinate are drawn for illustration only.

Molecular dynamics has shown a smaller opening of the spike protein where an RBD and adjacent NTD twist and peel away from the center of the spike protein, revealing a cryptic epitope at the top of the S2 domain (20). This rapidly sampled conformation is not state B, as it does not involve the S2 trimer interface and the timescale of conversion to state B is unlikely to be sampled during a molecular dynamics simulation. This partial opening, however, could be on pathway to state B.

2.3.2 A potential role for state B in spike function

The increase in the formation of state B upon binding ACE2 suggests that state B may be a functional intermediate. While we cannot say whether this transition occurs in wild-type spike on virions, it is possible that state B represent an intermediate along the pathway to S1 shedding during the transition from the prefusion conformation to the postfusion conformation. This irreversible transition is not possible in the soluble ectodomain which removes the proteolytic cleavage site. If this is an on-pathway intermediate, antibodies or ligands that trap the protein in this state may block the

protein along the pathway to fusion (42) those that act on the transition state and increase the rate of formation of the intermediate could promote the premature formation of the postfusion conformation and thus aid in neutralization. If instead, formation of state B is off-pathway, antibodies or other ligands that favor state B would essentially trap the protein in an inactive conformation.

2.3.3 The presence of this alternative conformation presents new druggable sites

Based on our model, the newly identified B state contains a large and unique accessible surface area that is buried in the canonical prefusion conformation, thus exposing different epitopes for antibody and ligand recognition. Moreover, these regions arise from the most highly conserved part of the protein, the S2 trimer interface, and therefore may present an ideal target for vaccines that would provide protection across coronaviruses (pan-coronavirus). In terms of therapeutics, ligands directed towards this region may also be broadly efficacious against variants of concern as well as other coronaviruses. Indeed, the antibody 3A3 represents one such potential therapeutic.

2.3.4 The presence of state B will affect measured ligand-binding affinities

Finally, independent of whether this additional conformation is an on-pathway intermediate in the coronavirus functional lifecycle, it is ubiquitous among in vitro preparations of the spike protein. We see evidence of this conformation in every variant examined, excluding the disulfide-locked sample. Many biochemical and diagnostic assays use these isolated spike constructs, and many laboratories store this protein at 4 °C, where the alternative, expanded conformation is favored. Given that state A and B have differing affinities for the receptor and some antibodies, the temperature and time-dependent changes in the population of state B complicates quantitative analysis of binding affinities and needs to be further evaluated.

2.4 Conclusion

In sum, we have found that the SARS-CoV-2 spike ectodomain reversibly samples an open-trimer conformation, potentially allowing for the development of pan-coronavirus vaccines and therapeutics. This open trimer is folded and exposes a highly conserved region of the protein. It is similar in energy to the well-characterized prefusion conformation determined by cryo-EM. The fraction of spike in each conformer depends on temperature, ligands, and sequence. Mutations, receptor binding, antibodies, and temperature all affect the kinetics and energetics of this conformational change. Thus, quantitative measurements, such as in vitro binding assays, need to be re-evaluated for possible effects due to this mixed population. How easily this conformation is sampled in natural membrane-bound spike and its position in the viral lifecycle are still unknown; however, an antibody specific for this conformation can bind and neutralize in in vitro SARS-CoV-2 cell fusion and pseudovirus assays suggesting an

important role. Determining which conformation elicits more robust protective immunity against both SARS-CoV-2 variants and other coronaviruses will be important for future vaccine development.

2.5 Methods

2.5.1 Protein expression and purification

SARS-CoV-2 Spike (2P) and RBD were expressed and purified from stably transformed Expi293 cells, following methods as described (43). Briefly, stable Expi293 suspension cells were maintained in Expi293 media at 37°C. Cells were grown for 6 days, then harvested by centrifugation, and filtered. Supernatant was adjusted to pH 7.4 and loaded onto a 5 mL HisTrap Excel column and washed with 60 CV of buffer. Captured proteins were eluted with 10 CV of (20 mM sodium phosphate, 500 mM NaCl, 500 mM imidazole, pH 7.4). Eluted proteins were buffer exchanged into PBS using either 3kDa MWCO (for RBD) or 100 kDa MWCO (for Spike) Amicon concentrators and filtered prior to storage at -80°C. HexaPro, HexaPro S383C/D985C, and alpha S1 HexaPro were expressed and purified from transiently transfected Freestyle 293-F cells as described (31). Briefly, cell cultures were harvested four days after transfection and centrifuged. Supernatants were filtered and flowed over StrepTactin resin (IBA). Proteins were further purified by size-exclusion chromatography using a Superose 6 increase column (GE Healthcare) in a buffer composed of 2 mM Tris pH 8.0, 200 mM NaCl and 0.02% NaN3. ACE2-Fc was a gift from the Wells lab (44). 3A3 IgG was expressed and purified from ExpiCHO cells as described (28). Briefly, Antibodies were expressed in ExpiCHO cells according to the high titer protocol provided and purified on a Protein A HiTrap column (GE Healthcare) and buffer exchanged to PBS.

2.5.2 Continuous hydrogen exchange labeling

For all continuous hydrogen exchange experiments, deuterated buffer was prepared by lyophilizing PBS (pH 7.4, Sigma-Aldrich P4417) and resuspending in D2O (Sigma-Aldrich 151882). To initiate the continuous exchange experiment, samples were diluted 10-fold (final spike trimer concentration of 0.167 μM) into temperature equilibrated deuterated PBS buffer (pHread 7, pD 7.4). Samples were quenched, at the timepoints outlined below, by mixing 30 μL of the partially exchanged protein with 30 μL of 2x quench buffer (3.6 M GdmCl, 500 mM TCEP, 200 mM Glycine pH 2.4) on ice. Samples were incubated on ice for one minute to allow for partial unfolding to assist with proteolytic degradation and then flash frozen in liquid nitrogen and stored at -80°C.

For studies comparing HexaPro ± ACE2 the RBD in isolation vs in S-2P, purified spike (1.67 μM spike trimer or 5 μM RBD) was incubated in PBS at 25°C overnight (12-16 hours) before the initiation of hydrogen exchange. For experiments done in the presence of ACE2-Fc, the ligand was added during this incubation at a 1.25:1 molar ratio of ligand to spike monomer (6.25 μM ligand) to ensure saturation. Based on the

reported affinity (KD ~15 nM) for ACE2-Fc, fraction bound can be assumed to be greater than 97%. The hydrogen exchange time points for these experiments were 15 seconds, 60 seconds, 180 seconds, 600 seconds, 1800 seconds, 5400 seconds, and 14400 seconds.

For the comparison of HexaPro ± 3A3, HexaPro was incubated overnight at 37 °C (12-16 hours). After incubation the protein was moved to 25 °C and diluted to 1.67 μM spike trimer. In the 3A3 bound condition, 6.25 μM antibody was added and allowed to bind for 10 minutes at 25 °C. Given the affinity of 3A3 for HexaPro (12 nM, fraction bound can be assumed to be greater than 97%. The quench time points for this experiment were 15 seconds, 180 seconds, 1800 seconds and 14400 seconds.

2.5.3 Back exchange control preparation

S-2P was diluted to 1.67 μM trimer in PBS pH 7.4. To initiate hydrogen exchange, the sample was diluted 10-fold (final spike trimer concentration of 0.167 M) into deuterated PBS buffer (pHread 7, pD 7.4) that was supplemented with 3.6 M GdmCl, and then incubated at 37 °C. The addition of denaturant and increased temperature should both promote hydrogen exchange, by destabilizing folded structures and increasing the intrinsic rate of hydrogen exchange, respectively. Following two weeks of exchange, 30 μL of deuterated spike was mixed with 30 μL of 2X quench buffer lacking denaturant (500 mM TCEP, 200 mM Glycine pH 2.4) and kept on ice for one minute prior to flash freezing in liquid nitrogen and storage at -80 °C. The results of this control experiment were used to characterize the back exchange of the system and were not used to adjust deuteration values of continuous-exchange experiments.

2.5.4 Incubation kinetics and pulse labeling

For evaluating the temperature dependent kinetics of interconversion, frozen spike samples were thawed, diluted to 5 μm spike monomer, and incubated at 37°C overnight. Samples were then moved to a temperature-controlled chamber at 4°C and the population of each state was evaluated at the specified time points as described below. After the final 4 °C sample was taken (96–526 hours, depending on the spike construct), the sample was returned to a 37° heat block for further incubation and the population of each state was again evaluated at the specified time points as described below. To evaluate the relative population of the A and B conformer at each time point, 3 μL of spike sample was removed from the incubation tube and mixed with 27 μL of room temperature deuterated buffer. After a one-minute labeling pulse, 30 μL of quench buffer kept on ice was mixed with the 30 μL of labeled protein. Quenched samples were kept on ice for one minute to allow for partial unfolding, and then flash frozen in liquid nitrogen.

For kinetics carried out in the presence of ACE2 or 3A3, after the initial 37 °C incubation the sample was brought to 25 °C and ligand was added (6.25 μM). To monitor the

population of state A and B as a function of time at 25 °C in the presence of ACE2 the sample was kept in a temperature-controlled chamber at 25 °C and aliquots were removed for pulse labeling as described above at 0 hours, 30 minutes, 3 hours, 6 hours and 24 hours.

2.5.5 Protease digestion and LC/MS

All samples were thawed immediately before injection into a cooled valve system (Trajan LEAP) coupled to a LC (Thermo UltiMate 3000). Sample time points were injected in random order. The temperature of the valve chamber, trap column, and analytical column were maintained at 2 °C. The temperature of the protease column was maintained at 10 °C. The quenched sample was subjected to inline digestion by two immobilized acid proteases in order, aspergillopepsin (Sigma-Aldrich P2143) and porcine pepsin (Sigma-Aldrich P6887) at a flow rate of 200 µL/min of buffer A (0.1 % formic acid). Protease columns were prepared in house by coupling protease to beads (Thermo Scientific POROS 20 Al aldehyde activated resin 1602906) and packed by hand into a column (2mm ID x 2 cm, IDEX C-130B). Following digestion, peptides were desalted for 4 minutes on a hand-packed trap column (Thermo Scientific POROS R2 reversed-phase resin 1112906, 1 mm ID x 2 cm, IDEX C-128). Peptides were then separated with a C8 analytical column (Thermo Scientific BioBasic-8 5 µm particle size 0.5 mm ID x 50 mm 72205-050565) and a gradient of 5-40% buffer B (100% Acetonitrile, 0.1% Formic Acid) at a flow rate of 40 µL/min over 14 minutes, and then of 40-90% buffer B over 30 seconds. The analytical and trap columns were then subjected to a sawtooth wash and equilibrated at 5% buffer B prior to the next injection. Protease columns were washed with two injections of 100 µL 1.6 M GdmCl, 0.1% formic acid prior to the next injection. Peptides were eluted directly into a Q Exactive Orbitrap Mass Spectrometer operating in positive mode (resolution 70000, AGC target 3e6, maximum IT 50 ms, scan range 300-1500 m/z). For each spike construct, a tandem mass spectrometry experiment was performed (Full MS settings the same as above, dd-MS2 settings as follows: resolution 17500, AGC target 2e5, maximum IT 100 ms, loop count 10, isolation window 2.0 m/z, NCE 28, charge state 1 and ≥7 excluded, dynamic exclusion of 15 seconds) on undeuterated samples.

2.5.6 Peptide identification

Byonic (Protein Metrics) was used to identify unmodified and glycosylated peptides in the tandem mass spectrometry data. The sequence of the expressed construct, including signal sequence and trimerization domain, was used as the search library. Sample digestion parameters were set to non-specific. Precursor mass tolerance and fragment mass tolerance was set to 6 and 10 ppm respectively. Variable N-linked glycosylation was allowed, with a library of 132 human N-glycans used in the search. No non-glycosylated peptides spanning any of the 22 known glycosylation sites in the spike sequence were ever observed, independent of the glycosylation search

parameters. Peptide lists (sequence, charge state, and retention time) were exported from Byonic and imported into HDExaminer 3 (Sierra Analytics). When multiple peptide lists were obtained, all were imported and combined in HDExaminer 3.

2.5.7 HDExaminer 3 analysis

Peptide isotope distributions at each exchange time point were fit in HDExaminer 3. For glycosylated peptides, only the highest confidence modification was included in the mass spectra search and analysis. For unimodal peptides, deuteration levels were determined by subtracting mass centroids of deuterated peptides from undeuterated peptides. For bimodal peaks, extracted peptide isotope spectra were exported from HDExaminer 3 and analyzed separately (see below for details).

2.5.8 Bimodal fitting and conformation quantification

Peptide mass spectra for bimodal peptides were exported from HDExaminer 3.0. All quantitative analysis of the exported peptide mass spectra was performed using python scripts in Jupyter notebooks. After importing a peptide mass spectra, the m/z range containing all possible deuteration states of the selected peptide was isolated and the find_peaks method from the scipy.signal package was used to identify each isotope in the mass envelope and the height of each peak was used as its intensity. The area of the total mass envelope was normalized to account for run-to-run differences in intensity. The bimodal mass envelopes for all timepoints under the same condition were globally fit to a sum of two gaussians, keeping the center and width of each gaussian constant across all incubation time points. Fitting was done using the curve_fit function from the scipy.optimize package. After fitting, the area under each individual gaussian was determined to approximate the relative population of each state.

2.5.9 Size Exclusion Chromatography – Multiangle Light Scattering (SEC-MALS)

To generate variable populations of states A and B, S-2P (100 µL, 0.18 mg/mL) was incubated at either 4 °C or 37 °C for four days. Post-incubation, and prior to SEC-MALS injection, an aliquot from each sample was taken and a one-minute pulse-labeling experiment was performed (see above). The resulting bimodal peptide distributions were used to calculate a fraction state A and B. Samples were filtered (0.22 µm hydrophilic polyvinylidene fluoride Ultrafree-MC GV centrifugal filter) prior to SEC-MALS injection. 90 µL of sample (0.18 mg/mL) was then injected onto a Superose 6 increase 10/300 (GE Healthcare) pre-equilibrated in filtered (0.1 µm polyethersulfone Nalgene Rapid-Flow vacuum filter) PBS flowing at 0.5 ml/min at 4 °C. The ÄKTA Pure 25 M1 (Cytiva) chromatography system was coupled to an 18-angle light scattering Wyatt Dawn detector and Wyatt Optilab refractive index detector (Wyatt Technology). Data analysis was carried out using the program ASTRA 7.1.4.8.

2.6 Acknowledgements

We thank the entire Marqusee Lab for advice and critical reading of the manuscript, particularly Johanna Lindner for help initiating these experiments. We thank Peter S. Kim, Abigail Powell, Payton Weidenbacher, and Natalia Freedland for advice and discussion; Jim Wells, Shion Lim, and Irene Lui for discussion and providing ACE2-Fc; Yifan Cheng, Adamo Mancino, and Mingliang Jin for assistance with SEC-MALS and Aashish Manglik for advice and discussion. We thank Jeff Morrow and Sierra Analytics for making HDExaminer freely available for at-home use during shelter-in-place orders. SM is a Chan Zuckerberg Biohub Investigator. Some figures were created with the use of BioRender.com. This work was funded by NSF Graduate Research Fellowship DGE1752814 (SMC); NIH grant no. GM050945 (SM); and NSF grant no. MCB1616591 (SM); NIH grant no. AI127521 (JSM); Welch foundation grant no. F-0003-19620604 (JSM); NIH grant no. AI122753 (JAM).

2.7 References

1. A. Baum, B. O. Fulton, E. Wloga, R. Copin, K. E. Pascal, V. Russo, S. Giordano, K. Lanza, N. Negron, M. Ni, Y. Wei, G. S. Atwal, A. J. Murphy, N. Stahl, G. D. Yancopoulos, C. A. Kyratsous, Antibody cocktail to SARS-CoV-2 spike protein prevents rapid mutational escape seen with individual antibodies. *Science*. **369**, 1014–1018 (2020).
2. P. C. Taylor, A. C. Adams, M. M. Hufford, I. de la Torre, K. Winthrop, R. L. Gottlieb, Neutralizing monoclonal antibodies for treatment of COVID-19. *Nat. Rev. Immunol.* **21**, 382–393 (2021).
3. J. Hansen, A. Baum, K. E. Pascal, V. Russo, S. Giordano, E. Wloga, B. O. Fulton, Y. Yan, K. Koon, K. Patel, K. M. Chung, A. Hermann, E. Ullman, J. Cruz, A. Rafique, T. Huang, J. Fairhurst, C. Libertiny, M. Malbec, W.-Y. Lee, R. Welsh, G. Farr, S. Pennington, D. Deshpande, J. Cheng, A. Watty, P. Bouffard, R. Babb, N. Levenkova, C. Chen, B. Zhang, A. Romero Hernandez, K. Saotome, Y. Zhou, M. Franklin, S. Sivapalasingam, D. C. Lye, S. Weston, J. Logue, R. Haupt, M. Frieman, G. Chen, W. Olson, A. J. Murphy, N. Stahl, G. D. Yancopoulos, C. A. Kyratsous, Studies in humanized mice and convalescent humans yield a SARS-CoV-2 antibody cocktail. *Science*. **369**, 1010–1014 (2020).
4. R. Shi, C. Shan, X. Duan, Z. Chen, P. Liu, J. Song, T. Song, X. Bi, C. Han, L. Wu, G. Gao, X. Hu, Y. Zhang, Z. Tong, W. Huang, W. J. Liu, G. Wu, B. Zhang, L. Wang, J. Qi, H. Feng, F.-S. Wang, Q. Wang, G. F. Gao, Z. Yuan, J. Yan, A human neutralizing antibody targets the receptor-binding site of SARS-CoV-2. *Nature*. **584**, 120–124 (2020).
5. Y. Watanabe, J. D. Allen, D. Wrapp, J. S. McLellan, M. Crispin, Site-specific glycan analysis of the SARS-CoV-2 spike. *Science*. **91**, eabb9983 (2020).
6. M. Hoffmann, H. Kleine-Weber, S. Schroeder, N. Krüger, T. Herrler, S. Erichsen, T. S. Schiergens, G. Herrler, N.-H. Wu, A. Nitsche, M. A. Müller, C. Drosten, S. Pöhlmann, SARS-CoV-2 Cell Entry Depends on ACE2 and TMPRSS2 and Is Blocked by a Clinically Proven Protease Inhibitor. *Cell*. **181**, 271-280.e8 (2020).
7. D. J. Benton, A. G. Wrobel, P. Xu, C. Roustan, S. R. Martin, P. B. Rosenthal, J. J. Skehel, S. J. Gamblin, Receptor binding and priming of the spike protein of SARS-CoV-2 for membrane fusion. *Nature*. **588**, 327–330 (2020).
8. S. Jiang, C. Hillyer, L. Du, Neutralizing Antibodies against SARS-CoV-2 and Other Human Coronaviruses. *Trends Immunol.* **41**, 355–359 (2020).
9. D. Wrapp, N. Wang, K. S. Corbett, J. A. Goldsmith, C.-L. Hsieh, O. Abiona, B. S. Graham, J. S. McLellan, Cryo-EM structure of the 2019-nCoV spike in the prefusion conformation. *Science*. **367**, 1260–1263 (2020).
10. A. C. Walls, Y.-J. Park, M. A. Tortorici, A. Wall, A. T. McGuire, D. Veesler, Structure, Function, and Antigenicity of the SARS-CoV-2 Spike Glycoprotein. *Cell*. **181**, 281-292.e6 (2020).
11. H. M. Berman, J. Westbrook, Z. Feng, G. Gilliland, T. N. Bhat, H. Weissig, I. N. Shindyalov, P. E. Bourne, The Protein Data Bank. *Nucleic Acids Res.* **28**, 235–242 (2000).

12. J. M. White, S. E. Delos, M. Brecher, K. Schornberg, Structures and mechanisms of viral membrane fusion proteins: multiple variations on a common theme. *Crit. Rev. Biochem. Mol. Biol.* **43**, 189–219 (2008).
13. F. Li, Structure, Function, and Evolution of Coronavirus Spike Proteins. *Annu Rev Virol*. **3**, 237–261 (2016).
14. T. Zhou, Y. Tsybovsky, J. Gorman, M. Rapp, G. Cerutti, G.-Y. Chuang, P. S. Katsamba, J. M. Sampson, A. Schön, J. Bimela, J. C. Boyington, A. Nazzari, A. S. Olia, W. Shi, M. Sastry, T. Stephens, J. Stuckey, I.-T. Teng, P. Wang, S. Wang, B. Zhang, R. A. Friesner, D. D. Ho, J. R. Mascola, L. Shapiro, P. D. Kwong, Cryo-EM Structures of SARS-CoV-2 Spike without and with ACE2 Reveal a pH-Dependent Switch to Mediate Endosomal Positioning of Receptor-Binding Domains. *Cell Host Microbe*. **28**, 867-879.e5 (2020).
15. T. Xiao, J. Lu, J. Zhang, R. I. Johnson, L. G. A. McKay, N. Storm, C. L. Lavine, H. Peng, Y. Cai, S. Rits-Volloch, S. Lu, B. D. Quinlan, M. Farzan, M. S. Seaman, A. Griffiths, B. Chen, A trimeric human angiotensin-converting enzyme 2 as an anti-SARS-CoV-2 agent. *Nat. Struct. Mol. Biol.* **28**, 202–209 (2021).
16. S. Belouzard, V. C. Chu, G. R. Whittaker, Activation of the SARS coronavirus spike protein via sequential proteolytic cleavage at two distinct sites. *Proc. Natl. Acad. Sci. U. S. A.* **106**, 5871–5876 (2009).
17. Y. Cai, J. Zhang, T. Xiao, H. Peng, S. M. Sterling, R. M. Walsh Jr, S. Rawson, S. Rits-Volloch, B. Chen, Distinct conformational states of SARS-CoV-2 spike protein. *Science*. **369**, 1586–1592 (2020).
18. A. C. Walls, M. A. Tortorici, J. Snijder, X. Xiong, B.-J. Bosch, F. A. Rey, D. Veesler, Tectonic conformational changes of a coronavirus spike glycoprotein promote membrane fusion. *Proc. Natl. Acad. Sci. U. S. A.* **114**, 11157–11162 (2017).
19. M. Lu, P. D. Uchil, W. Li, D. Zheng, D. S. Terry, J. Gorman, W. Shi, B. Zhang, T. Zhou, S. Ding, R. Gasser, J. Prévost, G. Beaudoin-Bussières, S. P. Anand, A. Laumaea, J. R. Grover, L. Liu, D. D. Ho, J. R. Mascola, A. Finzi, P. D. Kwong, S. C. Blanchard, W. Mothes, Real-Time Conformational Dynamics of SARS-CoV-2 Spikes on Virus Particles. *Cell Host Microbe*. **28**, 880-891.e8 (2020).
20. M. I. Zimmerman, J. R. Porter, M. D. Ward, S. Singh, N. Vithani, A. Meller, U. L. Mallimadugula, C. E. Kuhn, J. H. Borowsky, R. P. Wiewiora, M. F. D. Hurley, A. M. Harbison, C. A. Fogarty, J. E. Coffland, E. Fadda, V. A. Voelz, J. D. Chodera, G. R. Bowman, SARS-CoV-2 simulations go exascale to predict dramatic spike opening and cryptic pockets across the proteome. *Nat. Chem.* **13**, 651–659 (2021).
21. T. Sztain, S.-H. Ahn, A. T. Bogetti, L. Casalino, J. A. Goldsmith, E. Seitz, R. S. McCool, F. L. Kearns, F. Acosta-Reyes, S. Maji, G. Mashayekhi, J. A. McCammon, A. Ourmazd, J. Frank, J. S. McLellan, L. T. Chong, R. E. Amaro, A glycan gate controls opening of the SARS-CoV-2 spike protein. *Nat. Chem.*, 1–6 (2021).
22. S. W. Englander, Hydrogen exchange and mass spectrometry: A historical perspective. *J. Am. Soc. Mass Spectrom.* **17**, 1481–1489 (2006).

23. J. Zheng, T. Strutzenberg, B. D. Pascal, P. R. Griffin, Protein dynamics and conformational changes explored by hydrogen/deuterium exchange mass spectrometry. *Curr. Opin. Struct. Biol.* **58**, 305–313 (2019).
24. L. Casalino, Z. Gaieb, J. A. Goldsmith, C. K. Hjorth, A. C. Dommer, A. M. Harbison, C. A. Fogarty, E. P. Barros, B. C. Taylor, J. S. McLellan, E. Fadda, R. E. Amaro, Beyond Shielding: The Roles of Glycans in the SARS-CoV-2 Spike Protein. *ACS Cent. Sci.* **6**, 1722–1734 (2020).
25. B. Turoňová, M. Sikora, C. Schürmann, W. J. H. Hagen, S. Welsch, F. E. C. Blanc, S. von Bülow, M. Gecht, K. Bagola, C. Hörner, G. van Zandbergen, S. Mosalaganti, A. Schwarz, R. Covino, M. D. Mühlebach, G. Hummer, J. K. Locker, M. Beck, In situ structural analysis of SARS-CoV-2 spike reveals flexibility mediated by three hinges *Science*. **370**, 203-208 (2020).
26. C. O. Barnes, A. P. West Jr, K. E. Huey-Tubman, M. A. G. Hoffmann, N. G. Sharaf, P. R. Hoffman, N. Koranda, H. B. Gristick, C. Gaebler, F. Muecksch, J. C. C. Lorenzi, S. Finkin, T. Hägglöf, A. Hurley, K. G. Millard, Y. Weisblum, F. Schmidt, T. Hatziioannou, P. D. Bieniasz, M. Caskey, D. F. Robbiani, M. C. Nussenzweig, P. J. Bjorkman, Structures of Human Antibodies Bound to SARS-CoV-2 Spike Reveal Common Epitopes and Recurrent Features of Antibodies. *Cell*. **182**, 828-842.e16 (2020).
27. P. V. Raghuvamsi, N. K. Tulsian, F. Samsudin, X. Qian, K. Purushotorman, G. Yue, M. M. Kozma, W. Y. Hwa, J. Lescar, P. J. Bond, P. A. MacAry, G. S. Anand, SARS-CoV-2 S protein:ACE2 interaction reveals novel allosteric targets. *Elife*. **10** (2021), doi:10.7554/eLife.63646.
28. Y. Huang, A. W. Nguyen, C.-L. Hsieh, R. Silva, O. S. Olaluwoye, R. E. Wilen, T. S. Kaoud, L. R. Azouz, A. N. Qerqez, K. C. Le, A. L. Bohanon, A. M. DiVenere, Y. Liu, A. G. Lee, D. Amengor, K. N. Dalby, S. D'Arcy, J. S. McLellan, J. A. Maynard, Identification of a conserved neutralizing epitope present on spike proteins from all highly pathogenic coronaviruses. *bioRxiv* (2021), p. 2021.01.31.428824, , doi:10.1101/2021.01.31.428824.
29. M. A. Benhaim, V. Mangala Prasad, N. K. Garcia, M. Guttman, K. K. Lee, Structural monitoring of a transient intermediate in the hemagglutinin fusion machinery on influenza virions. *Sci. Adv.* **6**, eaaz8822 (05/2020).
30. R. J. Edwards, K. Mansouri, V. Stalls, K. Manne, B. Watts, R. Parks, K. Janowska, S. M. C. Gobeil, M. Kopp, D. Li, X. Lu, Z. Mu, M. Deyton, T. H. Oguin 3rd, J. Sprenz, W. Williams, K. O. Saunders, D. Montefiori, G. D. Sempowski, R. Henderson, S. Munir Alam, B. F. Haynes, P. Acharya, Cold sensitivity of the SARS-CoV-2 spike ectodomain. *Nat. Struct. Mol. Biol.* **28**, 128–131 (2021).
31. C.-L. Hsieh, J. A. Goldsmith, J. M. Schaub, A. M. DiVenere, H.-C. Kuo, K. Javanmardi, K. C. Le, D. Wrapp, A. G. Lee, Y. Liu, C.-W. Chou, P. O. Byrne, C. K. Hjorth, N. V. Johnson, J. Ludes-Meyers, A. W. Nguyen, J. Park, N. Wang, D. Amengor, J. J. Lavinder, G. C. Ippolito, J. A. Maynard, I. J. Finkelstein, J. S. McLellan, Structure-based design of prefusion-stabilized SARS-CoV-2 spikes. *Science*. **369**, 1501–1505 (2020).
32. R. Henderson, R. J. Edwards, K. Mansouri, K. Janowska, V. Stalls, S. M. C. Gobeil, M. Kopp, D. Li, R. Parks, A. L. Hsu, M. J. Borgnia, B. F. Haynes, P.

Acharya, Controlling the SARS-CoV-2 spike glycoprotein conformation. *Nat. Struct. Mol. Biol.* **27**, 925–933 (2020).
33. M. McCallum, A. C. Walls, J. E. Bowen, D. Corti, D. Veesler, Structure-guided covalent stabilization of coronavirus spike glycoprotein trimers in the closed conformation. *Nat. Struct. Mol. Biol.* (2020), doi:10.1038/s41594-020-0483-8.
34. The CITIID-NIHR COVID-19 BioResource Collaboration, X. Xiong, K. Qu, K. A. Ciazynska, M. Hosmillo, A. P. Carter, S. Ebrahimi, Z. Ke, S. H. W. Scheres, L. Bergamaschi, G. L. Grice, Y. Zhang, J. A. Nathan, S. Baker, L. C. James, H. E. Baxendale, I. Goodfellow, R. Doffinger, J. A. G. Briggs, A thermostable, closed SARS-CoV-2 spike protein trimer. *Nat. Struct. Mol. Biol.* (2020), doi:10.1038/s41594-020-0478-5.
35. R. Yan, Y. Zhang, Y. Li, L. Xia, Y. Guo, Q. Zhou, Structural basis for the recognition of SARS-CoV-2 by full-length human ACE2. *Science*. **367**, 1444–1448 (2020).
36. Q. Wang, Y. Zhang, L. Wu, S. Niu, C. Song, Z. Zhang, G. Lu, C. Qiao, Y. Hu, K.-Y. Yuen, Q. Wang, H. Zhou, J. Yan, J. Qi, Structural and Functional Basis of SARS-CoV-2 Entry by Using Human ACE2. *Cell*. **181**, 894-904.e9 (2020).
37. T. N. Starr, A. J. Greaney, A. Addetia, W. W. Hannon, M. C. Choudhary, A. S. Dingens, J. Z. Li, J. D. Bloom, Prospective mapping of viral mutations that escape antibodies used to treat COVID-19. *Science*. **371**, 850–854 (2021).
38. M. S. A. Gilman, P. Furmanova-Hollenstein, G. Pascual, A. B van 't Wout, J. P. M. Langedijk, J. S. McLellan, Transient opening of trimeric prefusion RSV F proteins. *Nat. Commun.* **10**, 2105 (2019).
39. A. A. Albertini, C. Mérigoux, S. Libersou, K. Madiona, S. Bressanelli, S. Roche, J. Lepault, R. Melki, P. Vachette, Y. Gaudin, Characterization of monomeric intermediates during VSV glycoprotein structural transition. *PLoS Pathog.* **8**, e1002556 (2012).
40. I. S. Kim, S. Jenni, M. L. Stanifer, E. Roth, S. P. J. Whelan, A. M. van Oijen, S. C. Harrison, Mechanism of membrane fusion induced by vesicular stomatitis virus G protein. *Proc. Natl. Acad. Sci. U. S. A.* **114**, E28–E36 (2017).
41. S. Bangaru, S. Lang, M. Schotsaert, H. A. Vanderven, X. Zhu, N. Kose, R. Bombardi, J. A. Finn, S. J. Kent, P. Gilchuk, I. Gilchuk, H. L. Turner, A. García-Sastre, S. Li, A. B. Ward, I. A. Wilson, J. E. Crowe Jr, A Site of Vulnerability on the Influenza Virus Hemagglutinin Head Domain Trimer Interface. *Cell*. **177**, 1136-1152.e18 (2019).
42. D. M. Eckert, P. S. Kim, Mechanisms of Viral Membrane Fusion and Its Inhibition. *Annu. Rev. Biochem.* **70**, 777–810 (2001).
43. J. R. Byrum, E. Waltari, O. Janson, S.-M. Guo, J. Folkesson, B. B. Chhun, J. Vinden, I. E. Ivanov, M. L. Forst, H. Li, A. G. Larson, W. Wu, C. M. Tato, K. M. McCutcheon, M. J. Peluso, T. J. Henrich, S. G. Deeks, M. Prakash, B. Greenhouse, J. E. Pak, S. B. Mehta, multiSero: open multiplex-ELISA platform for analyzing antibody responses to SARS-CoV-2 infection. *medRxiv* (2021), doi:10.1101/2021.05.07.21249238.
44. A. Glasgow, J. Glasgow, D. Limonta, P. Solomon, I. Lui, Y. Zhang, M. A. Nix, N. J. Rettko, S. Zha, R. Yamin, K. Kao, O. S. Rosenberg, J. V. Ravetch, A. P. Wiita, K. K. Leung, S. A. Lim, X. X. Zhou, T. C. Hobman, T. Kortemme, J. A.

Wells, Engineered ACE2 receptor traps potently neutralize SARS-CoV-2. *Proc. Natl. Acad. Sci. U. S. A.* (2020), doi:10.1073/pnas.2016093117.

Chapter 3:

Mutation and Cleavage Modulate Conformational Dynamics of SARS-CoV-2 Spike on Enveloped Virus-Like Particles

---

3.1 Introduction

SARS-CoV-2 has profoundly affected society since late 2019. This betacoronavirus infects host cells through its spike protein, which decorates the surface of the enveloped virus. The spike protein is responsible for recognizing the host cell receptor, angiotensin-converting enzyme 2 (ACE2) (*1*, *2*). Following cleavage at the S2' protease site by TMPRSS2 (*1*) or other host cell proteases (*3*), the spike protein undergoes dramatic conformational changes, ultimately leading to the fusion of the host and viral membranes and the release of the viral genetic material. As the largest surface protein on the virus with a crucial role in the infection process, the spike protein is the primary target for vaccines and therapeutics (*4*, *5*) .

The evolution of the SARS-CoV-2 spike protein has been marked by several crucial sequence alterations that have significantly impacted the virus's transmissibility and virulence. A key feature is the presence of a multibasic furin cleavage site at the S1/S2 junction, a distinctive characteristic of SARS-CoV-2 compared to other betacoronaviruses. This feature is believed to play a critical role in the virus's ability to jump from reservoir species to humans. The biological significance of these sites remains unclear, but has been suggested to determine tropism and pathogenesis (*6*). While other related coronaviruses have protease cleavage sites at the S1/S2 junction, they are often processed with low efficiency. For instance, Middle-Eastern respiratory syndrome (MERS) has a minimal furin cleavage site (R-X-X-R) (*7*), and SARS-CoV-1 has a single arginine at this junction (*3*, *8*). Notably, the SARS-CoV-2 spike furin cleavage site has an additional basic residue (R-R-A-R), making it more similar to the optimal furin cleavage site (R-X-R-R). Studies have shown that the S1/S2 junction of SARS-CoV-2 spike is cleaved more efficiently than that of SARS-CoV-1 spike (*3*). It is proposed that for the SARS-CoV-2 spike protein to be efficiently cleaved at the S2' protease site by TMPRSS2 on the host cell surface—triggering fusion—it must first be pre-processed by furin (*3*, *8*). To date, no molecular mechanism has been identified to explain how cleavage at the S1/S2 protease site enhances processing by TMPRSS2 at the S2' protease site. Moreover, the majority of soluble spike constructs as well as some vaccine constructs (*5*) have an ablated furin cleavage site, yet the impact of this deletion on the structure and antigenicity of these constructs remains unknown.

Another notable sequence change was the early emergence and fixation of the D614G mutation in the spike protein in the S1 subunit. Since December 2019, viral genomes have been collected and cataloged by numerous groups worldwide, allowing tracking of mutations throughout the pandemic. In January 2020, viral genomes

revealed a high frequency of the A23403G single nucleotide polymorphism, resulting in the change of an aspartic acid at position 614 to a glycine (D614G) in the spike protein (*9*, *10*). By June 2020, this mutation had reached near fixation globally (*9*, *10*). Substantial effort has been directed at understanding this mutation and why it imparts an evolutionary advantage to the virus. Studies in various cell types, using both authentic SARS-CoV-2 and viral pseudotypes, have shown that the G614 variant is 2- to 9-fold more infectious than D614 (*10*–*12*). However, experiments have shown that this advantage is not due to immune evasion, spike expression and processing, nor viral assembly (*10*–*13*). Several competing models have been proposed for why D614G provides a competitive advantage for the virus including reducing premature S1 dissociation from S2 (*12*, *14*) and increasing the proportion of RBDs in the up conformation (*10*). Given conflicting data, it remains unclear why this single mutation has a profound effect on virulence.

In addition to natural evolution, the spike protein has been engineered extensively to create more effective vaccine constructs and soluble versions of the trimer that can be used for *in vitro* experiments. One of the first engineered constructs is S-2P (*15*, *16*), in which the transmembrane helices are replaced with a synthetic trimerization domain (T4 fibritin or foldon), the multibasic furin cleavage site (R-R-A-R) is either substituted by G-S-A-S (*16*), is substituted to I-L-R with an additional deletion of the N-terminal N-S-P (*15*) or is replaced by a single alanine (*17*). Additionally, K986 and V987, which are at the S1 proximal end of the S2 domain in between HR1 and CH subdomains, are both mutated to proline. This engineering strategy was previously used to stabilize other class 1 viral fusion proteins, including respiratory syncytial virus (*18*) and Middle-Eastern respiratory syndrome (MERS) (*19*, *20*). These prolines prevent the reorganization of the S2 domain necessary for fusion, stabilizing the protein in its prefusion conformation (*19*). S-2P has led to crucial structural insights and facilitated the rapid development and deployment of vaccine constructs worldwide.

The engineering of soluble variants has enabled valuable biochemical studies on the spike protein, including antibody epitope mapping, affinity determination, and immunization studies, alongside further structure-based engineering. However, a detailed comparison of the structure of S-2P with membrane-bound spike variants and spike on infectious virus is lacking. This is largely due to the challenges and risks associated with working with live virus, the technical difficulties of conducting *in vitro* studies with non-soluble proteins, and the challenges of producing sufficient quantities of virus or pseudotyped virus needed for such studies. A deeper understanding of how these engineering efforts impact the structure and dynamics of the spike protein will enable more accurate interpretation of S-2P experiment results and help identify and address potential caveats.

There is no evidence to date to suggest that any of these changes, solubilization, K986P/V987P, removal of the multibasic furin site and the identity of the amino acid at

position 614 changes the overall fold of the spike protein. Much less is known about any changes to the conformational ensemble - dynamics and energetics - of the protein. Hydrogen-deuterium exchange monitored by mass spectrometry (HDX-MS) is a powerful experimental tool to evaluate the conformational landscape of proteins. The conformational dynamics of the spike protein have been evaluated using HDX-MS, molecular dynamics (*21*, *22*) and single-molecule Förster resonance energy transfer (smFRET) (*23*). Previous HDX-MS studies have been done on S-2P constructs as well as the isolated RBD and have been primarily used to map epitopes and evaluate the effect of receptor binding on the rest of the spike protein (*24–28*). HDX takes advantage of amide hydrogens being labile and exchanging with deuterons from the buffer made with heavy water (D_2O). The rate at which an individual amide exchanges depends on the stability of the hydrogen bond the amide is involved in, and thus reports on both solvent accessibility and local stability of secondary structural elements (*29*, *30*). By comparing the exchange of different SARS-CoV-2 spike constructs, we can determine how mutations and engineered features change the solvent accessibility, flexibility and stability of the spike protein.

In our previous work conducting HDX-MS on spike protein, we discovered that S-2P D614 undergoes a very slow ($t_{1/2}$ of hours) conformational change, wherein the trimer interface is no longer formed while each protomer remains well-folded (*31*). This conformational change is reversible and temperature-dependent, such that incubation at 4 °C promotes the formation of the “open-interface trimer,” while incubation at 37 °C returns the population to the canonical “closed-interface trimer” prefusion conformation. It is crucial to distinguish between this conformational change and the “up” and “down” states of each receptor-binding domain in the protein. While HDX-MS can report on the ensemble average of the RBD conformations, this conformational change is on the millisecond to second timescale (*23*) and thus is much faster than the conformational change between the prefusion and open-interface trimer. Given the labeling time of our experiments is minutes to hours, hydrogen exchange reports on the ensemble average of RBDs in the up and down position. All previous HDX-MS on full-length spike has been conducted with S-2P and other engineered soluble constructs.

Here we interrogate the conformational dynamics of spike protein in its native membrane environment by carrying out HDX on spike protein on engineered virus-like particles. We find that the multibasic furin site leads to a destabilization of the S2’ protease cleavage site as well as increases the proportion of open-interface trimer, which is compensated for by the D614G mutation. We further find that the trimerization domain and stabilizing prolines have a minimal effect on the fold and conformational landscape of the SARS-CoV-2 spike protein making them a faithful proxy for the membrane-bound, unstabilized spike protein.

3.2 Results

3.2.1 Hydrogen deuterium exchange of spike protein on enveloped virus-like particles

To study the spike protein in a more native-like environment, enveloped virus-like particles (eVLPs) were made as described before by genetically appending an endocytosis prevention motif (EPM) and ESCRT and ALIX-binding region (EABR) to the intracellular, c-terminal end of the full-length spike protein including the transmembrane helices (residues 1-2052) (*32*). This leads to the formation of extracellular vesicles that are densely coated with spike protein and are non-infectious and non-replicative and thus are compatible with HDX-MS without safety concerns of using pseudovirus or live SARS-CoV-2. Modifications were made to our previous spike protein HDX-MS protocol in order to remove phospholipids in the eVLPs to prevent clogging the columns in the liquid chromatography system. Despite the challenges of doing HDX-MS on a heavily glycosylated membrane protein in a complex mixture of other proteins in the eVLP, we identified and processed 200-250 unique peptides which resulted in 50-55% sequence coverage of the peptides shared between S-2P and the eVLP constructs with an average redundancy of 2.8. From continuous labeling HDX-MS experiments we have found that spike proteins displayed on eVLPs have exchange consistent with the soluble, prefusion stabilized S-2P construct and we do not see bimodal exchange that would suggest the presence of a significant population of post-fusion trimer.

Table 1

Construct	% Prefusion after 20 hours of incubation at 37 °C	Rate of opening at 4 °C (h^{-1})	Halftime of opening at 4 °C (h)
Soluble S-2P	84 ± 4	0.03 ± 0.003	23.7 ± 2.7
eVLP-KV-D614G-Fur	83 ± 9	0.02 ± 0.002	44.1 ± 6.8
eVLP-KV-D614G-ΔFur	89 ± 6	0.006 ± 0.003	117.5 ± 51.2
eVLP-KV-D614-Fur	50 ± 5	0.04 ± 0.009	17.3 ± 4.0
eVLP-KV-D614-ΔFur	89 ± 8	0.01 ± 0.002	58.0 ± 13.7
eVLP-2P-D614-ΔFur	95 ± 4	0.04 ± 0.004	16.7 ± 1.5
eVLP-2P-D614-Fur	28 ± 7	0.06 ± 0.02	12.2 ± 3.9

3.2.2 Unstabilized D614G SARS-CoV-2 spike samples the open trimer on an eVLP

Our previous paper on HDX-MS of S-2P revealed that in addition to the canonical prefusion conformation, the spike protein samples an open-interface trimer conformation that can be detected by bimodal HDX spectra, where the less exchanged distribution corresponds to the prefusion conformation and the more exchanged distribution corresponds to the open-interface trimer (Figure 1A). By fitting the bimodal spectra to two distributions, we can determine the relative populations of each state.

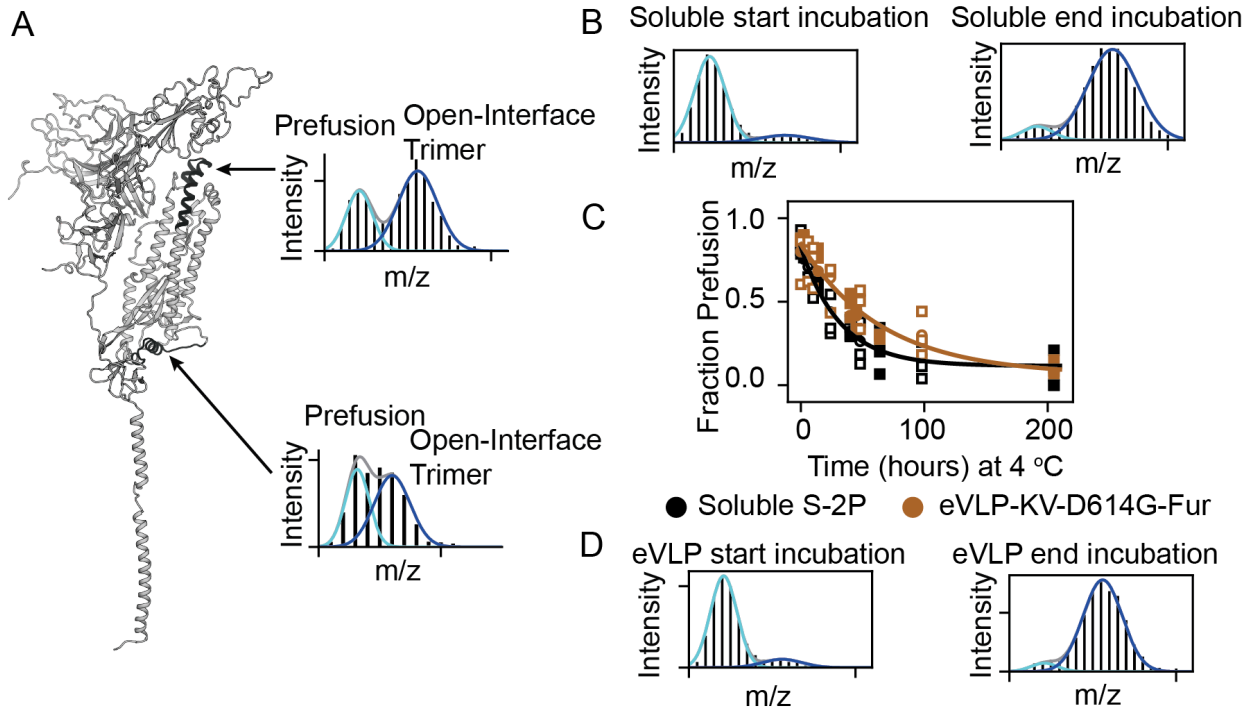

Figure 1 Monitoring the prefusion vs open-interface trimer conformational change
(A) Spike monomer ((22)), black regions are reporter regions used to determine conformation as they exchange differently in the two conformations and show bimodal behavior. Example spectra from the eVLP-KV-D614G-Fur from the top and bottom of S2 after 45 hours of incubation at 4 °C. The proportion of prefusion (cyan curve) and open-interface trimer (blue curve) is about the same for both regions. (B) Example spectra from the beginning (0h) and end (205h) of the soluble S-2P 4 °C incubation. (C) Time course of interconversion to open-interface trimer at 4 °C for soluble S-2P and eVLP-2P-D614-ΔFur (D) Example spectra from the beginning (0h) and end (205h) of the eVLP-KV-D614G-Fur 4 °C incubation.

To address the question of whether the wild-type SARS-CoV-2 spike sequence on a membrane can sample the open-interface trimer conformation, eVLPs without stabilizing prolines (K986 and V987) with D614G and an intact multibasic furin site (eVLP-KV-D614G-Fur) were expressed and purified. It was found that eVLP-KV-D614G-Fur shows bimodal spectra at the peptides previously shown to be

reporters on the conformation similar to what is seen for S-2P (Figure 1B-D). This confirms that the open-interface trimer conformation is indeed sampled by the wild-type SARS-CoV-2 spike sequence on a membrane. After incubating the purified eVLPs for 20 hours at 37 °C the bimodal spectra at the top of the S2 domain (peptides in the 978-1006 region) and the bottom of the S2 domain (peptides in the 892-916 region) reported that the eVLP-KV-D614G-Fur spike protein is 83 ± 9% closed trimer conformation (Table 1) while for S-2P the 37 °C equilibrium closed trimer population was 84 ± 4%. Similar to what was previously observed for soluble S-2P, incubation at 4 °C shifts the equilibrium to the open-interface trimer and we can measure the rate of interconversion (Figure 1C). It was found that the halftime of interconversion for eVLP-KV-D614G-Fur spike protein was 44 ± 6.8 hours while under the same conditions the halftime of interconversion for S-2P is 23.7 ± 2.7 hours (Table 1). Therefore the native spike sequence and environment raises the kinetic barrier of interconversion compared to S-2P while the equilibrium populations are relatively similar.

3.2.3 Cleavage at the furin site leads to destabilization of the S2' protease site

One of the notable differences between SARS-CoV-2 and other closely related coronaviruses was the existence of the multibasic furin site at the S1/S2 junction, which has been shown to increase the infectivity of the virus. We can determine the structural effect of furin cleavage by comparing the hydrogen exchange between eVLPs expressing constructs with K986/V987 and D614G with the multibasic furin site (R-R-A-R) and a construct with an ablated furin site (eVLP-KV-D614G-ΔFur). eVLPs with a multibasic furin site have nearly 100% cleavage as the S1/S2 furin site (*32*). In comparing the exchange, the majority of the peptides have very little difference in uptake between eVLP-KV-D614G-Fur and eVLP-KV-D614G-ΔFur with the notable exception of residues 783-822 which is more exchanged in the construct with the intact multibasic furin site (Figure 2A-C). This peptide contains the S2' cleavage site where TMPRSS2 cleaves and the fusion peptide. An increase in exchange indicates this area becomes more flexible when the S1/S2 junction is cleaved. This increased flexibility may increase TMPRSS2 activity at the S2' cleavage site as TMPRSS2 is a serine protease, which requires the substrate to be unstructured to bind and cleave.

The inclusion of the furin site does not significantly change the equilibrium populations of spike in the KV D614G background as the percent of closed-interface trimer after 20 hours of incubation at 37 °C was 89 ± 6% for eVLP-KV-D614G-ΔFur and 83 ± 9% for eVLP-KV-D614G-Fur; however, the inclusion of the furin site does lower the barrier of opening as the halftime of opening at 4 °C for eVLP-KV-D614G-ΔFur is 117.5 ± 51.2 hours while the halftime for eVLP-KV-D614G-Fur is 44.1 ± 6.8 hours (Figure 2D, Table 1).

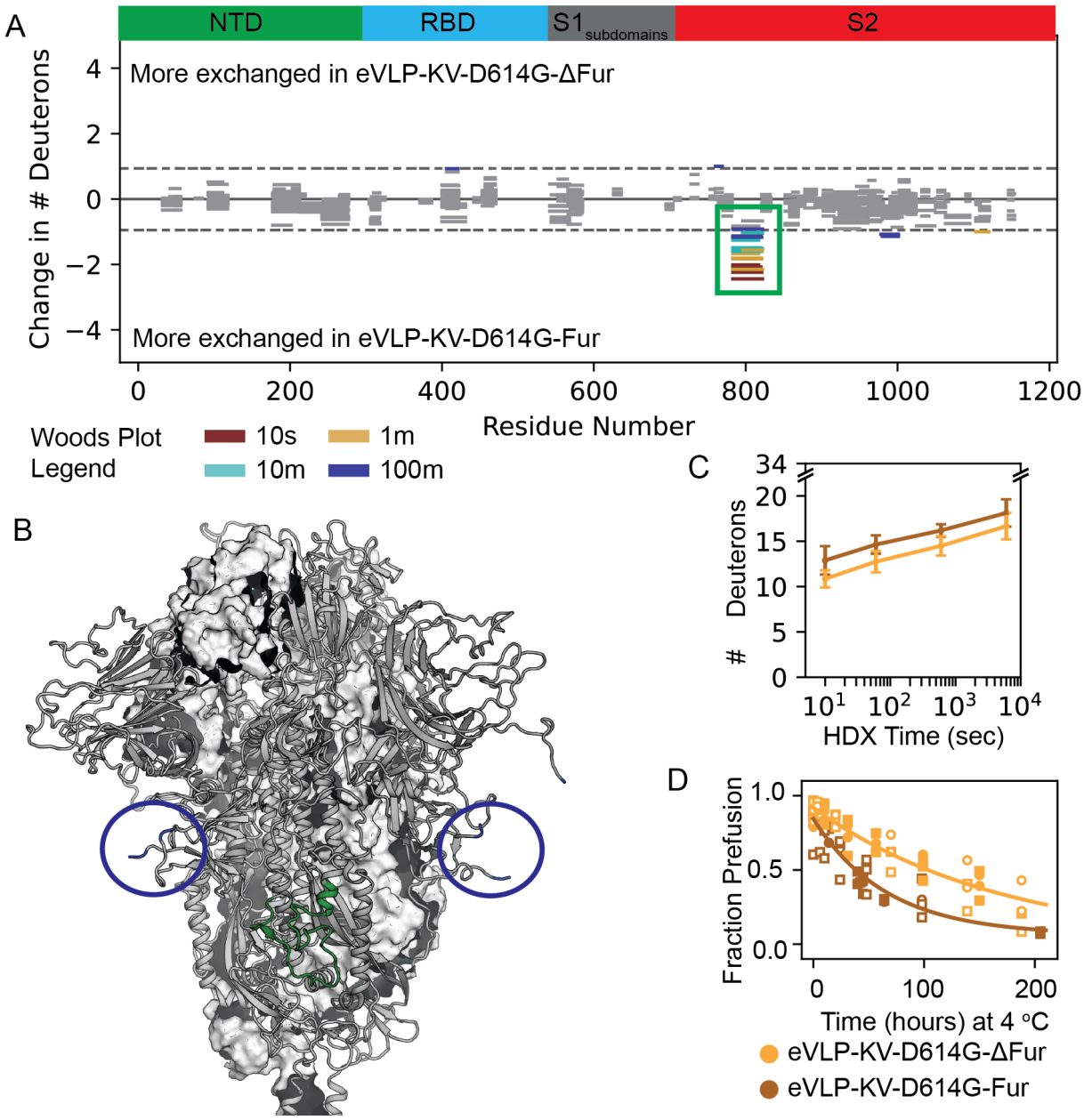

Figure 2 Comparison of eVLP-KV-D614G-Fur and eVLP-KV-D614G-ΔFur
(A) Woods plot of hydrogen exchange comparing eVLP-KV-D614G-Fur and eVLP-KV-D614G-ΔFur . Each line is a peptide, the x-axis position represents the sequence it covers and the y-axis position is the difference in exchange. The color of the line encodes the time of exchange. The black square is around the region showing significant differences in exchange. The exchange significance threshold was determined by the average variability of exchange within replicates of the same system and is represented by the grayed out peptides, which are below the threshold. (B) Structure of spike (*22*) with the peptide showing a significant difference in exchange in green. The location of the S1/S2 furin cleavage site is circled and colored in blue. (C) Uptake plot for the peptide designated in A. (D) Kinetics of conformational interconversion at 4 °C for eVLP-KV-D614G-Fur and eVLP-KV-D614G-ΔFur.

3.2.4 G614 stabilizes the closed trimer conformation compared to D614 in the presence of the multibasic furin site

We next investigated the role of the D614G mutation by comparing eVLP constructs with the D614 to eVLPs with G614. Position 614 is located in the S1 domain facing the S2 domain (Figure 3B). In the presence of the multibasic furin site, it was found that D614G dramatically stabilizes the prefusion conformation. After 20 hours of incubation at 37 °C, the percent prefusion is 83 ± 9% for eVLP-KV-D614G-Fur while it is only 50 ± 5% for eVLP-KV-D614-Fur (Table 1). In the absence of the furin site, D614G did not have an effect on the equilibrium percentage of prefusion conformation which was 89 ± 8% for eVLP-KV-D614-ΔFur compared to 90 ± 6% in eVLP-KV-D614G-ΔFur. This indicates that D614G stabilizes the closed interface trimer in comparison to constructs with D614 but only in the presence of the multibasic furin site. D614G also raises the barrier of opening approximately two-fold in the presence and absence of the multibasic furin site (Figure 3D, Table 1).

Given the dramatic difference in equilibrium populations between constructs with D614 and D614G with an intact furin site, we cannot fairly compare continuous labeling of eVLP-KV-D614-Fur and eVLP-KV-D614G-Fur. However, we can determine the effect of the D614G mutation on folding and local stability in the absence of furin by comparing the continuous labeling of eVLP-KV-D614-ΔFur to eVLP-KV-D614G-ΔFur. We found that the only region with a significant difference in exchange is again in peptides spanning the S2' cleavage site and fusion peptide; these peptides are more exchanged in the D614G construct (Figure 3A-C). This suggests that the evolution of the D614G mutation further resulted in a loosening of the S2' protease site.

3.2.5 Spike samples the open-interface trimer in the presence and absence of the stabilizing prolines.

Soluble S-2P as well as many vaccine constructs (*5*) include two mutations to proline (K986P and V987P) in a loop between HR1 and the central helix which has been shown in other class one fusion proteins to prevent spontaneous, irreversible adoption of the post-fusion conformation. To directly compare the effect of the proline mutations on both the formation of the open-interface trimer as well as the overall structure of the protein we compared eVLPs displaying spike with D614 with an ablated furin site either with the native KV (eVLP-KV-D614-ΔFur) or with the proline mutations (eVLP-2P-D614-ΔFur). It was found that mutation to proline had very little effect on the equilibrium population of prefusion conformation at 37 °C, 89 ± 8% for eVLP-KV-D614-ΔFur compared to 95 ± 4% eVLP-2P-D614-ΔFur (Table 1). The mutation from the native residues to prolines does lower the barrier to opening at 4 °C as eVLP-2P-D614-ΔFur was found to have an opening halftime of 16.7 ± 1.5 h, which is approximately 4 times faster than the opening time of eVLP-KV-D614-ΔFur (Figure 4D,

Table 1). This suggests that while the proline mutations may disrupt the interface in

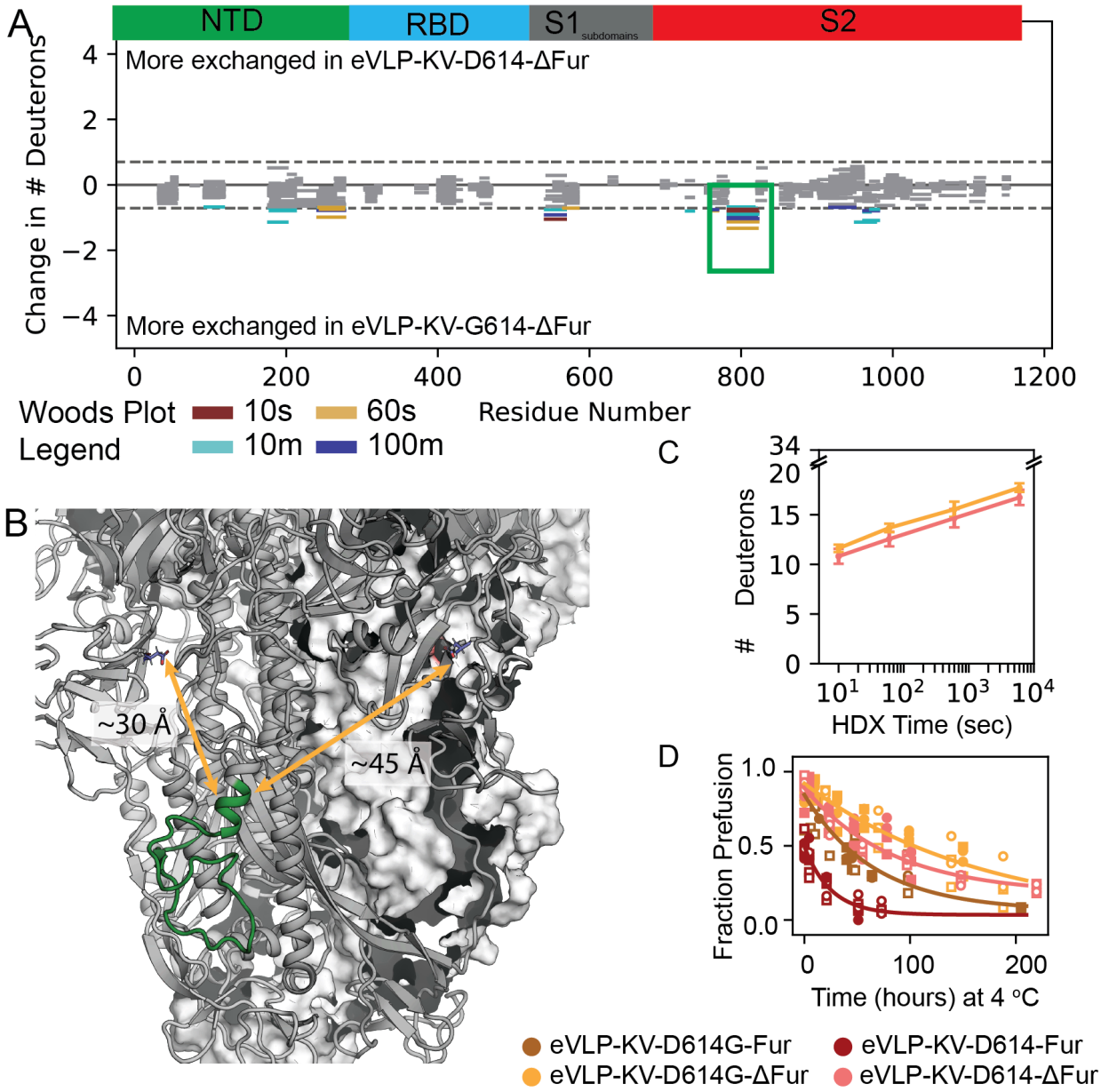

Figure 3 Comparison of eVLP-KV-D614-ΔFur and eVLP-KV-D614G-ΔFur
(A) Woods plot of hydrogen exchange comparing eVLP-KV-D614-ΔFur and eVLP-KV-D614G-ΔFur . Each line is a peptide, the x-axis position represents the sequence it covers and the y-axis position is the difference in exchange. The color of the line encodes the time of exchange. The black square is around the region showing significant differences in exchange. The exchange significance threshold was determined by the average variability of exchange within replicates of the same system and is represented by the grayed out peptides, which are below the threshold. (B) Structure of spike (*22*) with the peptide showing a significant difference in exchange in green. The location of D614 is shown on the same monomer and the adjacent monomer in blue sticks. The distance between the peptide of interest is indicated with the orange arrows. (C) Uptake plot for the peptide designated in A. (D) Kinetics of conformational interconversion at 4 °C for eVLP-KV-D614-ΔFur, eVLP-KV-D614G-ΔFur, eVLP-KV-D614-Fur and eVLP-KV-D614G-Fur.

such a way that favors opening, the overall behavior is not unique to proteins with the native residues or proline mutations.

Due to the hypothesis that spike requires proline mutations in order to remain in the prefusion conformation, there is little structural information regarding the effect of these mutations. When expressed on eVLPs, continuous labeling experiments show no large differences in exchange between eVLP-KV-D614-ΔFur and eVLP-2P-D614-ΔFur (Figure 4A). There is a small yet significant difference in peptides covering the c-terminal end of HR1 and the loop before the central helix (Figure 4B-C), which is more protected in the eVLP-KV-D614-ΔFur. This region is proximal to the site of the proline mutations and thus the decrease in exchange could be due to an increase in flexibility of this region when the prolines lead to restriction on the backbone (Figure 4C).

3.2.6 The membrane environment stabilizes the spike protein but does not change the fold

In order to make soluble spike variants including S-2P, the transmembrane helices were replaced by a T4 fibritin trimerization domain. This trimerization domain has been shown to be an acceptable geometry for the spike protein to form the proper contacts; however, given the geometry could be different we hypothesized that the formation of the open-interface trimer may be affected by the solubilization. To address this question, we can compare S-2P to a sequence matched construct minus the trimerization domain with the transmembrane domain and eVLP tags (eVLP-2P-D614-ΔFur). After incubating eVLP-2P-D614-ΔFur at 37 °C for 20 hours the spike protein was approximately 95 ± 4% prefusion conformation, compared to 84 ± 4% in the soluble S-2P construct after thawing from a frozen aliquot and incubated at 37 °C for 20 hours (Figure 5A, Table 1). This suggests that the membrane slightly stabilizes the closed trimer conformation relative to the soluble matched construct. Under the current conditions, we found the rate of opening for soluble S-2P and eVLP-2P-D614-ΔFur S protein have a similar rate of opening at 4 °C (Table 1, Figure 5A).

To determine if the T4 fibritin trimerization domain and resulting solubilization changes the hydrogen exchange pattern of the spike protein compared to a more native membrane environment, we conducted continuous labeling HDX on S-2P and a sequence matched eVLP (eVLP-2P-D614-ΔFur). It was found that the hydrogen exchange uptake pattern is similar in both soluble S-2P and eVLP-2P-D614-ΔFur except that in most peptides S-2P is more exchanged than eVLP-2P-D614-ΔFur (Figure 5B). This suggests that eVLP-2P-D614-ΔFur is more stable than S-2P throughout most of the protein. One notable area of the protein where increased exchange is seen in soluble S-2P is along the central helix (CH), suggesting global destabilization of the

protein. Overall, the consistent shape of uptake plots between S-2P and

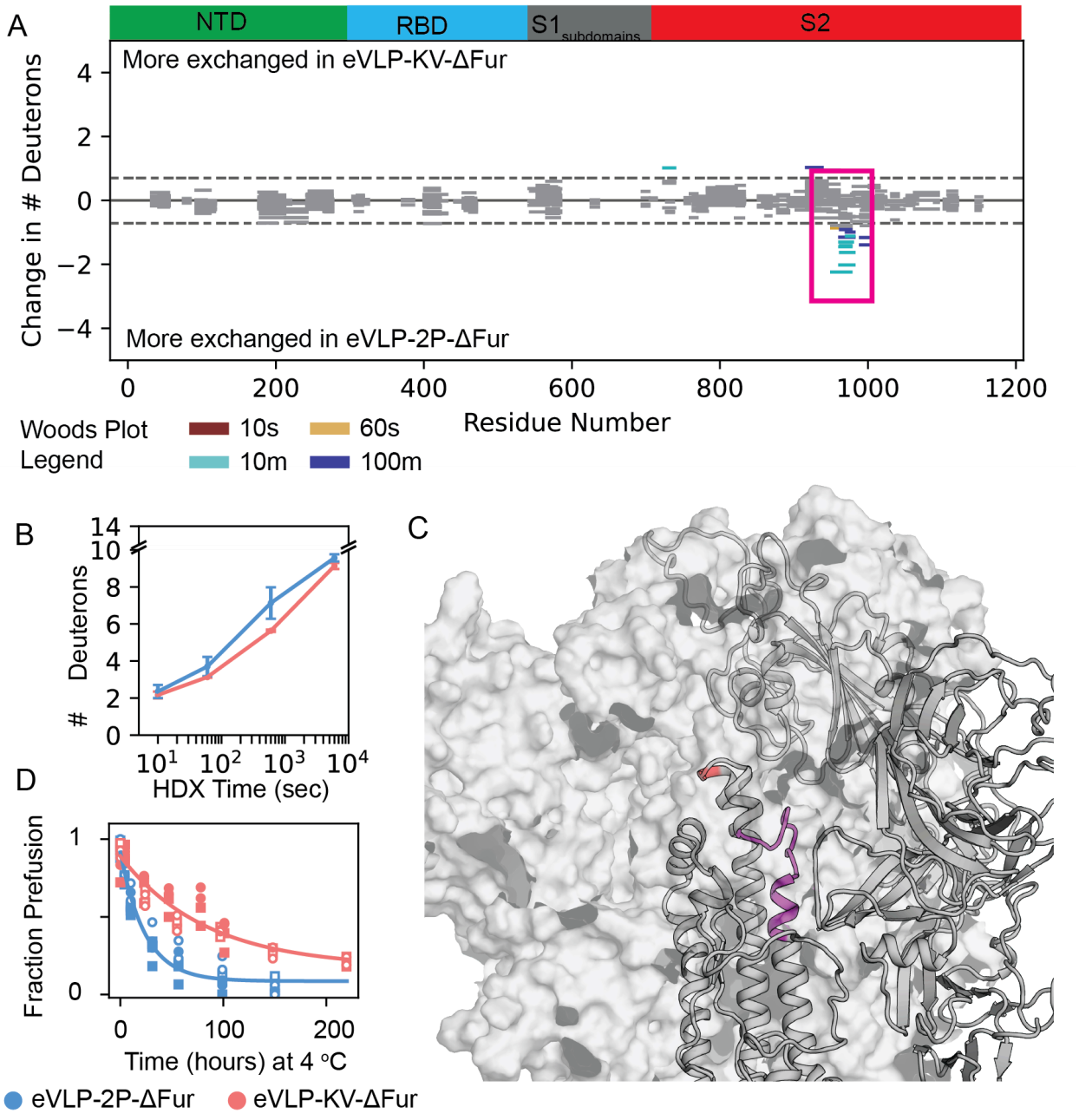

Figure 4 Comparing stabilizing prolines to native K986 and V987
(A) Woods plot of hydrogen exchange comparing eVLP-2P-D614-ΔFur and eVLP-KV-D614-ΔFur. Each line is a peptide, the x-axis position represents the sequence it covers and the y-axis position is the difference in exchange. The color of the line encodes the time of exchange. The one region of different exchange is in the black square. (B) Uptake plot of the region designated in the woods plot. The exchange significance threshold was determined by the average variability of exchange within replicates of the same system and is represented by the grayed out peptides, which are below the threshold. (C) The location of the peptide designated in the woods plot and the uptake plot is shown in purple. K986/V987 are shown in red. (D) Time course of conformation interconversion at 4 °C for eVLP-2P-D614-ΔFur and eVLP-KV-D614-ΔFur.

eVLP-2P-D614-ΔFur suggests that the two constructs are folded similarly; the differences in exchange suggest a small difference in local stability throughout the protein (Figure 5C).

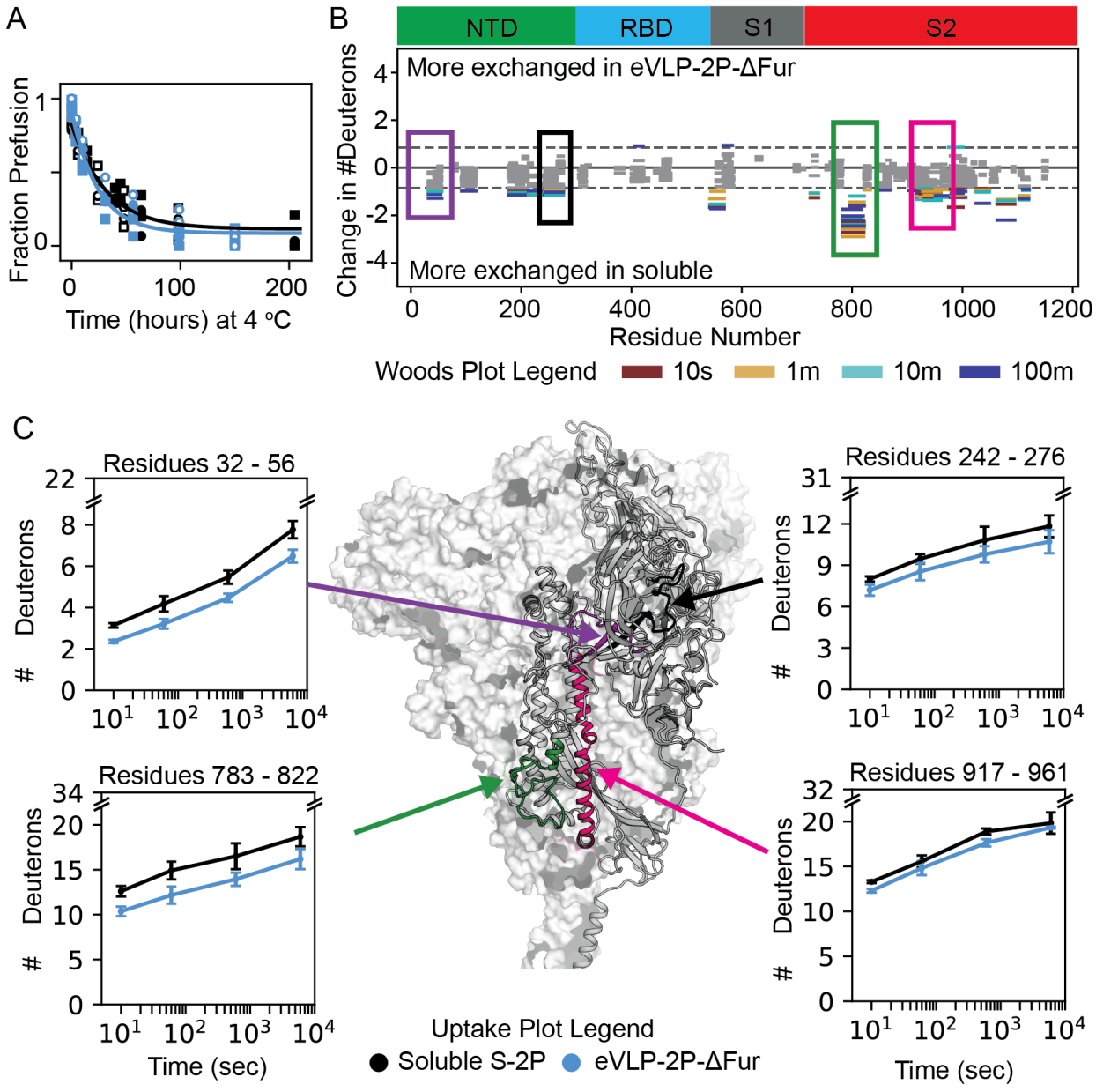

Figure 5 Comparison of soluble S-2P and eVLP-2P-D614-ΔFur (A) Kinetics of conversion to the open-interface trimer at 4 °C of soluble S-2P and eVLP-2P-D614-ΔFur spike. (B) Woods plot comparing deuterium uptake between soluble S-2P and eVLP-2P-D614-ΔFur. Each line is a peptide whose x-axis value and length represents its sequence position and the y-axis value is the difference in the exchange. The color of the line represents the deuteration time. The exchange significance

threshold was determined by the average variability of exchange within replicates of the same system and is represented by the grayed out peptides, which are below the threshold. The boxed peptides are selected for illustrative purposes and the corresponding uptake plot is shown in parts (C) and the location of these peptides is shown on structure (*22*).

3.3 Discussion

3.3.1 Implications for viral evolution

The biggest change that we see in terms of local flexibility is an increase in flexibility S2' protease site and fusion peptide region in the furin-cleaved construct when comparing eVLP-KV-D614G-Fur to eVLP-KV-D614G-ΔFur. Previous structural analysis comparing a cleaved and uncleaved construct did not note any structural changes to this region in the presence of cleavage and only noted modest reorientation of S1 subdomains (*13*). It is important to note that this change cannot be accounted for by an increase in solvent accessibility after cleavage of the S1/S2 junction as the location of both neighboring sites is over 30 Å away (Figure 6 B). This observed disordering of the S2' site may explain the evolutionary advantage of the multibasic furin cleavage site at S1/S2 as this allosteric disordering could make it easier for the S2' site to be processed by TMPRSS2, a serine protease, which requires a disordered stretch of amino acids to bind to in order to cleave. To our knowledge, this is the first molecular explanation for why furin cleavage is advantageous to the virus.

In considering the implications of our hydrogen exchange data on our understanding of the role of the early-adopted D614G mutation in enhancing virulence, our results do not indicate that this variant significantly alters the structure of the SARS-CoV-2 spike protein. Most structural studies align with this conclusion, though some suggest the mutation induces rotations of S1 subdomains (*10*, *13*), an increase in secondary structure of the 640 loop in S1 (*14*), as well as altering RBD dynamics.(*13*). Our HDX data does show some small, yet statistically significant, changes in uptake in regions in S1 and HR1 that could reflect the changes noted in structures (*10*, *14*). There also could be changes in regions that we do not have peptide coverage of. Combining the results of cryo-EM, which would report on large changes in structure, and HDX, which can report on small structural changes, it seems clear that the advantage conferred by D614G is likely not due to a dramatic structural change in spike.

Our data does suggest that the D614G mutation significantly stabilizes the canonical prefusion trimer conformation relative to the open-interface trimer particularly in furin-cleaved constructs, as evidenced by higher 37 °C equilibrium population of prefusion in eVLP-KV-D614G-Fur compared to eVLP-KV-D614-Fur. While a conformational change with a halftime of tens of hours to days is unlikely to represent a conformational change occurring during the infection process, a change in this rate instead suggests a change to the propensity of the trimer interface to lose trimeric contacts. If a trimer is more prone to losing trimeric contacts, it may increase the rate of S1 shedding as dissociation from S2 would require dissociation from both intra- and

inter protomer contacts. If too much S1 is shed before the virus has recognized the host-cell, the virus would be rendered non-infectious. Therefore the competitive advantage D614G may confer to the virus is strengthening trimeric contacts, as is seen by the decrease in trimer opening rate, which in turn may prevent premature S1 shedding.

The combination of D614G and the furin cleavage site suggests a pathway where the virus evolved the multibasic furin cleavage site at S1/S2, facilitating easier processing of the S2' site by TMPRSS2. However, this also inadvertently reduced trimer stability, increasing premature S1 shedding. The D614G mutation then evolved in response to this premature S1 shedding, stabilizing the trimer and resulting in a more infectious virus.

3.3.2 Implications for engineering and therapeutics

By examining the hydrogen exchange behavior and the propensity of different engineered SARS-CoV-2 protein constructs to adopt the open-interface trimer, we can better understand the impact of these mutations on the structure and dynamics of the protein. Overall the stabilizing proline mutations and trimerization domain did not have a big effect on the equilibrium populations or kinetics of opening at 4 °C. This indicates that the propensity to lose trimeric constructs, exposing the trimeric interface to solvent, is inherent in the protein and is not a consequence of engineering. In fact, the only variable that seems to have a dramatic effect was abolishing the native multibasic furin cleavage site which resulted in an decrease in the open-interface trimer equilibrium population at 37 °C in all constructs except those with D614G. This suggests that on a bonafide virus this conformation is likely sampled at least in a small population.

From the continuous labeling experiments, it was found that the overall fold and structure of the spike protein is not dramatically different as a result from engineered mutations as the uptake curve shapes are similar throughout the entire protein. Instead the data suggest that some of the engineered mutations had effects on the local stability. In the case of replacing the transmembrane helices with the trimerization domain, the entire protein is slightly destabilized suggesting the trimerization domain may constrict the geometry in such a way that the protein is destabilized. On a much smaller scale the K986P/V987P results in a destabilization of the c-terminus of the HR1 helix, which is proximal to the mutation, but does not seem to have an effect on the global stability or fold elsewhere. Finally in the case of both the D614/G614 comparison and the Furin/ΔFurin comparison, we see differences in local stability in regions that are not near the site of mutation but are also not widespread throughout the protein (which would suggest an affect on global stability), instead there is a change in uptake in the S2’/fusion peptide region, suggesting these mutations have an allosteric effect on the flexibility of these areas.

It is difficult to deduce the effect that these reported changes in SARS-CoV-2 spike constructs may have on the antigenicity of vaccine constructs as well the affinity of antibodies. In general small changes in local stability of the antigen could have an effect on the affinity of an antibody that was raised against one construct attempting to bind to another, but these effects are hard to predict. However, the most antigenically important regions of the SARS-CoV-2 spike protein are thought to be the NTD and RBD and except for the case of the S-2P/eVLP-2P-D614-ΔFur comparison, none of the differences noted are in these regions. However, there are neutralizing antibodies that target the fusion peptide of the SARS-CoV-2 peptide (*33*), where we do see a difference in exchange between constructs with and without furin cleavage and with D614 versus D614G. Given the increase in flexibility of this region in the presence of furin cleavage at the S1/S2 junction, the affinity of antibodies could be different to constructs with an ablated furin site compared to one with a cleavable furin site. Interestingly, to determine the affinity of fusion peptide targeting antibodies, they used an S-2P construct that had an intact furin site, suggesting that to measure tight binding furin cleavage was necessary. They further reported that binding was much tighter to an isolated S2 construct, suggesting that an increase in dynamics of this region leads to tighter binding. This is one example of how a change in dynamics can affect antibody binding and thus is an important consideration when evaluating affinity.

3.4 Conclusion

HDX-MS of eVLPs has significantly advanced our ability to study viral fusion proteins in environments that closely mimic their native state. This approach has provided critical structural insights into viral evolution and infectivity while also illuminating how engineering modifies the local dynamics of spike proteins. The potential of HDX-MS paired with eVLPs to revolutionize the study of viral fusion and other membrane proteins is immense. Membrane protein research has long been hampered by the challenges of expression, purification, and the use of detergents, which can distort their conformational landscapes compared to native lipid environments (*34–36*). By embedding proteins within eVLPs, we achieve a setting that closely resembles the natural viral membrane. Moreover, eVLPs offer substantial safety advantages due to their lack of genetic material and enable significantly higher protein concentrations than alternative methods like pseudoviruses. These benefits position eVLPs as a superior platform for HDX-MS studies. Looking ahead, the integration of eVLPs with HDX-MS holds enormous potential for deepening our understanding of viral fusion proteins and other membrane proteins, shedding light on the structural and energetic impacts of evolutionary and engineered mutations.

3.4 Methods

3.4.1 Protein expression and purification

SARS-CoV-2 Spike (S-2P) and RBD were expressed and purified from stably transformed Expi293 cells, following methods as described (*37*). Briefly, stable Expi293 suspension cells were maintained in Expi293 media at 37 °C. Cells were grown for 6 days, then harvested by centrifugation, and filtered. Supernatant was adjusted to pH 7.4 and loaded onto a 5 mL HisTrap Excel column and washed with 60 CV of buffer. Captured proteins were eluted with 10 CV of (20 mM sodium phosphate, 500 mM NaCl, 500 mM imidazole, pH 7.4). Eluted proteins were buffer exchanged into PBS using 100 kDa MWCO Amicon concentrators and filtered prior to storage at -80°C.

3.4.2 Spike eVLP Cloning, Expression and Purification

Full length SARS-CoV-2 spike protein constructs were cloned into a p3BNC plasmid containing the ALIX and EABR tags described in (*32*). Mutations (D614/D614G, ΔFur) were introduced via “around the horn” PCR. The ΔFur mutation was made by replacing the R-R-A-R residues with a single alanine (*17*). The resulting plasmid was transformed into MachOne E.coli $RbCl_2$ chemically competent cells via heatshock and plated onto ampicillin LB plates. A 100 mL overnight culture was then inoculated with a colony from the selection plate or a stab from a glycerol stock from a previous overnight culture. The culture was then prepped with a Qiagen maxi-prep kit to get plasmid at 500-2000 ng/uL.

Expi 293 Freestyle cells were prepared in various culture sizes (50-150 mL) at 2.5e6 cells/mL in FreeStyle™ 293 Expression Medium (Gibco, ThermoFisher). To transfect cells, 1 ug DNA per milliliter of cell culture was filtered with 300 uL of OptiMEM media. This was then diluted to 25 ug/mL in OptiMEM. In a separate tube 4 ug of PEI Max (Kyfora Bio) was prepared in 0.4 mL of OptiMEM for every 1 mL of cell culture and mixed well. The DNA mixture was then added to the PEI Max mixture and allowed to complex for 15 minutes before adding dropwise to the cell culture while swirling the flask. The cells were allowed to express for 65-70 hours at 37 °C 8% CO2 before harvesting by spinning down the cells at 4000xg for 15 minutes and collecting the supernatant.

To purify eVLPS, the collected supernatant was passed through a 0.2 um filter and then was set up for sucrose gradient centrifugation. Optiseal 29.9 mL ultracentrifuge tubes (Beckman Coulter) were filled with 25 mL of filtered supernatant and then 4.9 mL of 20% sucrose PBS was layered at the bottom of the tube. The tubes were balanced, capped and then spun in an MLA50 rotor in a 10 °C Optima MAX-XP for 2 hours at 48,000 rpm (rcf average = 150,700). The tubes were then emptied and the tubes were cut in half at an angle. 250 uL of 1X PBS was added to the pellet and then the cut tube was covered with parafilm. The pellet was then allowed to incubate overnight at room temperature before pipetting up and down to resuspend. The resuspended pellets of the same construct were combined and incubated at 37 °C for

15 minutes in an eppendorf tube. The tubes were then spun down at 11,000xg in a tabletop centrifuge for 2 minutes and the supernatant was collected. This was repeated 4 times to remove insoluble aggregates. The final supernatant was then flowed over an S200 sizing column to desalt the eVLPS (coming out in the void volume) from soluble protein (coming out later in the column). The void fraction was then pooled and concentrated to 20 uL for every 25 mL of culture. The eVLPs were then either used immediately for experiments or were flash frozen in liquid nitrogen and stored at -80 °C.

3.4.3 Continuous Labelling HDX-MS

To initiate exchange, concentrated eVLPs or 1.67 uM soluble S-2P spike trimer was diluted 10-fold to 1X PBS deuterated buffer (made by lyophilizing 1X PBS (Sigma-Aldrich P4417) and resuspending the powder with D_2O (TCI-America Cat No: W0002)) at pH_{read} 7.4. At each timepoint, exchange was quenched by mixing 100 uL of exchange reaction with 100 uL of ice-cold 2X offline digestion quench buffer containing zirconium oxide (3M Urea 20 mM TCEP pH 2.4 with 25 mg/ml Zirconium oxide) and adding 2 uL of a mixture of aspergillopepsin (Sigma-Aldrich P2143) and porcine pepsin (Sigma-Aldrich P6887) (3.5 mg/mL aspergillopepsin, 5 mg/mL porcine pepsin). The mixture was vortexed for 3 seconds before incubating on ice for 1 minute, incubating on ice for another minute for a total quench time of 2 minutes. The mixture was put into a Costar SpinX 0.22 um filter (Corning P/N: 8160) and spun at 6000 xg for 30 seconds. The filtered sample was then moved to a clean tube and flash frozen in liquid nitrogen. Samples were stored at -80 °C until LC-MS.

3.4.4 Incubation kinetics and pulse labeling

For evaluating the temperature dependent kinetics of interconversion, concentrated eVLPs or 1.67 μm soluble spike trimer were incubated at 37 °C for 20 hours. Samples were then moved to a temperature-controlled chamber at 4 °C and the population of each state was evaluated at the specified time points. To evaluate the relative population of the A and B conformer at each time point, 10 μL of spike sample was removed from the incubation tube and mixed with 90 μL of room temperature deuterated buffer. After a one-minute labeling pulse, 100 μL of quench buffer (3M Urea 20 mM TCEP pH 2.4 with 25 mg/ml Zirconium oxide) kept on ice was mixed with the 100 μL of labeled protein. To digest the protein, 2 uL of a mixture of aspergillopepsin (Sigma-Aldrich P2143) and porcine pepsin (Sigma-Aldrich P6887) (3.5 mg/mL aspergillopepsin, 5 mg/mL porcine pepsin) was added to the mixture. The mixture was vortexed for 3 seconds before incubating on ice for 1 minute, incubating on ice for another minute for a total quench time of 2 minutes. The mixture was put into a Costar SpinX 0.22 um filter (Corning P/N: 8160) and spun at 6000 xg for 30 seconds. The filtered sample was then moved to a clean tube and flash frozen in liquid nitrogen. Samples were stored at -80 °C until LC-MS..

3.4.5 Liquid chromatography - mass spectrometry.

All samples were thawed immediately before injection into a cooled valve system (Trajan LEAP) coupled to a LC (Thermo UltiMate 3000). Sample time points were injected in random order. The temperature of the valve chamber, trap column, and analytical column were maintained at 2 °C. Peptides were desalted for 4 minutes on a hand-packed trap column (Thermo Scientific POROS R2 reversed-phase resin 1112906, 1 mm ID x 2 cm, IDEX C-128) at 200 µL/min. Peptides were then separated with a C18 analytical column (ACQUITY UPLC BEH C18 Column, 130Å, 1.7 µm, 1 mm X 50 mm) and a gradient of 5-40% buffer B (100% Acetonitrile, 0.1% Formic Acid) at a flow rate of 40 µL/min over 14 minutes, and then of 40-90% buffer B over 30 seconds. The analytical and trap columns were then subjected to a sawtooth wash and equilibrated at 5% buffer B prior to the next injection. Protease columns were washed with two injections of 100 µL 1.6 M GdmCl, 0.1% formic acid prior to the next injection. Peptides were eluted directly into a Q Exactive Orbitrap Mass Spectrometer operating in positive mode (resolution 70000, AGC target 3e6, maximum IT 50 ms, scan range 300-1500 m/z). For each spike construct, a tandem mass spectrometry experiment was performed (Full MS settings the same as above, dd-MS2 settings as follows: resolution 17500, AGC target 2e5, maximum IT 100 ms, loop count 10, isolation window 2.0 m/z, NCE 28, charge state 1 and ≥7 excluded, dynamic exclusion of 15 seconds) on undeuterated samples.

3.4.6 Peptide identification

Byonic (Protein Metrics) was used to identify unmodified and glycosylated peptides in the tandem mass spectrometry data. The sequence of the expressed construct, including signal sequence and trimerization domain, was used as the search library. Sample digestion parameters were set to non-specific. Precursor mass tolerance and fragment mass tolerance was set to 6 and 10 ppm respectively. Variable N-linked glycosylation was allowed, with a library of human N-glycans. Peptide lists (sequence, charge state, and retention time) were exported from Byonic and imported into HDExaminer 3 (Sierra Analytics). When multiple peptide lists were obtained, all were imported and combined in HDExaminer 3.

3.4.7 HDExaminer3 analysis

Peptide isotope distributions at each exchange time point were fit in HDExaminer 3.2. For glycosylated peptides, only the highest confidence modification was included in the mass spectra search and analysis. Deuteration levels were determined by subtracting mass centroids of deuterated peptides from non-deuterated peptides. Care was taken to adjust the retention time window for each peptide, so that an even slice of the elution peak was taken and was the same width in all conditions to avoid deuteration elution bias. Woods plot significance was calculated in HDExaminer by determining the

average variation of deuteration amongst three replicates. Peptides discussed in the manuscript all had timepoints that were greater than the calculated significance threshold and were determined to have a p-value < 0.05, as visualized on a volcano plot.

3.4.8 Bimodal fitting and conformation quantification

The quantification of each conformation was conducted as described before (*31*). To reiterate, peptide mass spectra for bimodal peptides were exported from HDExaminer 3.0. All quantitative analysis of the exported peptide mass spectra was performed using python scripts in Jupyter notebooks. After importing a peptide mass spectra, the m/z range containing all possible deuteration states of the selected peptide was isolated and the find_peaks method from the scipy.signal package was used to identify each isotope in the mass envelope and the height of each peak was used as its intensity. The area of the total mass envelope was normalized to account for run-to-run differences in intensity. The bimodal mass envelopes for all timepoints under the same condition were globally fit to a sum of two gaussians, keeping the center and width of each gaussian constant across all incubation time points. Fitting was done using the curve_fit function from the scipy.optimize package. After fitting, the area under each individual gaussian was determined to approximate the relative population of each state. Two peptides from the top of S2 (residues 878-1010) and two peptides from the bottom of S2 (residues 878-925) were processed for each timepoint and then all points were plotted against time and fit to a single exponential. The error of the fitted rate was determined from the covariance of the fitted parameters and then was propagated to determine the error on the halftime. To determine the population of prefusion after 20 hours of incubation at 37 °C the prefusion conformation from all four peptides (two from top of S2 and two from bottom of S2) at the zero hour time point of the 4 °C incubation were averaged together

3.5 References

1. M. Hoffmann, H. Kleine-Weber, S. Schroeder, N. Krüger, T. Herrler, S. Erichsen, T. S. Schiergens, G. Herrler, N.-H. Wu, A. Nitsche, M. A. Müller, C. Drosten, S. Pöhlmann, SARS-CoV-2 Cell Entry Depends on ACE2 and TMPRSS2 and Is Blocked by a Clinically Proven Protease Inhibitor. *Cell* **181**, 271-280.e8 (2020).
2. P. Zhou, X.-L. Yang, X.-G. Wang, B. Hu, L. Zhang, W. Zhang, H.-R. Si, Y. Zhu, B. Li, C.-L. Huang, H.-D. Chen, J. Chen, Y. Luo, H. Guo, R.-D. Jiang, M.-Q. Liu, Y. Chen, X.-R. Shen, X. Wang, X.-S. Zheng, K. Zhao, Q.-J. Chen, F. Deng, L.-L. Liu, B. Yan, F.-X. Zhan, Y.-Y. Wang, G.-F. Xiao, Z.-L. Shi, A pneumonia outbreak associated with a new coronavirus of probable bat origin. *Nature* **579**, 270–273 (2020).
3. G. Papa, D. L. Mallery, A. Albecka, L. G. Welch, J. Cattin-Ortolá, J. Luptak, D. Paul, H. T. McMahon, I. G. Goodfellow, A. Carter, S. Munro, L. C. James, Furin cleavage of SARS-CoV-2 Spike promotes but is not essential for infection and cell-cell fusion. *PLOS Pathog.* **17**, e1009246 (2021).
4. D. Focosi, S. McConnell, A. Casadevall, E. Cappello, G. Valdiserra, M. Tuccori, Monoclonal antibody therapies against SARS-CoV-2. *Lancet Infect. Dis.* **22**, e311–e326 (2022).
5. F. X. Heinz, K. Stiasny, Distinguishing features of current COVID-19 vaccines: knowns and unknowns of antigen presentation and modes of action. *Npj Vaccines* **6**, 1–13 (2021).
6. J. K. Millet, G. R. Whittaker, Host cell proteases: Critical determinants of coronavirus tropism and pathogenesis. *Virus Res.* **202**, 120–134 (2015).
7. J. K. Millet, G. R. Whittaker, Host cell entry of Middle East respiratory syndrome coronavirus after two-step, furin-mediated activation of the spike protein. *Proc. Natl. Acad. Sci.* **111**, 15214–15219 (2014).
8. M. Hoffmann, H. Kleine-Weber, S. Pöhlmann, A Multibasic Cleavage Site in the Spike Protein of SARS-CoV-2 Is Essential for Infection of Human Lung Cells. *Mol. Cell* **78**, 779-784.e5 (2020).
9. B. Korber, W. M. Fischer, S. Gnanakaran, H. Yoon, J. Theiler, W. Abfalterer, N. Hengartner, E. E. Giorgi, T. Bhattacharya, B. Foley, K. M. Hastie, M. D. Parker, D. G. Partridge, C. M. Evans, T. M. Freeman, T. I. de Silva, A. Angyal, R. L. Brown, L. Carrilero, L. R. Green, D. C. Groves, K. J. Johnson, A. J. Keeley, B. B. Lindsey, P. J. Parsons, M. Raza, S. Rowland-Jones, N. Smith, R. M. Tucker, D. Wang, M. D. Wyles, C. McDanal, L. G. Perez, H. Tang, A. Moon-Walker, S. P. Whelan, C. C. LaBranche, E. O. Saphire, D. C. Montefiori, Tracking Changes in SARS-CoV-2 Spike: Evidence that D614G Increases Infectivity of the COVID-19 Virus. *Cell* **182**, 812-827.e19 (2020).
10. L. Yurkovetskiy, X. Wang, K. E. Pascal, C. Tomkins-Tinch, T. P. Nyalile, Y. Wang, A. Baum, W. E. Diehl, A. Dauphin, C. Carbone, K. Veinotte, S. B. Egri, S. F. Schaffner, J. E. Lemieux, J. B. Munro, A. Rafique, A. Barve, P. C. Sabeti, C. A. Kyratsous, N. V. Dudkina, K. Shen, J. Luban, Structural and Functional Analysis of the D614G SARS-CoV-2 Spike Protein Variant. *Cell* **183**, 739-751.e8 (2020).
11. J. A. Plante, Y. Liu, J. Liu, H. Xia, B. A. Johnson, K. G. Lokugamage, X. Zhang, A. E. Muruato, J. Zou, C. R. Fontes-Garfias, D. Mirchandani, D. Scharton, J. P. Bilello, Z. Ku, Z. An, B. Kalveram, A. N. Freiberg, V. D. Menachery, X. Xie, K. S. Plante, S.

C. Weaver, P.-Y. Shi, Spike mutation D614G alters SARS-CoV-2 fitness. *Nature* **592**, 116–121 (2021).
12. L. Zhang, C. B. Jackson, H. Mou, A. Ojha, H. Peng, B. D. Quinlan, E. S. Rangarajan, A. Pan, A. Vanderheiden, M. S. Suthar, W. Li, T. Izard, C. Rader, M. Farzan, H. Choe, SARS-CoV-2 spike-protein D614G mutation increases virion spike density and infectivity. *Nat. Commun.* **11**, 6013 (2020).
13. S. M.-C. Gobeil, K. Janowska, S. McDowell, K. Mansouri, R. Parks, K. Manne, V. Stalls, M. F. Kopp, R. Henderson, R. J. Edwards, B. F. Haynes, P. Acharya, D614G Mutation Alters SARS-CoV-2 Spike Conformation and Enhances Protease Cleavage at the S1/S2 Junction. *Cell Rep.* **34**, 108630 (2021).
14. J. Zhang, Y. Cai, T. Xiao, J. Lu, H. Peng, S. M. Sterling, R. M. Walsh, S. Rits-Volloch, H. Zhu, A. N. Woosley, W. Yang, P. Sliz, B. Chen, Structural impact on SARS-CoV-2 spike protein by D614G substitution. *Science* **372**, 525–530 (2021).
15. A. C. Walls, Y.-J. Park, M. A. Tortorici, A. Wall, A. T. McGuire, D. Veesler, Structure, Function, and Antigenicity of the SARS-CoV-2 Spike Glycoprotein. *Cell* **181**, 281-292.e6 (2020).
16. D. Wrapp, N. Wang, K. S. Corbett, J. A. Goldsmith, C.-L. Hsieh, O. Abiona, B. S. Graham, J. S. McLellan, Cryo-EM structure of the 2019-nCoV spike in the prefusion conformation. *Science* **367**, 1260–1263 (2020).
17. F. Amanat, D. Stadlbauer, S. Strohmeier, T. H. O. Nguyen, V. Chromikova, M. McMahon, K. Jiang, G. A. Arunkumar, D. Jurczyszak, J. Polanco, M. Bermudez-Gonzalez, G. Kleiner, T. Aydillo, L. Miorin, D. S. Fierer, L. A. Lugo, E. M. Kojic, J. Stoever, S. T. H. Liu, C. Cunningham-Rundles, P. L. Felgner, T. Moran, A. García-Sastre, D. Caplivski, A. C. Cheng, K. Kedzierska, O. Vapalahti, J. M. Hepojoki, V. Simon, F. Krammer, A serological assay to detect SARS-CoV-2 seroconversion in humans. *Nat. Med.* **26**, 1033–1036 (2020).
18. A. Krarup, D. Truan, P. Furmanova-Hollenstein, L. Bogaert, P. Bouchier, I. J. M. Bisschop, M. N. Widjojoatmodjo, R. Zahn, H. Schuitemaker, J. S. McLellan, J. P. M. Langedijk, A highly stable prefusion RSV F vaccine derived from structural analysis of the fusion mechanism. *Nat. Commun.* **6**, 8143 (2015).
19. R. N. Kirchdoerfer, N. Wang, J. Pallesen, D. Wrapp, H. L. Turner, C. A. Cottrell, K. S. Corbett, B. S. Graham, J. S. McLellan, A. B. Ward, Stabilized coronavirus spikes are resistant to conformational changes induced by receptor recognition or proteolysis. *Sci. Rep.* **8**, 15701 (2018).
20. J. Pallesen, N. Wang, K. S. Corbett, D. Wrapp, R. N. Kirchdoerfer, H. L. Turner, C. A. Cottrell, M. M. Becker, L. Wang, W. Shi, W.-P. Kong, E. L. Andres, A. N. Kettenbach, M. R. Denison, J. D. Chappell, B. S. Graham, A. B. Ward, J. S. McLellan, Immunogenicity and structures of a rationally designed prefusion MERS-CoV spike antigen. *Proc. Natl. Acad. Sci.* **114**, E7348–E7357 (2017).
21. M. I. Zimmerman, J. R. Porter, M. D. Ward, S. Singh, A. Meller, U. L. Mallimadugula, C. E. Kuhn, R. P. Wiewiora, M. F. D. Hurley, A. M. Harbison, C. A. Fogarty, J. E. Coffland, E. Fadda, V. A. Voelz, J. D. Chodera, SARS-CoV-2 Simulations Go Exascale to Capture Spike Opening and Reveal Cryptic Pockets Across the Proteome. 28.
22. L. Casalino, Z. Gaieb, J. A. Goldsmith, C. K. Hjorth, A. C. Dommer, A. M. Harbison, C. A. Fogarty, E. P. Barros, B. C. Taylor, J. S. McLellan, E. Fadda, R. E. Amaro,

Beyond Shielding: The Roles of Glycans in the SARS-CoV-2 Spike Protein. *ACS Cent. Sci.* **6**, 1722–1734 (2020).
23. M. Lu, P. D. Uchil, W. Li, D. Zheng, D. S. Terry, J. Gorman, W. Shi, B. Zhang, T. Zhou, S. Ding, R. Gasser, J. Prévost, G. Beaudoin-Bussières, S. P. Anand, A. Laumaea, J. R. Grover, L. Liu, D. D. Ho, J. R. Mascola, A. Finzi, P. D. Kwong, S. C. Blanchard, W. Mothes, Real-Time Conformational Dynamics of SARS-CoV-2 Spikes on Virus Particles. *Cell Host Microbe* **28**, 880-891.e8 (2020).
24. P. V. Raghuvamsi, N. K. Tulsian, F. Samsudin, X. Qian, K. Purushotorman, G. Yue, M. M. Kozma, W. Y. Hwa, J. Lescar, P. J. Bond, P. A. MacAry, G. S. Anand, SARS-CoV-2 S protein:ACE2 interaction reveals novel allosteric targets. *eLife* **10**, e63646 (2021).
25. V. Calvaresi, A. G. Wrobel, J. Toporowska, D. Hammerschmid, K. J. Doores, R. T. Bradshaw, R. B. Parsons, D. J. Benton, C. Roustan, E. Reading, M. H. Malim, S. J. Gamblin, A. Politis, Structural dynamics in the evolution of SARS-CoV-2 spike glycoprotein. *Nat. Commun.* **14**, 1421 (2023).
26. D. Narang, D. A. James, M. T. Balmer, D. J. Wilson, Protein Footprinting, Conformational Dynamics, and Core Interface-Adjacent Neutralization “Hotspots” in the SARS-CoV-2 Spike Protein Receptor Binding Domain/Human ACE2 Interaction. *J. Am. Soc. Mass Spectrom.* **32**, 1593–1600 (2021).
27. S. M. Braet, T. S. Buckley, V. Venkatakrishnan, K.-M. A. Dam, P. J. Bjorkman, G. S. Anand, Timeline of changes in spike conformational dynamics in emergent SARS-CoV-2 variants reveal progressive stabilization of trimer stalk with altered NTD dynamics. *eLife* **12**, e82584 (2023).
28. C. Chen, R. Zhu, E. A. Hodge, M. A. Díaz-Salinas, A. Nguyen, J. B. Munro, K. K. Lee, hACE2-Induced Allosteric Activation in SARS-CoV versus SARS-CoV-2 Spike Assemblies Revealed by Structural Dynamics. *ACS Infect. Dis.* **9**, 1180–1189 (2023).
29. S. W. Englander, N. R. Kallenbach, Hydrogen exchange and structural dynamics of proteins and nucleic acids. *Q. Rev. Biophys.* **16**, 521–655 (1983).
30. S. W. Englander, L. Mayne, Y. Bai, T. R. Sosnick, Hydrogen exchange: The modern legacy of Linderstrøm-Lang. *Protein Sci.* **6**, 1101–1109 (1997).
31. S. M. Costello, S. R. Shoemaker, H. T. Hobbs, A. W. Nguyen, C.-L. Hsieh, J. A. Maynard, J. S. McLellan, J. E. Pak, S. Marqusee, The SARS-CoV-2 spike reversibly samples an open-trimer conformation exposing novel epitopes. *Nat. Struct. Mol. Biol.* **29**, 229–238 (2022).
32. M. A. G. Hoffmann, Z. Yang, K. E. Huey-Tubman, A. A. Cohen, P. N. P. Gnanapragasam, L. M. Nakatomi, K. N. Storm, W. J. Moon, P. J. C. Lin, P. J. Bjorkman, ESCRT recruitment to mRNA-encoded SARS-CoV-2 spike induces virus-like particles and enhanced antibody responses. bioRxiv [Preprint] (2022). https://doi.org/10.1101/2022.12.26.521940.
33. C. Dacon, C. Tucker, L. Peng, C.-C. D. Lee, T.-H. Lin, M. Yuan, Y. Cong, L. Wang, L. Purser, J. K. Williams, C.-W. Pyo, I. Kosik, Z. Hu, M. Zhao, D. Mohan, A. J. R. Cooper, M. Peterson, J. Skinner, S. Dixit, E. Kollins, L. Huzella, D. Perry, R. Byrum, S. Lembirik, D. Drawbaugh, B. Eaton, Y. Zhang, E. S. Yang, M. Chen, K. Leung, R. S. Weinberg, A. Pegu, D. E. Geraghty, E. Davidson, I. Douagi, S. Moir, J. W. Yewdell, C. Schmaljohn, P. D. Crompton, M. R. Holbrook, D. Nemazee, J. R.

Mascola, I. A. Wilson, J. Tan, Broadly neutralizing antibodies target the coronavirus fusion peptide. *Science* **377**, 728–735 (2022).
34. A. M. Seddon, P. Curnow, P. J. Booth, Membrane proteins, lipids and detergents: not just a soap opera. *Biochim. Biophys. Acta BBA - Biomembr.* **1666**, 105–117 (2004).
35. L. Hoffmann, A. Baier, L. Jorde, M. Kamel, J.-H. Schäfer, K. Schnelle, A. Scholz, D. Shvarev, J. E. M. M. Wong, K. Parey, D. Januliene, A. Moeller, The ABC transporter MsbA in a dozen environments. bioRxiv [Preprint] (2024). https://doi.org/10.1101/2024.06.20.599867.
36. K. Krishna Kumar, H. Wang, C. Habrian, N. R. Latorraca, J. Xu, E. S. O'Brien, C. Zhang, E. Montabana, A. Koehl, S. Marqusee, E. Y. Isacoff, B. K. Kobilka, Stepwise activation of a metabotropic glutamate receptor. *Nature* **629**, 951–956 (2024).
37. J. R. Byrum, E. Waltari, O. Janson, S.-M. Guo, J. Folkesson, B. B. Chhun, J. Vinden, I. E. Ivanov, M. L. Forst, H. Li, A. G. Larson, W. Wu, C. M. Tato, K. M. McCutcheon, M. J. Peluso, T. J. Henrich, S. G. Deeks, M. Prakash, B. Greenhouse, J. E. Pak, S. B. Mehta, multiSero: open multiplex-ELISA platform for analyzing antibody responses to SARS-CoV-2 infection. medRxiv [Preprint] (2021). https://doi.org/10.1101/2021.05.07.21249238.

Chapter 4:

Mapping the Conformational Landscape of the Rabies Virus Glycoprotein

---

4.1 Introduction

4.1.1 Rabies Virus is a deadly lyssavirus and causes preventable deaths around the world

Rabies virus (RABV), a bullet shaped, negative sense RNA virus which is a member of the Rhabdoviridae family and lyssavirus genus, is the causative agent of rabies (*1*). RABV infection occurs through contact with saliva of an infected animal and thus is primarily transmitted through bites and scratches from infected animals. Once transmitted, the virus travels through the nervous system until it reaches the central nervous system where it causes neurological symptoms including agitation, hallucination, paranoia, hypersalivation and hydrophobia. Even with effective therapeutics, approximately 60,000 people per year die from RABV infection worldwide (*2*). These deaths are primarily in areas of the world where people live in close proximity to wild animals and lack access to medical care (*1*). Many of these deaths are in children who do not alert adults to the fact they were bitten or scratched by a wild animal so proper prophylactic measures were not taken before the onset of symptoms, at which point there are essentially no viable treatments to save the patient (*1*). When reported before the onset of symptoms there are effective therapeutics including vaccines and polyclonal antibodies purified from serum of people who have previously been exposed to rabies virus (*3*).

The current rabies vaccines are mainly made in Vero cell culture and contain inactivated viruses of varying strains (*4*). As a pre-exposure prophylactic, two doses are given over the span of one week and for some individuals a booster is needed within the first three years (*5*). Currently, in the United States, the CDC only recommends pre-exposure prophylactic vaccination for high risk individuals, which includes those who work with wildlife, veterinarians as well as people traveling to areas where they are at high risk of a rabies exposure. However, the rabies vaccine is also an effective post-exposure prophylactic treatment as the virus can take days or months to reach the central nervous system after exposure (*4*). As a post-exposure prophylactic, patients receive four doses of two weeks as well as concomitant antibody therapy, typically a polyclonal antibody sera from a previously vaccinated patient (*3*).

Although effective therapeutics exist, there are remaining challenges in treating rabies including the cost of vaccination and access to therapeutics where they are needed most. The World Health Organization has determined there are ways to reduce the volume of vaccine needed by changing from an intramuscular injection to intradermal administration, making them more accessible (*6*). Current rabies

vaccinations can cost upwards of $100 USD in countries where daily income is around $1-2 USD resulting in a barrier to treatment (*6*)). In comparison, in these same countries, other vaccines such as measles and flu cost the equivalent of $0.20-3 USD (*7*, *8*). This difference in cost may represent the discrepancy in investment between vaccines that are routinely given and thus many doses are required, and one that is primarily only administered after exposure, leaving the price very high. If the price of rabies vaccination could be lowered, it may result in more children undergoing pre-exposure prophylactic vaccination which could prevent many deaths. In the United States rabies post-exposure prophylactic treatment can be tens of thousands of dollars, which is a strain on the medical system (*9*). There has also been work in recent years to find therapeutics that could cure symptomatic rabies which has proven to require creative and extreme measures (*10*). Clearly there is room for improvement in RABV therapeutics to make them more accessible, cost-effective and efficacious.

4.1.2 RABV glycoprotein is the viral fusion protein and is the proposed target of next generation therapeutics

With a continuing and renewed interest in therapeutics for rabies there has been an increased focus on the rabies virus glycoprotein (RABV-G). Before 2020, in the absence of structural data on RABV-G, it was difficult to test hypotheses of where antibodies bound and how mutations impacted the protein. Most studies relied on hypotheses inferred from structural data for Indiana Vesiculovirus, previously known as vesicular stomatitis virus (VSV-G), which is a virus of the same family (Rhabdoviridae) but different genus. Structures of VSV-G in the prefusion (*11*) and postfusion conformations (*12*) were assumed to have the same architecture as RABV-G. In 2020, a crystal structure of a monomeric soluble RABV-G construct secreted from insect cells was solved in both the prefusion conformation, and the extended intermediate conformation (*13*). Later, two cryo-EM models of RABV-G were determined from protein expressed in mammalian cells, both in the presence and absence of the transmembrane domain in detergent (*14*, *15*). These models confirm that the structure of RABV-G is architecturally similar to VSV-G, but reveals some differences as well.

These structures of RABV-G helped put a long history of antibody research into context. RABV-G is a trimeric protein and each protomer has two glycosylation sites and is made up of three extraviral domains (Figure 1). The central domain (CD) consists of the N-terminus as well as the final 100 C-terminal residues before a linker that leads to the transmembrane domain which then leads into the small intraviral domain. A pleckstrin homology domain (PHD) and a fusion domain (FD), which is where the two fusion loops are located (*13*), are in between the N-terminus and the rest of the CD (Figure 1). In the prefusion conformation of RABV-G the central helix leading from the CD to the PHD is bent such that the PHD and FD lie parallel to the CD and the fusion loops point towards the viral membrane (Figure 1). To adopt the extended intermediate

conformation, the central helix fully reforms, swinging the PHD and FD away from the viral membrane so the three domains are in line with one another. The fusion loops are now pointed away from the viral membrane in hopes of burying in a cell membrane.

A unique feature of both RABV-G and VSV-G is that the conformational change between the prefusion conformation and the extended intermediate is reversible. At physiological pH both conformations are sampled but the exact proportion and timescale of interconversion is unknown (*13*, *16–21*). This conformational change is pH dependent. The virus enters the cell through the endosome, which begins to acidify leading to a drop in pH which drives the equilibrium to the extended intermediate, leading to fusion.

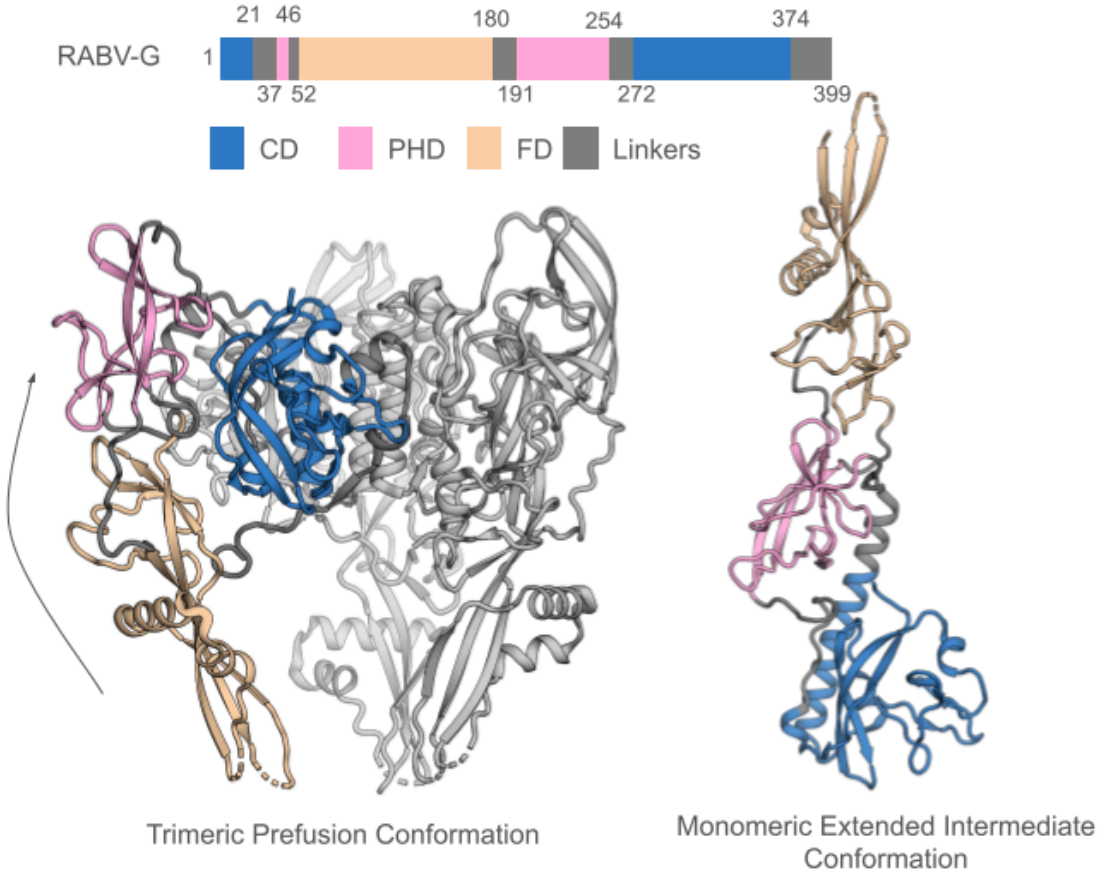

Figure 1: Topology and Fold of RABV-G in the Prefusion and Extended Intermediate Conformations. Sequence map of RABV-G colored by domain (as in Ng. et al 2022). Trimeric prefusion structure (PDB: 7U9G (Callaway et al 2022)) colored by domain. Arrow shows direction that the PHD/FD arm of the monomer moves to reach the extended intermediate conformation. Monomeric extended intermediate structure (PDB: 6LGW (Yang et al 2020) colored by domain.

Thus, at low pH the extended intermediate dominates, while at slightly basic pH the prefusion conformation dominates. Much of what is known about this conformational change comes from research on VSV-G with the presumption that it also applies to RABV-G. VSV-G has a much broader research history due to the relative safety of VSV compared to RABV (VSV infection only causes flu like symptoms in humans instead of CNS symptoms and death) and the fact that VSV-G is much easier to purify and crystallize than RABV-G and hence there has been structural information for much longer.

The Harrison lab has carried out an elegant study illustrating and investigating this reversible conformational change in VSV-G (*21*). Fluorescent VSV was imaged while flowing over a suspended lipid bilayer. At pH 7.4, the fluorescent particles appear to “roll” or move in the direction of the buffer flow. In a pH 6.6 buffer, these particles no longer move and stay “arrested” in the membrane. The interpretation is that at pH 7.4, a critical percentage of the VSV-G on the virus are in the prefusion conformation, so the fusion loops are not exposed and the virus moves with the flow of buffer; however, switching the buffer to pH 6.6 led to a critical percentage of the fusion loops of VSV-G being exposed and burying in the suspended lipid bilayer, leading the virus no longer flowing with the buffer. Although these are single virus experiments, they still report on the bulk properties of the protein, because each virus has hundreds of copies of VSV-G on its surface. Therefore, although they quantify the percent of rolling or arrested viral particles as a function of pH, it is hard to know if this directly correlates with the percent of individual proteins in the prefusion or extended intermediate conformation. These experiments also give a sense of the timescale for the interconversion: it takes approximately 20-30 seconds for the particle to begin rolling after the pH jumps to 7.4 from 6.6, and similarly it takes about 10-20 seconds for the particles to arrest after the 7.4 to 6.6 jump. But again, that does not necessarily mean that the timescale of interconversion is on the 10s of seconds timescale as the percentage of VSV-G that need to convert to change the behavior of the viral particle is unknown.

The reason for the reversible nature of this conformational change and its evolutionary benefits are unknown. That said, understanding this conformational transition is important for the development of therapeutics. As with other viral fusion proteins, targeting therapeutics and vaccines to the prefusion conformation of RABV-G is expected to result in the best neutralization of the virus. Given that RABV-G is samples both conformations before infecting a cell, the immune system potentially generates antibodies to both conformations and it is unknown if therapeutics that specifically bind the extended intermediate are neutralizing. In addition, discovering mutations that lock RABV-G in the prefusion conformation is important for both better vaccines as well as expression and purification practicality. In the extended intermediate, the hydrophobic fusion loops are exposed which can cause the proteins to aggregate, so expression and purification will be greatly simplified if the fusion loops

remain tucked down. In sum, new methods are needed to better understand the conformational landscape of RABV-G in the pursuit of better therapeutics.

4.1.3 Methodology to monitor the conformational landscape of RABV-G is still being developed and understood

Currently, there are no methods to determine which conformation (prefusion or extended intermediate) dominates the RABV-G conformational landscape. In the past, this was attempted through both viral fusion assays as well as conformation-specific antibody binding assays (*15*, *22*). While both methods may detect changes in conformational landscape, they have convoluting factors that make them difficult to interpret. With fusion assays, a lack of fusion may be due to RABV-G being locked in its prefusion conformation but could also be from RABV-G being unable to undergo the conformational change from extended intermediate to postfusion. In antibody-binding readouts, antibodies that specifically recognize one conformation or the other will shift the conformational landscape to favor that conformation due to thermodynamic linkage. So, while changes in antibody affinity may indicate a change in conformational landscape, it is hard to get a quantitative measurement of the change.

Hydrogen deuterium exchange monitored by mass spectrometry provides an alternative approach that may provide a better and more direct method for monitoring this conformational change. The hypothesis is that both conformations will undergo hydrogen exchange differently from one another due to a change in contacts between the domains and thus a change in local stability. HDX-MS also has the benefit of being able to study the protein ensemble in solution without needing labels or binding, both of which could unknowingly change the conformational landscape.

4.2 Results

4.2.1 HDX-MS can distinguish the prefusion and extended intermediate conformations

To test the hypothesis that HDX-MS can distinguish the two conformations due to differential uptake at pH's where the conformational landscape is assumed to be different, HDX-MS was conducted on a soluble monomeric construct with the fusion loops mutated to GGSGG linkers, to prevent aggregation (*13*). This construct is expressed in insect cells and affinity purified with a nickel column followed by size exclusion chromatography (see Methods).

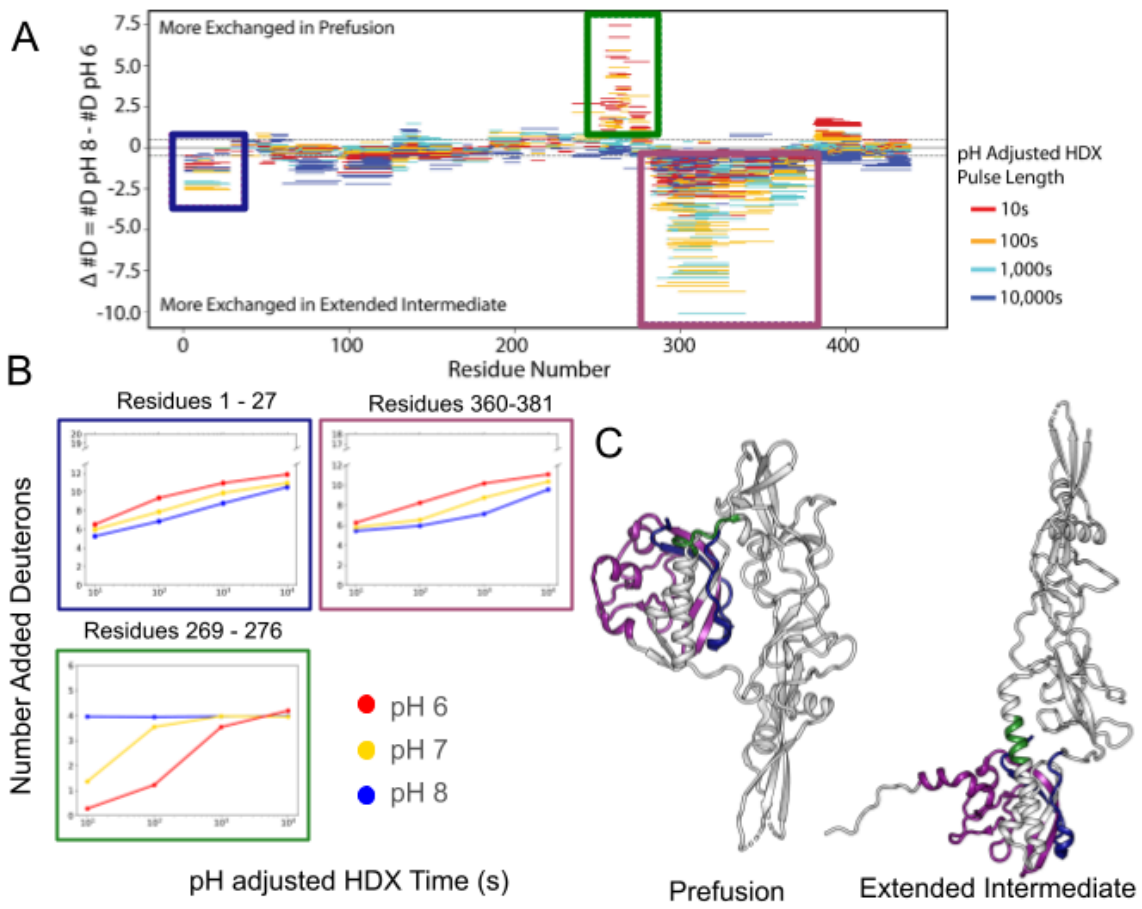

Figure 2: HDX-MS of RABV-G at pH 6 and pH 8. (A) Difference Woods plot of HDX done at pH 6 and pH 8. Regions showing interpretable differences are indicated with a green, blue or purple square. The corresponding uptake plots are shown in (B) with a border color indicating which region. Each region is colored on a prefusion structure (PDB: 7U9G) and an extended intermediate (PDB: 6LGW) in (C).

HDX-MS was performed at pH 6 and pH 8 over a range of timescales (10-10,000 seconds at pH 8, equivalent to 1,000-1,000,000 seconds at pH 6). Unlike in the HDX-MS of SARS-CoV-2 spike protein, we do not expect to see bimodal exchange as the prefusion and extended intermediate are likely in fast exchange with one another based on data from VSV-G which suggests the timescale of exchange is on the milliseconds to seconds timescale. Instead, we see unimodal exchange distributions at both pHs. When the difference of exchange between these two pHs is visualized on a Woods plot (Figure 2A) there are three regions that show notable differences (Figure 2B). These regions correlate with structural differences of the two different conformations (Figure 2C). The first region is the N-terminus of the protein, which in the prefusion structure is sandwiched between the CD and the PHD/FD occluding it from solvent while in the extended-intermediate conformation while the PHD/FD arm has

swung up, is now solvent exposed leading it to be more exchanged in the pH 6 exchange than the pH 8 exchange. Similarly much of the CD exchanges more in the pH 6 exchange than in the pH 8 exchange, which is explained by an increase in local stability when the CD and the PHD/FD are making contacts in the prefusion conformation which is then lost when the PHD/FD has moved into the EI conformation. On the other hand peptides that are in the middle of the central helix are more exchanged in the pH 8 exchange than the pH 6 exchange, which again is logical as in the prefusion conformation this region is in a loop conformation not forming hydrogen bonds, where in the EI these residues are helical and forming hydrogen bonds. Outside of these regions there are minor regions that do have differential exchange that are not easily understood by the structural data and the magnitude of change is much smaller than the other regions (Figure 2A). The three regions denoted in Figure 2 can be used as reporter peptides for the conformational change.

4.3.2 Comparing uptake at varying pH to determine a percent prefusion is not feasible

The original goal for this project was to use HDX-MS to quantify the percent prefusion

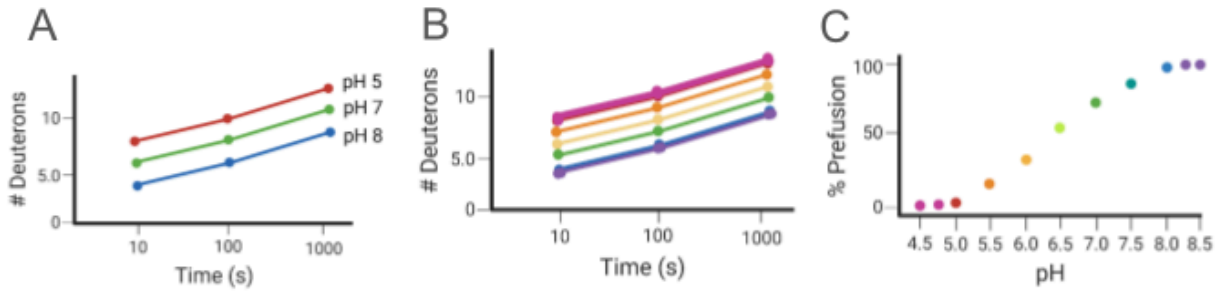

Figure 3: Visualization of theory of how percent prefusion can be calculated from HDX data. (A) An example of if we knew that pH 5 and pH 8 were where there was 100% extended intermediate and 100% prefusion respectively, we could place the intermediate percentages of a pH 7 population. (B) To determine where these hypothetical baselines are, we must find pH's where the exchange is no longer changing and thus the curves overlap. (C) Once these baselines are established, we should be able to plot percent prefusion against pH.

under different conditions. The hypothesis is that if the conformations are in fast exchange (milliseconds-seconds) in comparison to labeling time, then the observed rate of exchange (k_{obs}) will be the linear combination of the exchange from each conformation (k_{pre} and k_{EI}) multiplied by the fraction of the population in each conformation (fraction prefusion = f_{pre} and fraction extended intermediate = f_{EI}).

$$k_{obs} = k_{pre} * f_{pre} + k_{EI} * f_{EI} \text{ (Eq. 1)}$$

Since f_{pre} and f_{EI} must sum to one under this two state model, this can be rewritten as

$$f_{pre} = (k_{obs} - k_{EI}) / (k_{pre} - k_{EI}) \text{ (Eq. 2).}$$

This model requires several assumptions. One is that, as mentioned before the two conformations must be in fast exchange in comparison to the intrinsic rate of hydrogen exchange. The other is that there is no pH dependency on stability or exchange beyond the conformational change in question. Finally, this model requires the conformational change to be two state and not have any intermediates that exchange differently than the two end states.

Originally I attempted to use this model but instead of calculating a rate, I would compare raw exchange numbers (Figure 3A), essentially multiplying each rate in equation 2 by a time in seconds resulting in

$$f_{pre} = (\#D_{obs} - \#D_{EI}) / (\#D_{pre} - \#D_{EI}) \text{ (Eq. 3).}$$

This calculation should be equivalent as long as in every condition we are in the exchangeable regime (not fully unexchanged and not fully exchanged).

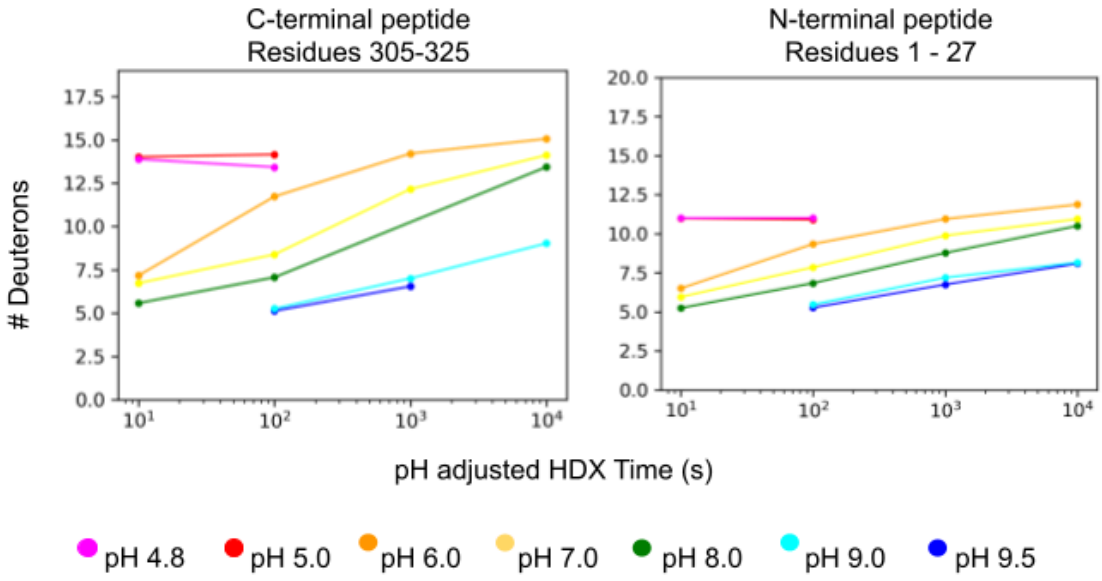

Figure 4: HDX of RABV-G over pH range 4.8 - 9.5. In an attempt to make the calculations described in Equations 1-3 and Figure 3 HDX was performed at a wide pH range to find where exchange plateaus indicating homogenous populations. Peptide level exchange for an N-terminal peptide and C-terminal peptide showed similar exchange behavior at each pH but exchange has not plateaued at the extreme pHs and the protein is not in the exchangeable regime so a comparison cannot be made.

Since we are shifting the equilibrium with pH, the intrinsic rate of exchange is also changing; however, we can account for this change (k_{int} is ten times faster for each unit of increased pH) and adjust the time point we are comparing to account for the difference in pH (e.g. a 10 second time point at pH 7 is equivalent to a 100 second time point at pH 6).

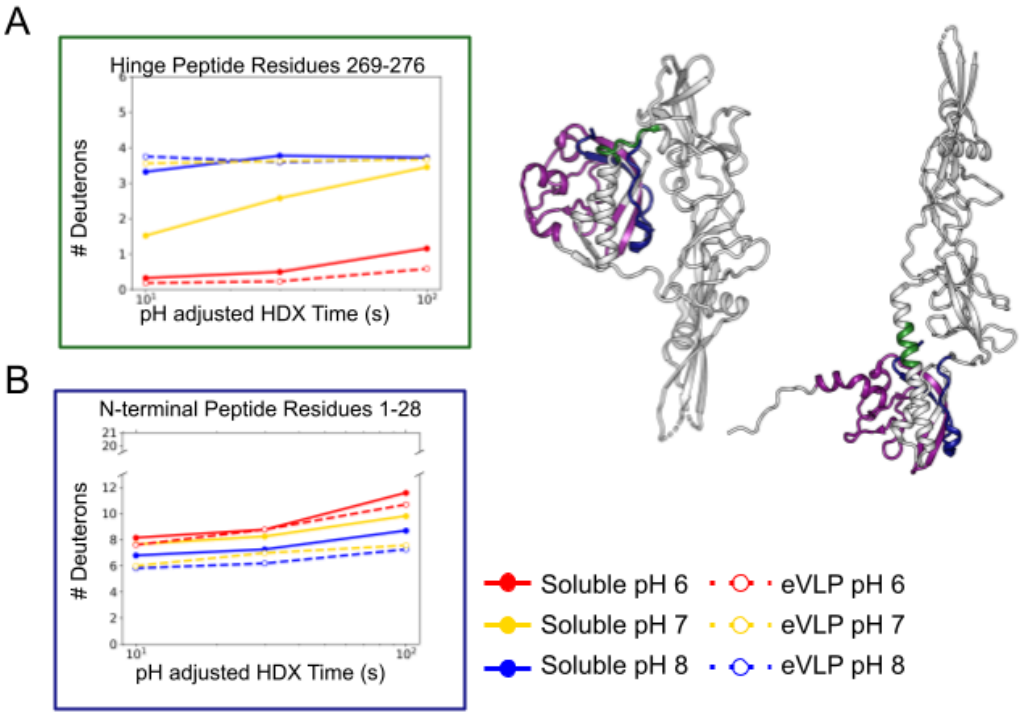

The first step was to try to determine at what pH's RABV-G is in nearly 100% prefusion

Figure 5: HDX of soluble RABV-G vs RABV-G in an eVLP at pH 6, 7 and 8. Exchange of the hinge peptide (A) and the N-terminal peptide (B) both suggest an increase in prefusion conformation on the eVLP at pH 7 and 8. The border color of each uptake plot corresponds to the coloring on the protein structures on the left.

and 100% extended-intermediate conformations. That is to find acidic and basic pH's where the exchange no longer changes, indicating the conformational equilibrium is no longer changing (Figure 3B and 3C). Therefore, I did hydrogen exchange over multiple ranges of pH with adjusted timepoints in order to find these baselines. In the measurable range of pH 4.8 to pH 9.5, the exchange on the acidic side was completely exchanged while the exchange on the basic side still showed measurable difference between pH 9.0 and pH 9.5 (Figure 4). Given there are over 4 orders of magnitude between the highest and lowest pH, a 44 hour time point at pH 4.8 was equivalent to a 3

second time point at pH 9.5, thus it became experimentally unfeasible to compare these data. Furthermore, we are no longer under our assumption where we are in the exchangeable range as it appears that at pH 5 and pH 4.5 in this time comparable range the protein is fully exchanged. Therefore, under these conditions it does not seem possible to calculate a percent prefusion using this method.

4.3.3 Comparing HDX uptake qualitatively can allow us to make conclusions about shifts to the conformational landscape

While quantitatively determining a percent prefusion may be experimentally infeasible as described above, we can still monitor shifts in the conformational landscape by observing changes in hydrogen exchange at different pH's compared to a reference construct. For example by performing hydrogen exchange at pH 6, 7 and 8 with a reference wild-type sequence and then comparing hydrogen exchange of a variant sequence, we can observe changes. If exchange at all pH's is shifted towards

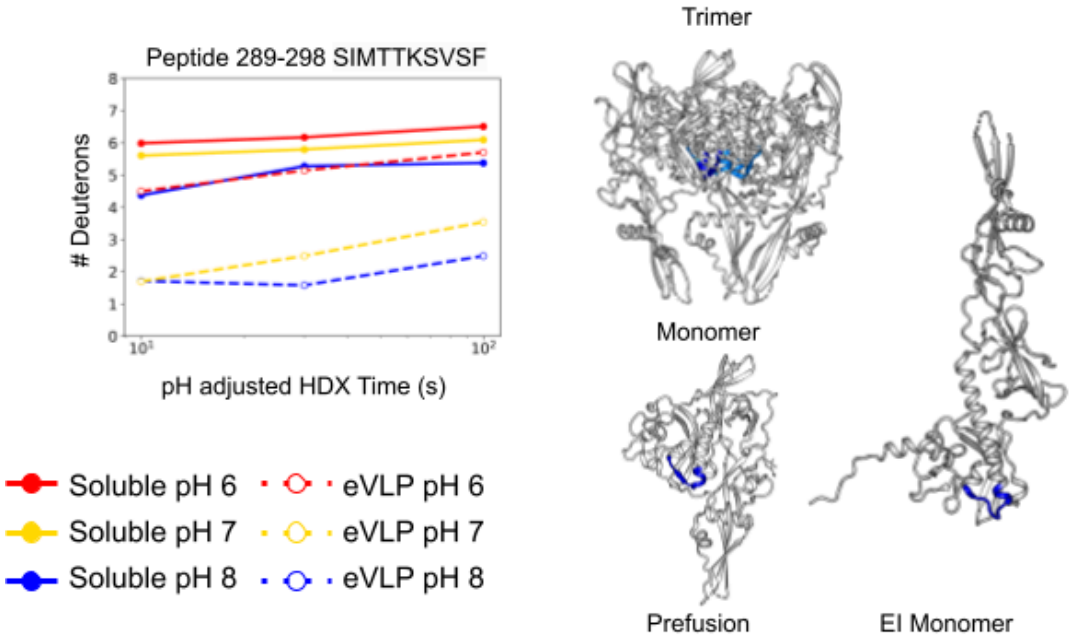

Figure 6: Differential uptake of a peptide between soluble RABV-G and eVLP RABV-G. The peptide is at the trimer interface in the trimeric prefusion structure but would be solvent exposed in a monomeric prefusion and extended intermediate conformation.

the exchange at pH 8 of the reference sequence, then we can conclude that the variant sequence is more prefusion than the reference sequence. This strategy was employed to answer the following questions. What is the impact of the membrane and

trimerization on the conformational landscape of RABV-G? And what mutations can stabilize the prefusion conformation?

4.3.4 Trimerization and the membrane environment stabilize the prefusion conformation

To address the first question about the effect of the membrane and trimerization, I again used the enveloped virus-like particle technique that was described in Chapter 2. Briefly, by appending an EABR tag to the C-terminal, intracellular end of RABV-G, the ESCRT machinery is recruited leading to the release of extracellular vesicles into the cell culture media that are densely coated in RABV-G and can be purified via ultracentrifugation and size exclusion chromatography (see Methods). In order to carry

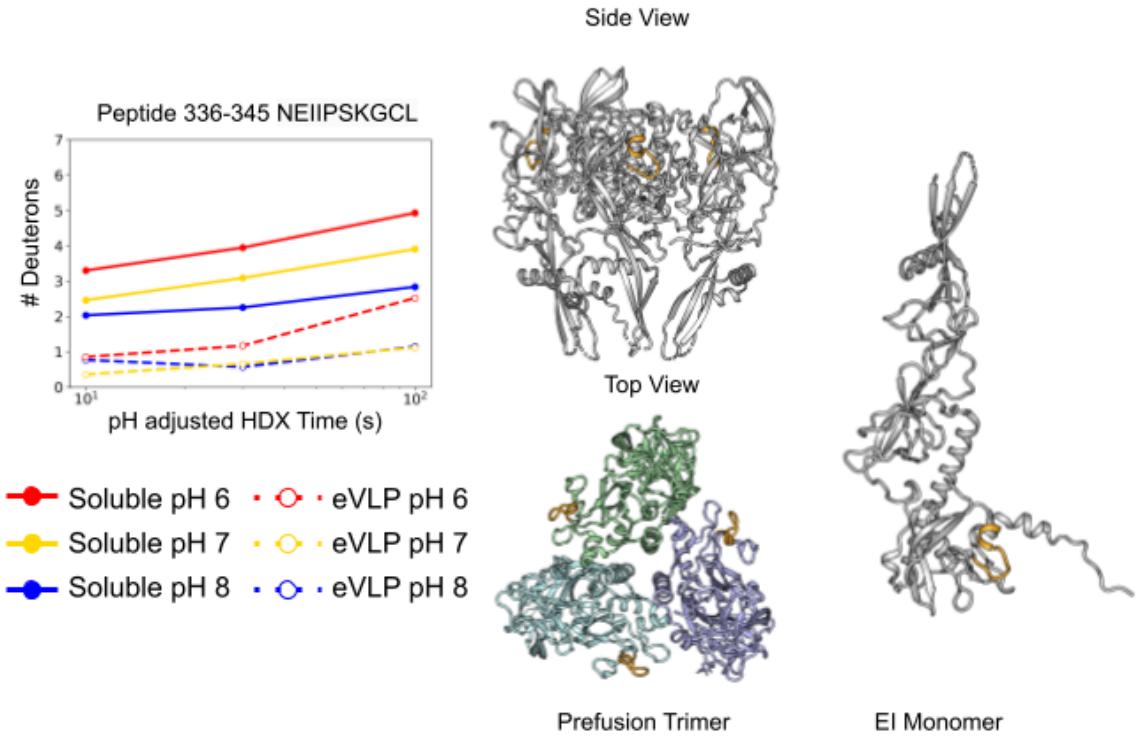

Figure 7: Differential uptake of a peptide between soluble RABV-G and eVLP RABV-G which is not explained by structures.

out HDX-MS on these particles, the lipids must be removed during the quenching step, which is achieved by including 25 mg/mL of zirconium oxide in the quench buffer which binds to phospholipids and then removed from the solution via filtration or pelleting in a quick centrifugation step. While this approach results in fewer identified peptides

compared to online digestion with soluble RABV-G, but there are still 30-50 peptides resulting in ~40-50% coverage and importantly we have coverage in the regions that we previously identified to be good reporters of conformation (N-terminus, C-terminal domain and the hinge peptide). This coverage can likely be improved given what was learned from optimization of SARS-CoV-2 spik eVLPs in Chapter 2.

In comparing the deuterium uptake for both the soluble and eVLP constructs at pH 6, 7 and 8, we find that exchange at pH 6 is fairly similar for both constructs, but exchange at pH 7
and pH 8 are shifted to be more exchanged (in the case of the hinge peptide) (Figure 5A) or more protected (in the case of the N-terminus peptides) (Figure 5B) in the eVLP than in the soluble construct. This suggests that the trimerization and membrane environment stabilizes the prefusion conformation at neutral and slightly basic pH's while the protein is still able to adopt the extended intermediate at slightly acidic pH's (Figure 5B). There are two other regions that experience change in uptake between the soluble and eVLP construct, one region is consistent with protection due to contacts

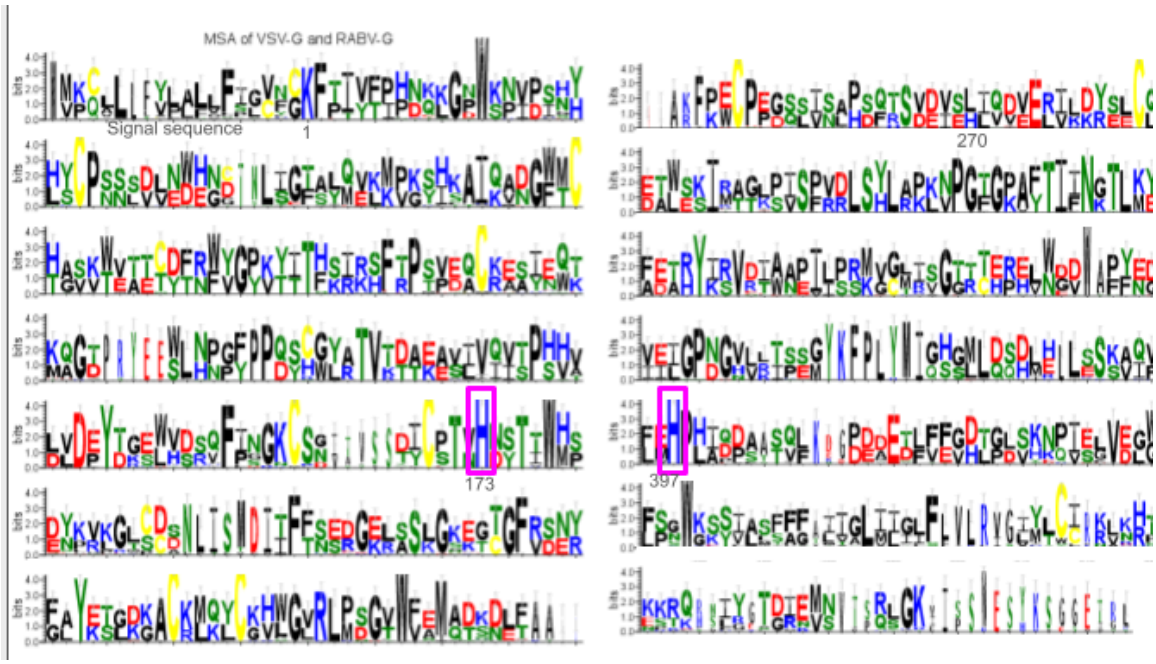

Figure 8: MSA made by aligning sequences of RABV-G and VSV-G from uniprot. The two histidines that were mutated are indicated in magenta boxes with the sequence position underneath. Key residues are also noted with the RABV-G sequence numbering.

along the trimerization interface (Figure 6). Interestingly, at pH 6, the protection compared to the soluble construct is lost, suggesting that the extended intermediate does not make trimeric contacts at this site; the lack of trimeric contacts suggests that the extended intermediate monomerizes in the process of changing conformations. It is

less clear why the other region would show a difference in exchange, but it could be due to a change in stability upon trimerization or a reordering of this loop (Figure 7).

4.3.5 Mutation of hypothesized critical ionizable residues in soluble RABV-G did not result in a shift of the conformational landscape

To address the question of mutations that may shift the conformational landscape, a few different approaches were taken. The first strategy was finding conserved ionizable residues that could undergo a pH dependent charge change that may result in the conformational change by creating a multiple sequence alignment (MSA) of RABV-G and VSV-G from different strains (Figure 8).

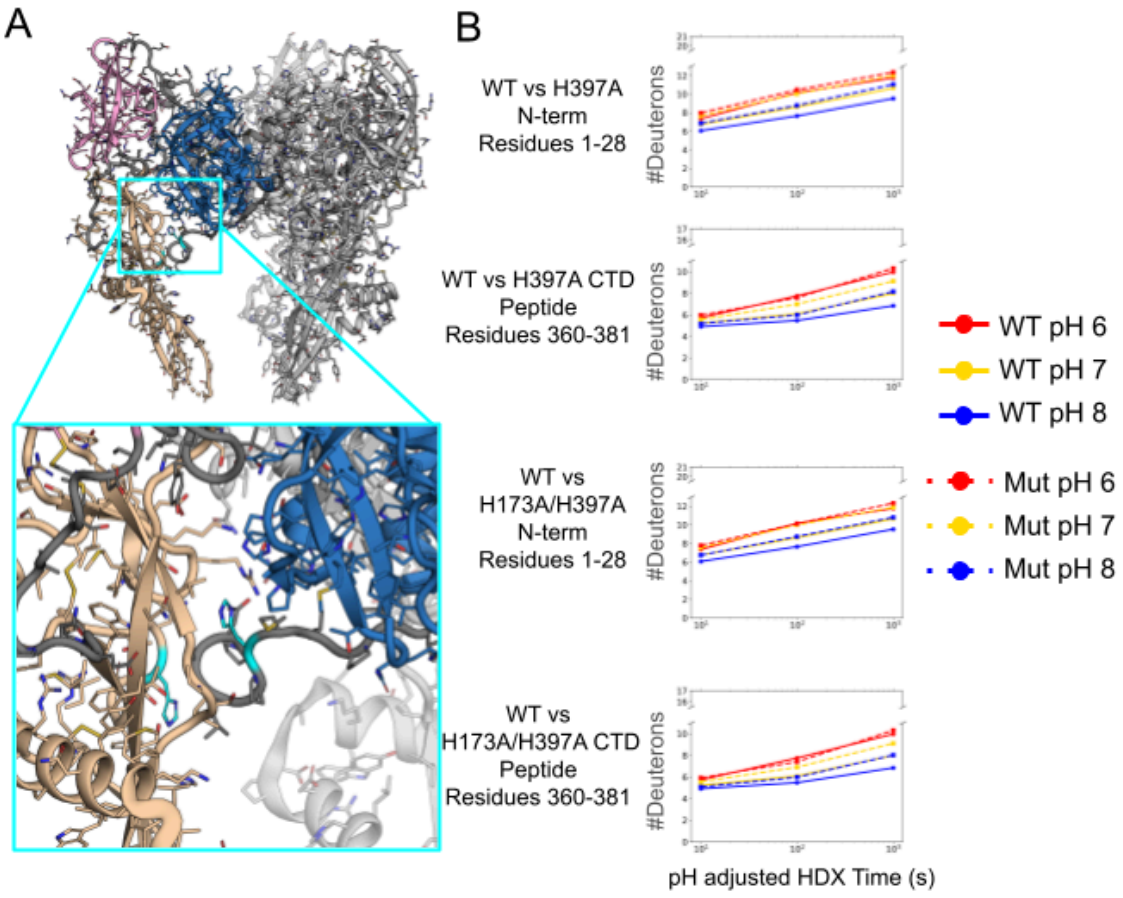

Figure 9: HDX of soluble RABV-G with mutations of conserved ionizable residues (H173A and H397A). The location of these histidines is in the interface between the PHD/FD arm and the CD as shown on the left. The uptake was not significantly changed between these mutants and the reference sequence indicating there was not a large shift in conformational landscape. Instead the exchange may suggest these mutations destabilize the protein.

Initially, the residues that stood out were H397 and H173, both of which are in the interface of the CD and the PHD/FD arm (Figure 9A). Given the pKa of histidine (~6.0),

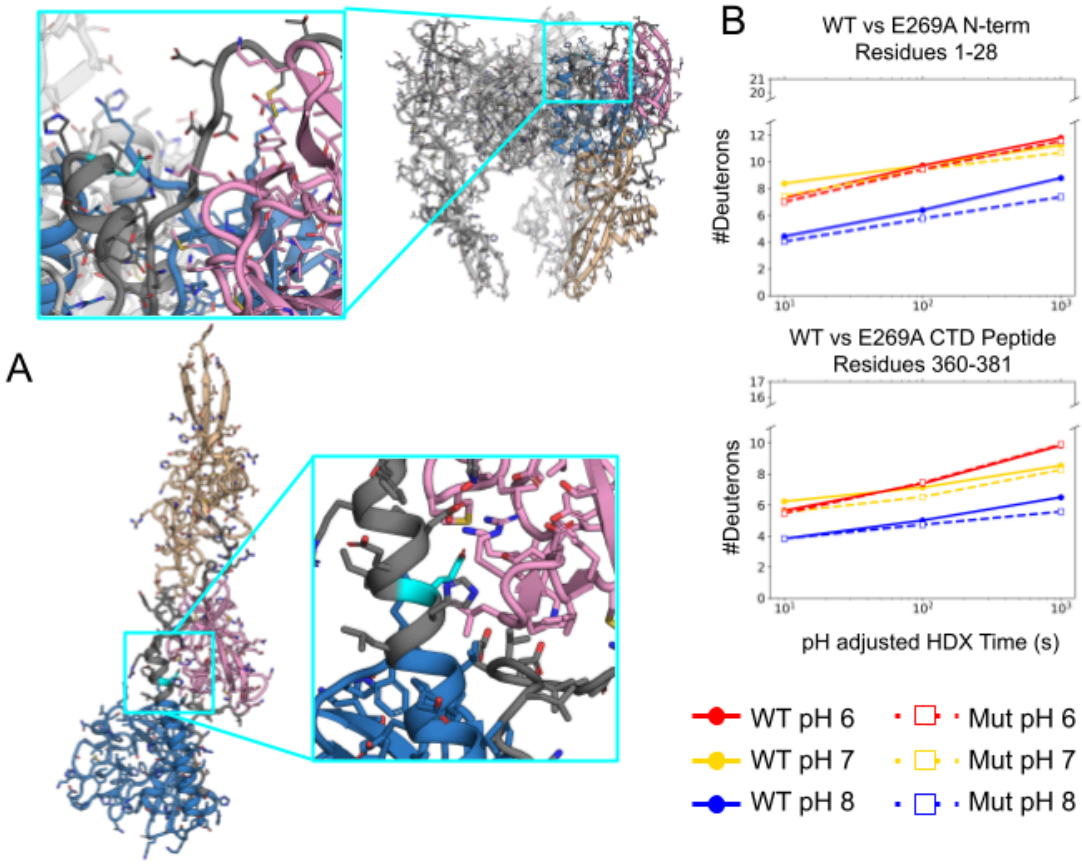

Figure 10: HDX of RABV-G E269A was not much different from exchange of the reference RABV-G sequence as shown on the right. The location of this mutation is shown on the left, there is not an obvious reason that the pKa of this residue would be so different between the conformations (prefusion 4.27 extended intermediate 8.20).

these histidines are likely charge neutral at pH 7-8 and become positively charged upon acidification, which could lead to repulsion from nearby charged residues resulting in the PHD/FD arm moving into the extended intermediate conformation. Following this hypothesis, variants were made with H397A in the presence and absence of H173A and hydrogen exchange was carried out at pH 6, 7 and 8. Compared to the reference sequence, hydrogen exchange behavior did not drastically change with the notable exception of at pH 8 the exchange is shifted to be more similar to the exchange at pH 6 and 7 (Figure 9B). This suggests that these mutations either shift the conformational landscape towards the extended intermediate, or globally destabilizes the protein resulting in more deuterium uptake.

Another similar, more systematic approach was taken by using a structural pKa prediction algorithm and looking for amino acids whose pKa dramatically shifted between the structures. The only residue that had a dramatically shifted pKa was E269 where the pKa was predicted to be 4.27 (Figure 10A) in the prefusion conformation and 8.20 in the EI (Figure 10B). E269 resides in the 'central helix' in the part that is a loop in the prefusion and helical in the EI. On visual inspection, there is no obvious structural

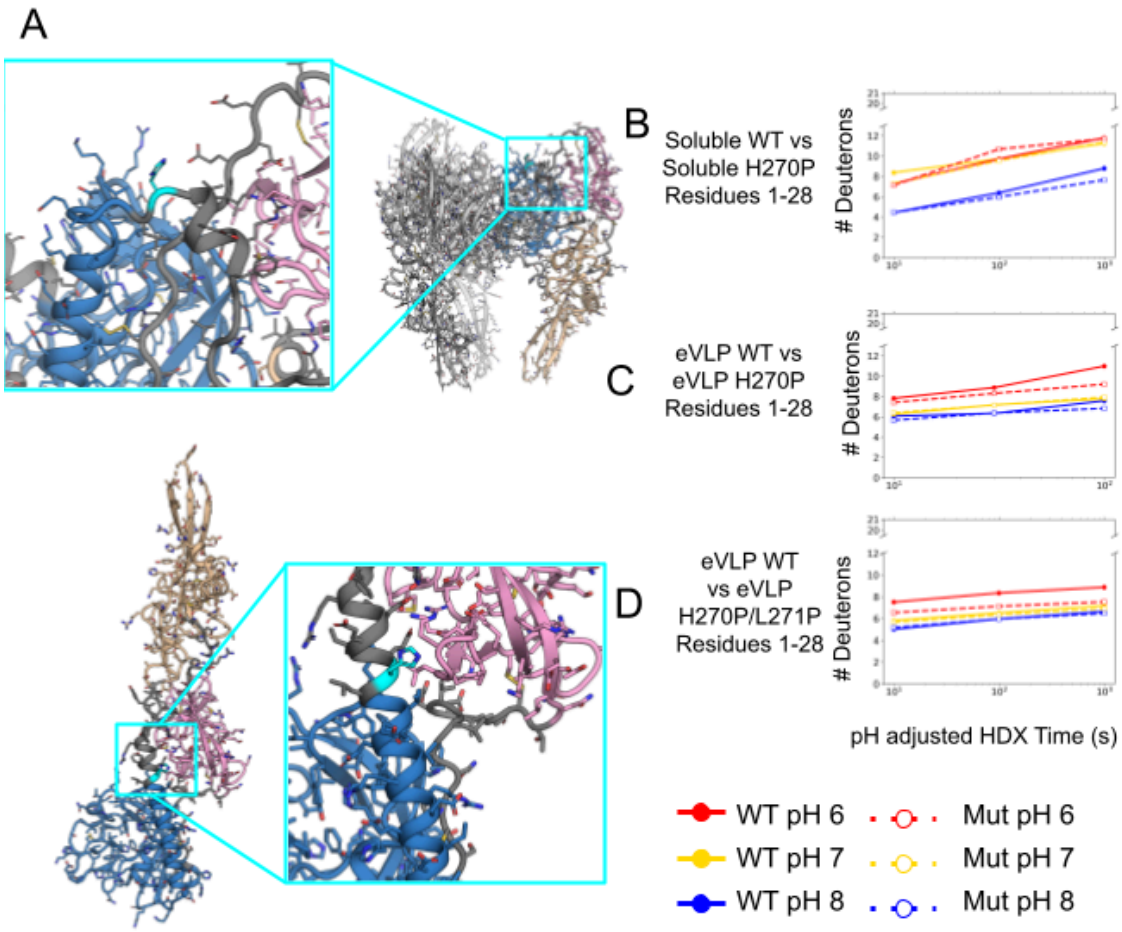

Figure 11: HDX of RABV-G with helix breaking mutations compared to the reference sequence. (A) location of the helix breaking mutations shown on both the extended intermediate and prefusion conformation. (B) Uptake plot comparing exchange of the N-terminal peptide of soluble RABV-G with and without H270P. (C) Uptake plot comparing exchange of the N-terminal peptide of eVLP RABV-G with and without H270P. (D) Uptake plot comparing exchange of the N-terminal peptide of eVLP RABV-G with and without H270P/L271P

explanation for why the pKa of this residue would be shifted, but it is in a different chemical environment in both conformations (Figure 10A-B). Therefore, the E269A variant was made in the soluble construct and again very little difference in hydrogen exchange was observed between this sequence and the reference sequence (Figure 10C).

4.3.6 Helix disrupting mutations have a slight impact on the conformational landscape

The final strategy employed was to introduce prolines into the region of the central helix that is helical in the EI and in a loop in the prefusion conformation (Figure 11A). The hypothesis is that the prolines disfavor the formation of helices and therefore would favor the prefusion conformation where the proline is in a loop. This strategy was employed in Ng. *et al*. and they suggested H270P has a dramatic effect on stabilizing the prefusion conformation based on fusion data as well as binding of an proposed conformational specific antibody. In soluble RABV-G H270P, the exchange at pH 6, 7 and 8 were indistinguishable from exchange on WT soluble RABV-G (Figure 11B). However, with an eVLP displaying RABV-G H270P, the exchange at pH 6 was shifted in the direction of the prefusion conformation when monitored in peptides covering the N-terminus and the CD. This suggests a shift in the conformational landscape to prefer the prefusion conformation at low pH; however, this change is very slight suggesting that the EI is still sampled (Figure 11C). To further investigate the effect of helix breaking mutations, a second proline mutation was made at position 271, resulting in an eVLP displaying RABV-G H270P/L271P. The hydrogen exchange at pH 6 again revealed a slight shift (albeit more than H270P alone) in exchange indicating that the prefusion conformation is further stabilized but the protein is still pH sensitive and sampling both conformations (Figure 11D).

4.4 Discussion

While this project is still in progress, at time of writing of this thesis the results give us insights both into this methodology as well as RABV biology. The method developed with soluble, monomeric, RABV-G reveals peptides that exchange differently in the prefusion and extended intermediate conformations. These peptides can thus be used to monitor the conformational landscape of RABV-G. The biggest challenge of this project is finding the pHs where we can assume the population is 100% extended intermediate and 100% prefusion conformation in order to quantitatively determine the fraction of each conformation under different conditions. Given the pH range we tested went from 4.8 to 9.5 and both baselines were not reached it is not possible given current conditions and instrumentation to use this approach. Instead it may be possible to calculate a fraction prefusion by calculating a rate for a single peptide at a variety of pHs by taking exchange timepoints from seconds to days or weeks of exchange. These rates can then be compared by correcting for pH as under EX2 conditions the observed rate is equal to K_{eq} multiplied by k_{int}. As we know that k_{int} decreases by a factor of 10 with every unit of decrease in pH, the k_{obs} can be multiplied or divided by 10 to make them comparable and thus we can compare K_{eq} for a peptide. It could be possible that

even with this method we do not find baselines as there could be pH dependent stability effects not related to the conformational change.

Regardless of whether we can quantify a fraction prefusion using hydrogen exchange, the qualitative approach described in this paper can also give us insights into the conformational landscape of RABV-G. Using this method, we determined that the membrane stabilizes the prefusion conformation. We also found that some helix breaking mutations slightly stabilize the prefusion conformation while the other mutations we tried did not have a large effect on the conformational landscape. In the future this method can continue to be employed for other mutations as well as to determine how the conformational landscape changes in the presence of an antibody.

Our results also provide insights into the biology of RABV-G. It is surprising how broad the transition from extended intermediate to the prefusion conformation is over the pH range tested (Figure 4). RABV-G interacts with host-cells at physiological pH, around 7.2. The optimal pH for viral fusion is 5.5 (*19*). Therefore we would expect that over this narrow pH range (less than 2 units) we would go from 100% extended intermediate to 100% prefusion. But with the soluble construct this is not what we see. This could be due to the soluble, monomeric RABV-G being different from the trimeric, membrane bound RABV-G, but in our comparison it appears the membrane stabilizes the prefusion conformation. Furthermore this wide pH range suggests that there is not a single ionizable residue responsible for the conformational change but rather a handful of protonation events must occur for the conformational change to occur. This could be why we did not see a dramatic effect when mutating one or two histidines and instead many more residues must be mutated to prevent the pH dependent conformational change. The lack of a sharp transition could also suggest that the conformational change is not a two state transition. For VSV-G it has been proposed based on SAXS and other biophysical data that there is a collection of expanded states that are not fully extended but are no longer making contacts between the PHD/FD arm and the CD (*17*); however, it is unclear if these proposed intermediate conformations would exchange differently than the extended intermediate or prefusion conformations, especially in the N-terminal peptide and CD peptides.

From the data of the hydrogen exchange in RABV-G with helix breaking mutations, it seems that the protein can access conformations where the central helix does not form but there is separation between the PHD/FD and the CD as we see that the hinge region of the central helix is fully exchanged at all pHs, but the N-terminal reporter peptide and CD reporter peptide still have a pH dependence. This is supported by the observation that there may be some expanded intermediates that are not fully extended. Therefore, a strategy that breaks the central helix as well as removes ionizable residues may be more effective at stabilizing the prefusion conformation. It appears that the conformational change relies both on pH as well as the ability of the central helix to form.

In conclusion, the data collected to this point is encouraging that an HDX-MS method to probe the conformational landscape of RABV-G could be a useful method for vaccine and therapeutic development. Furthermore, the current qualitative method has allowed for the evaluation of a variety of mutations and conditions and helped us better understand RABV-G including that the membrane stabilizes the prefusion conformation and that the central helix's helical propensity is crucial to the conformational change from prefusion to extended intermediate.

4.5 Methods

4.5.1 Soluble RABV-G Bacmid Production

Based on the construct in (*13*) gene encoding truncated RABV-G CVS-11 to not include the transmembrane domain (residues 1-405), with fusion loops (residues 74-79 and 121-125) mutated to GGSGG, a N-terminal gp67 signal sequence and a C-terminal 6x histidine tag was ordered in a pFastBac1 Plasmid (Genscript, Piscataway NJ). This plasmid was transformed into EMBacY cells by mixing 25 uL of RbCl2 cells with 50 ng of plasmid and incubating on ice for 30 minutes followed by a 45 second heatshock at 42 °C and then a 2 minute recovery on ice. The cells were then recovered in 500 uL of Luria Broth (LB) in a 37 °C shaking incubator for 5 hours. Ten and one-hundred fold serial dilutions were made and then 100 uL was plated on LB agar selection plates containing 165 uM IPTG, 200 ug/mL Bluo-Gal (GoldBio), 50 ug/mL kanamycin, 10 ug/mL tetracycline and 7 ug/mL gentamicin. The plates were incubated for 2-3 days and then were checked for white colonies which indicates the gene was successfully transposed into the bacmid. The white colonies were restreaked onto fresh selection plates and incubated for 2 days to verify the white colony phenotype. The transposition was further confirmed by colony PCR with the following primers: pUC/M13 Forward 5' - CCCAGTCACGACGTTGTAAAACG - 3' pUC/M13 Reverse 5' - AGCGGATAACAATTTCACACAGG- 3' and looking or a product that is 2300 basepairs (from the bacmid) plus 1400 basepairs from the RABV-G gene. Bands of 300 basepairs are untransposed bacmid and those colonies should be avoided. A confirmed colony was then used to make a 50 mL overnight culture in LB with 50 ug/mL Kanamycin, 7 ug/mL Gentamicin and 10 ug/mL Tetracycline. The overnight culture was grown at 37 °C and then bacmid was isolated with a PureLink™ HiPure Plasmid Midiprep Kit (Invitrogen, ThermoFisher). Bacmid was stored in the refrigerator until transfection for no longer than 2 days.

4.5.2 Baculovirus production

To produce baculovirus that contains the RABV-G gene Sf9 cells in a 6-well plate (1.5e6 cells/mL, 1 mL of cells) were prepared and given 3 hours to adhere to the plate. Each RABV-G variant only needs 2-3 wells to prepare enough P0 virus. For each well 8 uL cellfectin II was mixed with 100 uL of -/- ESF 921 Insect Cell Culture Medium, Protein

Free (Expression Systems, Advancion) and then vortexed (solution A) and 1400 ng of bacmid was mixed with 100 uL of -/- ESF 921 Insect Cell Culture Medium, Protein Free and gently mixed. Solutions A and B were then mixed gently and allowed to incubate at room temperature for 15-30 minutes. The cells were then washed with 2 mL of -/- ESF 921 Insect Cell Culture Medium, Protein Free media two times and then 800 uL of -/- ESF 921 Insect Cell Culture Medium, Protein Free was added to the cells followed by adding the transfection mixture dropwise to the well while slowly agitating the plate to mix. After all wells had been treated, the plates were covered and parafilmed and left in a 27 °C non-shaking incubator. Starting on day 2, the cells were examined under a fluorescence microscope to look for cell swelling and YFP expression, which indicates the cells have been transfected and are producing baculovirus. The virus was harvested on day 5 to 6 after transfection by collecting the media and spinning it down at 500xg for 10 minutes to remove cell debris. This virus is P0 and is low titer.

To make a higher titer P1, suspension Sf9s (50 mL, 1e6 cells/mL) were made in -/- ESF 921 Insect Cell Culture Medium, Protein Free and allowed to recover overnight. The cells were then counted and if they were close to 2e6 cells/mL 500 uL of P0 was added and if they were closer to 3e6 cells/mL 750 uL of P0 was added. The cells were incubated at 27 °C on a shaking plate. Every few days, cells were examined under a microscope and counted to determine viability. After 3-4 days, cells were typically >95% alive and 50-60% fluorescent and then after 6-7 days the cells were typically ~50% dead and almost all of the alive cells were fluorescent. At this point the culture was harvested by spinning down the cells and harvesting the supernatant. The supernatant was then passed through a 0.2 um syringe filter, this is then P1.

4.5.3 Soluble RABV-G Expression and Purification

One liter of suspension High5 insect cells were made in -/- ESF 921 Insect Cell Culture Medium at 2e6 cells/mL and were infected with 5-15 mL of P1 and allowed to express for 3-5 days at 27 °C on a shaking incubator. The end day was decided by examining cells under a fluorescent microscope and counting them to determine when approximately 50-60% of cells were still alive and most of the cells were fluorescent. The culture was then spun down at 6k RCF for 40 minutes and the supernatant was passed through a 0.2 um bottletop filter. 100 mL of 10x PBS 20 mM Imidazole pH 7.4 (final concentrations) was added to the supernatant before it was then passed over a 5 mL HisTrap Excel at 5 mL/minute with a peristaltic pump. The column was then washed with 50 column volumes (CV) of 20 mM Imidazole 1X PBS pH 7.5 buffer. The protein was then eluted with 15 CV of 250 mM Imidazole 1X PBS pH 7.5 buffer in 5 mL fractions, a final elution of 5 CV of 500 mM Imidazole 1X PBS pH 7.5 buffer was done to wash the column. Elution fractions were run on a gel to determine where the protein eluted. The fractions with protein were then combined and concentrated in a 10 kDa amicon concentrator down to 2 mL. The concentrated protein was then passed over a

S75 SEC column and the fractions that had mAU signal were run on a gel and then the clean RABV-G fractions were pooled and concentrated to 50 uM before flash freezing and storing at -80 °C until use.

4.5.4 RABV-G eVLP Cloning, Expression and Purification

Full length RABV-G PV s (gift from John Pak) was cloned into a p3BNC plasmid containing the ALIX and EABR tags described in (*23*) (gift from Magnus Hoffmann) using gibson assembly. The resulting plasmid was transformed into MachOne E.coli RbCl2 chemically competent cells via heatshock and plated onto ampicillin LB plates. A 100 mL overnight culture was then inoculated with a colony from the selection plate or a stab from a glycerol stock from a previous overnight culture. The culture was then prepped with a Qiagen maxi-prep kit to get plasmid at 500-2000 ng/uL.

Expi 293 Freestyle cells were prepared in various culture sizes (50-150 mL) at 2.5e6 cells/mL in FreeStyle™ 293 Expression Medium (Gibco, ThermoFisher). To transfect cells, 1 ug DNA per milliliter of cell culture was filtered with 300 uL of OptiMEM media. This was then diluted to 25 ug/mL in OptiMEM. In a separate tube 4 ug of PEI Max (Kyfora Bio) was prepared in 0.4 mL of OptiMEM for every 1 mL of cell culture and mixed well. The DNA mixture was then added to the PEI Max mixture and allowed to complex for 15 minutes before adding dropwise to the cell culture while swirling the flask. The cells were allowed to express for 65-70 hours at 37 °C 8% CO2 before harvesting by spinning down the cells at 4000xg for 15 minutes and collecting the supernatant.

To purify eVLPS, the collected supernatant was passed through a 0.2 um filter and then was set up for sucrose gradient centrifugation. Optiseal 29.9 mL ultracentrifuge tubes (Beckman Coulter) were loaded with 25 mL of filtered supernatant and then 4 mL of 20% sucrose PBS was layered at the bottom of the tube. The tubes were balanced, capped and then spun in an MLA50 rotor in a 10 °C Optima MAX-XP for 2 hours at 48,000 rpm (rcf average = 150,700). The tubes were then emptied and the tubes were cut in half at an angle. 250 uL of 1X PBS was added to the pellet and then the cut tube was covered with parafilm. The pellet was then allowed to incubate overnight at 4 °C before pipetting up and down to resuspend. The resuspended pellets of the same construct were combined and incubated at 37 °C for 15 minutes in an eppendorf tube. The tubes were then spun down at 11,000xg in a tabletop centrifuge for 2 minutes and the supernatant was collected. This was repeated 4 times to remove insoluble aggregates. The final supernatant was then flowed over an S200 sizing column to desalt the eVLPS (coming out in the void volume) from soluble protein (coming out later in the column). The void fraction was then pooled and concentrated to 20 uL for every 25 mL of culture. The eVLPs were then either used immediately for experiments or were flash frozen in liquid nitrogen and stored at -80 °C.

4.5.5 Hydrogen Exchange Buffers

To accommodate the large range of pHs the experiments are done over, a universal buffer was created with sodium citrate, sodium phosphate and sodium borate and sodium chloride (20mM Sodium Phosphate (Dibasic), 20 mM Sodium Citrate, 20 mM Sodium Borate + 150 mM NaCl). For each pH, a buffer was made and adjusted to the desired pH with NaOH and HCl. To make D_2O buffer, buffer was lyophilized overnight and resuspended in D_2O (TCI-America Cat No: W0002). As it has been noted that different buffers shift pKa differently in D_2O, it was empirically determined that the following pH adjustments were made to get a D_2O buffer with 0.05 pH units of the desired pH.

Desired D_2O pD_{read}	Adjust pH of buffer for lyophilizing to
4.8	4.5
5.0	4.7
6.0	5.85
7.0	6.85
8.0	7.85
9.0	8.85

4.5.6.Soluble RABV-G HDX at different pHs

For soluble RABV-G that were not compared to HDX of eVLPS, purified soluble RABV-G was diluted to 15 uM and dialyzed into the proper pH H_2O experiment buffer with a Pierce Microdialysis Plate (10K MWCO, 0.1 mL) in 1.2 mL buffer in a 2 mL eppendorf tube overnight at 4 °C. To initiate exchange, protein was diluted 10-fold to 1.5 uM in D_2O experiment buffer equilibrated to 25 °C (see above). At each timepoint, exchange was quenched by mixing 60 uL of exchange reaction with 60 uL of ice-cold 2X quench buffer (3.6M GdnCl 500 mM TCEP 200 mM glycine pH 2.4) and immediately flash freezing. Samples were stored at -80 °C until LC-MS.

4.5.7 eVLP RABV-G HDX at different pHs

Purified eVLPs or 15 uM soluble RABV-G were dialyzed into the proper pH H_2O experiment buffer with a Pierce Microdialysis Plate (10K MWCO, 0.1 mL) in 1.2 mL buffer in a 2 mL eppendorf tube overnight at 4 °C. To initiate exchange, eVLP or soluble RABV-G was diluted 10-fold to 1.5 uM in D_2O experiment buffer equilibrated to 25 °C (see above). At each timepoint, exchange was quenched by mixing 100 uL of exchange reaction with 100 uL of ice-cold 2X offline digestion quench buffer containing zirconium oxide (3M Urea 20 mM TCEP pH 2.4 with 25 mg/ml Zirconium oxide) and adding 2 uL of a mixture of aspergillopepsin (Sigma-Aldrich P2143) and porcine pepsin (Sigma-Aldrich P6887) (3.5 mg/mL aspergillopepsin, 5 mg/mL porcine pepsin). The

mixture was vortexed for 3 seconds before incubating on ice until 1 minute of total quench time. The mixture was then hardspinned (21.1 k rcf) for 10 seconds and the supernatant was removed, put in a clean tube and flash frozen in liquid nitrogen. Samples were stored at -80 °C until LC-MS.

4.5.8 Liquid chromatography - mass spectrometry.

All samples were thawed immediately before injection into a cooled valve system (Trajan LEAP) coupled to a LC (Thermo UltiMate 3000). Sample time points were injected in random order. The temperature of the valve chamber, trap column, and analytical column were maintained at 2 °C. The temperature of the protease column was maintained at 10 °C. For online digestion samples, the quenched sample was subjected to inline digestion by two immobilized acid proteases in order, aspergillopepsin (Sigma-Aldrich P2143) and porcine pepsin (Sigma-Aldrich P6887) at a flow rate of 200 µL/min of buffer A (0.1 % formic acid). Protease columns were prepared in house by coupling protease to beads (Thermo Scientific POROS 20 Al aldehyde activated resin 1602906) and packed by hand into a column (2mm ID x 2 cm, IDEX C-130B). For offline digestion sample, the protease columns were bypassed. Peptides were desalted for 4 minutes on a hand-packed trap column (Thermo Scientific POROS R2 reversed-phase resin 1112906, 1 mm ID x 2 cm, IDEX C-128). Peptides were then separated with a C18 analytical column (ACQUITY UPLC BEH C18 Column, 130Å, 1.7 µm, 1 mm X 50 mm) and a gradient of 5-40% buffer B (100% Acetonitrile, 0.1% Formic Acid) at a flow rate of 40 µL/min over 14 minutes, and then of 40-90% buffer B over 30 seconds. The analytical and trap columns were then subjected to a sawtooth wash and equilibrated at 5% buffer B prior to the next injection. Protease columns were washed with two injections of 100 µL 1.6 M GdmCl, 0.1% formic acid prior to the next injection. Peptides were eluted directly into a Q Exactive Orbitrap Mass Spectrometer operating in positive mode (resolution 70000, AGC target 3e6, maximum IT 50 ms, scan range 300-1500 m/z). For each spike construct, a tandem mass spectrometry experiment was performed (Full MS settings the same as above, dd-MS2 settings as follows: resolution 17500, AGC target 2e5, maximum IT 100 ms, loop count 10, isolation window 2.0 m/z, NCE 28, charge state 1 and ≥7 excluded, dynamic exclusion of 15 seconds) on undeuterated samples.

4.5.9 Peptide identification

Byonic (Protein Metrics) was used to identify unmodified and glycosylated peptides in the tandem mass spectrometry data. The sequence of the expressed construct, including signal sequence and trimerization domain, was used as the search library. Sample digestion parameters were set to non-specific. Precursor mass tolerance and fragment mass tolerance was set to 6 and 10 ppm respectively. Variable N-linked glycosylation was allowed, with a library of insect N-glycans used in the search (for soluble RABV-G) or human N-glycans (for eVLP RABV-G). Peptide lists (sequence,

charge state, and retention time) were exported from Byonic and imported into HDExaminer 3 (Sierra Analytics). When multiple peptide lists were obtained, all were imported and combined in HDExaminer 3.

4.5.10 HDExaminer3 analysis

Peptide isotope distributions at each exchange time point were fit in HDExaminer 3.2. For glycosylated peptides, only the highest confidence modification was included in the mass spectra search and analysis. Deuteration levels were determined by subtracting mass centroids of deuterated peptides from undeuterated peptides.

4.6 References

1. B. M. Davis, G. F. Rall, M. J. Schnell, Everything You Always Wanted to Know About Rabies Virus (But Were Afraid to Ask). *Annu. Rev. Virol.* **2**, 451–471 (2015).
2. E. G. Pieracci, Vital Signs: Trends in Human Rabies Deaths and Exposures — United States, 1938–2018. *MMWR Morb. Mortal. Wkly. Rep.* **68** (2019).
3. CDC, Rabies Post-exposure Prophylaxis, *Rabies* (2024). https://www.cdc.gov/rabies/hcp/prevention-recommendations/post-exposure-prophylaxis.html.
4. K. Natesan, S. Isloor, B. Vinayagamurthy, S. Ramakrishnaiah, R. Doddamane, A. R. Fooks, Developments in Rabies Vaccines: The Path Traversed from Pasteur to the Modern Era of Immunization. *Vaccines* **11**, 756 (2023).
5. CDC, Rabies Pre-exposure Prophylaxis, *Rabies* (2024). https://www.cdc.gov/rabies/hcp/prevention-recommendations/pre-exposure-prophylaxis.html.
6. PEP recommendations. https://www.who.int/teams/control-of-neglected-tropical-diseases/rabies/pep-recommendations.
7. R. Gharpure, A. O. Akumu, J. Dawa, S. Gobin, B. B. Adhikari, K. E. Lafond, L. S. Fischer, H. Mirieri, H. Mwazighe, C. Tabu, R. Jalang'o, P. Kamau, C. Silali, R. Kalani, P. Oginga, I. Jewa, V. Njenga, M. S. Ebama, J. S. Bresee, M. K. Njenga, E. Osoro, M. I. Meltzer, G. O. Emukule, Costs of seasonal influenza vaccine delivery in a pediatric demonstration project for children aged 6–23 months — Nakuru and Mombasa Counties, Kenya, 2019–2021. *Vaccine* **42**, 125519 (2024).
8. A. E. Jean Baptiste, J. Van der Schans, S. Bawa, B. Masresha, J. Wagai, J. Oteri, B. Dieng, M. Soyemi, R. Eshuchi, Y. G. Yehualashet, O. Afolabi, F. Braka, A. Bita, E. Hak, The cost of implementing measles campaign in Nigeria: comparing the stand-alone and the integrated strategy. *Health Econ. Rev.* **13**, 36 (2023).
9. W. Davis, The Capitol fox fascinated folks. But no one mentioned the cost of rabies treatment, *NPR* (2022). https://www.npr.org/2022/04/09/1091797594/the-capitol-fox-fascinated-folks-but-no-one-mentioned-the-cost-of-rabies-treatme.
10. G. D. de Melo, F. Sonthonnax, G. Lepousez, G. Jouvion, A. Minola, F. Zatta, F. Larrous, L. Kergoat, C. Mazo, C. Moigneu, R. Aiello, A. Salomoni, E. Brisebard, P. De Benedictis, D. Corti, H. Bourhy, A combination of two human monoclonal antibodies cures symptomatic rabies. *EMBO Mol. Med.* **12**, e12628 (2020).
11. S. Roche, F. A. Rey, Y. Gaudin, S. Bressanelli, Structure of the Prefusion Form of the Vesicular Stomatitis Virus Glycoprotein G. *Science* **315**, 843–848 (2007).
12. S. Roche, S. Bressanelli, F. A. Rey, Y. Gaudin, Crystal structure of the low-pH form of the vesicular stomatitis virus glycoprotein G. *Science* **313**, 187–191 (2006).
13. F. Yang, S. Lin, F. Ye, J. Yang, J. Qi, Z. Chen, X. Lin, J. Wang, D. Yue, Y. Cheng, Z. Chen, H. Chen, Y. You, Z. Zhang, Y. Yang, M. Yang, H. Sun, Y. Li, Y. Cao, S. Yang, Y. Wei, G. F. Gao, G. Lu, Structural Analysis of Rabies Virus Glycoprotein Reveals pH-Dependent Conformational Changes and Interactions with a Neutralizing Antibody. *Cell Host Microbe* **27**, 441-453.e7 (2020).
14. H. M. Callaway, D. Zyla, F. Larrous, G. D. de Melo, K. M. Hastie, R. D. Avalos, A. Agarwal, D. Corti, H. Bourhy, E. O. Saphire, Structure of the rabies virus

glycoprotein trimer bound to a prefusion-specific neutralizing antibody. *Sci. Adv.* **8**, eabp9151 (2022).
15. W. M. Ng, S. Fedosyuk, S. English, G. Augusto, A. Berg, L. Thorley, R. R. Segireddy, T. A. Bowden, A. D. Douglas, “Structure of trimeric pre-fusion rabies virus glycoprotein in complex with two protective antibodies” (preprint, Microbiology, 2022); https://doi.org/10.1101/2022.02.28.482293.
16. A. Abou-Hamdan, L. Belot, A. Albertini, Y. Gaudin, Monomeric Intermediates Formed by Vesiculovirus Glycoprotein during Its Low-pH-induced Structural Transition. *J. Mol. Biol.* **430**, 1685–1695 (2018).
17. A. A. Albertini, C. Mérigoux, S. Libersou, K. Madiona, S. Bressanelli, S. Roche, J. Lepault, R. Melki, P. Vachette, Y. Gaudin, Characterization of Monomeric Intermediates during VSV Glycoprotein Structural Transition. *PLOS Pathog.* **8**, e1002556 (2012).
18. E. Baquero, A. A. Albertini, H. Raux, A. Abou-Hamdan, E. Boeri-Erba, M. Ouldali, L. Buonocore, J. K. Rose, J. Lepault, S. Bressanelli, Y. Gaudin, Structural intermediates in the fusion-associated transition of vesiculovirus glycoprotein. *EMBO J.* **36**, 679–692 (2017).
19. Y. Gaudin, R. W. Ruigrok, M. Knossow, A. Flamand, Low-pH conformational changes of rabies virus glycoprotein and their role in membrane fusion. *J. Virol.* **67**, 1365–1372 (1993).
20. Y. Gaudin, H. Raux, A. Flamand, R. W. Ruigrok, Identification of amino acids controlling the low-pH-induced conformational change of rabies virus glycoprotein. *J. Virol.* **70**, 7371–7378 (1996).
21. I. S. Kim, S. Jenni, M. L. Stanifer, E. Roth, S. P. J. Whelan, A. M. van Oijen, S. C. Harrison, Mechanism of membrane fusion induced by vesicular stomatitis virus G protein. *Proc. Natl. Acad. Sci.* **114**, E28–E36 (2017).
22. J. Hellert, J. Buchrieser, F. Larrous, A. Minola, G. D. de Melo, L. Soriaga, P. England, A. Haouz, A. Telenti, O. Schwartz, D. Corti, H. Bourhy, F. A. Rey, Structure of the prefusion-locking broadly neutralizing antibody RVC20 bound to the rabies virus glycoprotein. *Nat. Commun.* **11**, 596 (2020).
23. M. A. G. Hoffmann, Z. Yang, K. E. Huey-Tubman, A. A. Cohen, P. N. P. Gnanapragasam, L. M. Nakatomi, K. N. Storm, W. J. Moon, P. J. C. Lin, P. J. Bjorkman, ESCRT recruitment to mRNA-encoded SARS-CoV-2 spike induces virus-like particles and enhanced antibody responses. bioRxiv [Preprint] (2022). https://doi.org/10.1101/2022.12.26.521940.